Search for New Physics Using Events with Two Photons and Large Missing Transverse Energy in pp Collisions at $\sqrt{s} = 7$ TeV

by

Yueh-Feng Liu

Submitted in partial fulfillment of the
requirements for the degree of
Doctor of Philosophy
at

Carnegie Mellon University
Department of Physics
Pittsburgh, Pennsylvania

Advised by Professor Manfred Paulini

January 25, 2013

Abstract

A search for new physics in events with two photons and missing transverse energy is performed. Data corresponding to an integrated luminosity of 4.93 fb^{-1} in proton-proton collisions at $\sqrt{s} = 7$ TeV collected by the CMS detector at the Large Hadron Collider are analyzed. No excess of events with large missing transverse energy is observed by comparing the data to the expected standard model processes. The results are interpreted within the general gauge-mediated supersymmetry model and through simplified model spectra. Upper limits on the signal production cross sections and exclusion regions at the 95% confidence level are set in the parameter space of the respective models.

Acknowledgments

I would like to express my deep gratitude to my advisor Prof. Manfred Paulini who provides me all possible research resources, gives me freedom when I explore physics and guides me when I need advices. Without his help, I cannot complete my Ph.D. degree.

I thank other members of my thesis committee: Prof. Thomas A. Ferguson, Prof. Tao Han and Prof. James S. Russ for their comments and advices on my thesis, especially for Prof. Thomas A. Ferguson's detailed comments.

I thank CMS SUSY photon group, especially Dr. Dongwook Jang and Dr. David A. Mason for your useful suggestions and discussions.

To my family, your support is the energy keeps me moving forward. Thanks you!!!

Contents

List of Figures

List of Tables

Chapter 1

Introduction

The standard model (SM) of particle physics is a fundamental and well-tested physics theory. Although high-precision experiments have repeatedly verified subtle effects predicted by the SM, many fundamental questions of physics, such as the origin of mass and the properties of the dark matter and dark energy composing 95% of the universe, need to be answered. It is believed that new physics beyond the SM (BSM) is required to explain the nature of our world.

Supersymmetry is one of the popular theories that provides solutions to explain the physics BSM. However, there are many versions of supersymmetry owing to our limited knowledge about the new physics. Different models result in different physical final states.

In this thesis, a search for new physics in *pp* collisions at a center-of-mass energy of 7 TeV is performed, using events with two photons and missing transverse energy in the final state. The data were collected by the Compact Muon Solenoid (CMS) detector at the Large Hadron Collider (LHC) during

2011. Previous searches for supersymmetry based on two photons in the final state have been performed by the ATLAS [1], CMS [2], CDF [3], and D0 [4] experiments.

This thesis is organized in the following way. An introduction of the standard model and a description of the new physics model that we are looking for are given in Chapter 1. The properties of the experimental apparatus are described in Chapter 2, and the methods for reconstructing physical objects are discussed in Chapter 3. Chapter 4 covers the event selections of the analysis, while Chapter 5 describes the procedure for estimating the background. The results are given in Chapter 6. Finally, Chapter 7 summarizes the conclusions from the results.

1.1 Standard Model

The SM of particle physics is a quantum field theory that describes the known elementary particles and their interactions [5, 6]. One of the principles of the SM is that the Lagrangian, which represents the dynamics of the quantum system, is invariant under local gauge transformations. The associated gauge bosons with integer spin are the force carriers that mediate the electromagnetic, weak and strong interactions in the SM. The elementary particles included in the SM having spin 1/2 are called fermions. All matter is made out of fermions and bosons.

Fermions are further classified as either leptons or quarks according to the different interactions in which they participate. Leptons are grouped into three generations. The first lepton generation consists of the electron and a corresponding electron neutrino. The muon and muon neutrino form the

Table 1.1: Elementary fermions of the SM.

	1^{st} generation	2^{nd} generation	3^{rd} generation	charge
Leptons	e	μ	τ	-1
	ν_e	ν_μ	ν_τ	0
Quarks	u	c	t	2/3
	d	s	b	-1/3

second lepton generation, while the tau and tau neutrino belong to the third lepton generation. Each generation has a similar physical behavior. The main differences between the three generations are the masses and lifetimes of the charged leptons. For example, tau particles can decay into muons or electrons, and muons can decay into electrons, while electrons are stable particles.

There are six flavors of quarks known as up, down, charm, strange, top and bottom. Quarks can also be divided into three generations. Each generation consists of one quark with electric charge +2/3 and one quark with electric charge -1/3. Table 1.1 summarizes the fermions of the SM.

Gauge bosons play the role of the force mediators between the elementary particles. The gauge group of the SM can be described as

$$SU(3)_C \times SU(2)_L \times U(1)_Y. \tag{1.1}$$

$SU(3)_C$ is the gauge group of the strong interaction, which is one of four fundamental interactions of nature [7]. There exist 8 massless gauge bosons of the strong interaction, called gluons. Both gluons and quarks carry a color charge, which means that gluons can interact not only with quarks but also with other gluons. Particles with color charge cannot be observed individually because of "color confinement", which requires particles with color such as quarks and gluons to be confined and to form color-neutral states (hadrons). Hadrons are categorized into two families: baryons, which are made up of three quarks with different color charges, and mesons, which are made up of one quark and one anti-quark. Another property of the strong interaction is "asymptotic freedom", which states that the interactions between quarks and gluons become weaker as the distance between them decreases and the energy of the interaction increases.

$SU(2)_L \times U(1)_Y$ is the unification of the weak and electromagnetic interactions [8, 9, 10]. A weak-isospin current couples to a weak-isotriplet vector boson W originating from SU(2) (W^1, W^2, W^3), and the weak-hypercharge current couples to an isosinglet vector boson B originating from U(1). Combinations of the W^1 and W^2 components form the charged $W^{\pm}$ bosons that couple only to the left-handed helicity states of quarks and leptons. On the other hand, the linear combinations of W^3 and B form the Z^0 boson and the photon γ:

$$\begin{pmatrix} \gamma \\ Z^0 \end{pmatrix} = \begin{pmatrix} \cos\theta_W & \sin\theta_W \\ -\sin\theta_W & \cos\theta_W \end{pmatrix} \begin{pmatrix} B \\ W^3 \end{pmatrix} \tag{1.2}$$

where θ_W is the weak mixing angle.

By introducing a scaler field and requiring it to have a non-zero vacuum expectation value, $SU(2)_L \times U(1)_Y$ is spontaneously broken [11]. Spontaneous symmetry breaking provides a mechanism to generate the mass of the gauge bosons, but also introduces an additional scaler particle, the Higgs boson. Elementary particles gain mass by interacting with the Higgs boson, which is known as the Higgs mechanism. The ATLAS and CMS experiments at the LHC announced the discovery of a Higgs-like boson with a mass between

Table 1.2: The gauge group, charge and spin of the fundamental bosons of the SM.

	Gauge Group	Charge	Spin
g	$SU(3)_C$	0	1
$W^{\pm}$	$SU(2)_L \times U(1)_Y$	±1	1
γ	$SU(2)_L \times U(1)_Y$	0	1
Z	$SU(2)_L \times U(1)_Y$	0	1
H		0	0

125-127 GeV in July 2012 [12, 13]. Table 1.2 summarizes the properties of the bosons of the SM.

1.2 New Physics

Although the SM has passed stringent quantitative experimental tests, we have plenty of motivations to explore particle physics beyond the SM.

1.2.1 Motivations for New Physics

First, if the newly discovered boson is the expected SM Higgs boson, it will couple to fermions via the Yukawa interaction $\mathcal{L}_{Yukawa} = -\lambda_f \bar{f} H f$, where λ_f is the Yukawa coupling and f is the fermion field. The one-loop correction to the Higgs mass due to fermions, as shown on the left of Figure 1.1, can be written as

$$\Delta m_H^2 = -\frac{|\lambda_f|^2}{8\pi^2}\Lambda^2 + \mathcal{O}(\ln \Lambda), \tag{1.3}$$

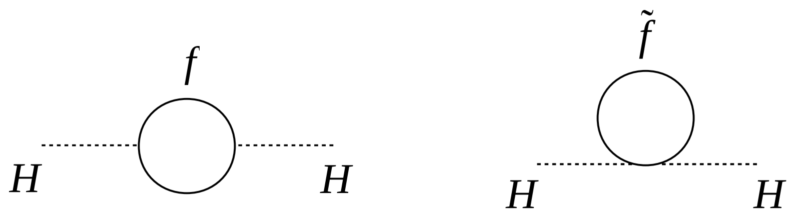

Figure 1.1: Feynman diagrams for the one-loop correction to the Higgs mass with a fermion on the left and supersymmetric scalar on the right.

where Λ is the "ultraviolet cutoff", or the mass scale, up to which the SM is valid. If Λ is on the order of the Plank scale, $M_p \sim 10^{19}$ GeV, fine-tuning is needed to have $m_H^2 \sim (125 \text{ GeV})^2$, which is an unnatural physics situation. However, suppose a scalar superpartner $\bar{f}$ for each corresponding fermion also contributes to the one-loop correction of the Higgs mass, as shown on the right of Figure 1.1,

$$\Delta m_H^2 = \frac{\lambda_{\tilde{f}}}{8\pi^2}\Lambda^2 + \mathcal{O}(\ln \Lambda). \tag{1.4}$$

The quadratic Λ term can be canceled if $|\lambda_f|^2 = \lambda_{\tilde{f}}$. Therefore, the extension of the SM provides a way to avoid the hierarchy problem of the Higgs mass [14].

Furthermore, in astrophysics and cosmology, several observations have shown evidence for the presence of dark matter. For example, gravitational lensing studies of the Bullet Cluster, which is a system of two galaxy clusters in collision, shows that much of the mass of the Bullet Cluster resides outside the central region of the baryonic mass (visible matter) [15]. In addition, the discrepancy between the expected and observed galaxy rotation curves, as shown in Figure 1.2, suggests the existence of dark matter [16,17]. By measuring the cosmic microwave background anisotropies, the Wilkinson Microwave Anisotropy Probe (WMAP) estimates that our university is made up of 73% dark energy, 23% dark matter, and only 4% baryonic matter [18]. The SM cannot account for dark matter, but supersymmetry (see Sec. 1.2.2) can provide a possible dark matter candidate.

Finally, the $SU(3)_C \times SU(2)_L \times U(1)_Y$ gauge theory has three independent gauge coupling constants and describes well elementary particles at energies presently probed by experiments. The question is whether this theory will be valid at higher energies. Theoretically, it is believed that the $SU(3)_C \times SU(2)_L \times U(1)_Y$ gauge group is embedded in a larger group known as grand unification theory [19, 20]. In this theory, the three different coupling constants are unified at some high-energy scale. This goal cannot be achieved under the framework of the SM, as shown in Figure 1.3. However, the assumption of supersymmetry predicts a gauge-coupling unification at a high-energy scale, as displayed in Figure 1.3 [14].

1.2.2 Supersymmetry

Supersymmetry (SUSY) [14, 21, 22] is a symmetry relating fermions and bosons. A SUSY generator $\mathcal{Q}$ transforms a fermion state into a boson state, and vise versa

$$\mathcal{Q}|Fermion\rangle = |Boson\rangle, \qquad \mathcal{Q}|Boson\rangle = |Fermion\rangle. \tag{1.5}$$

A supermultiplet containing both fermion and boson states is an irreducible representation of single-particle states in a supersymmetric theory. Each supermultiplet has an equal number of fermionic and bosonic degrees of free-

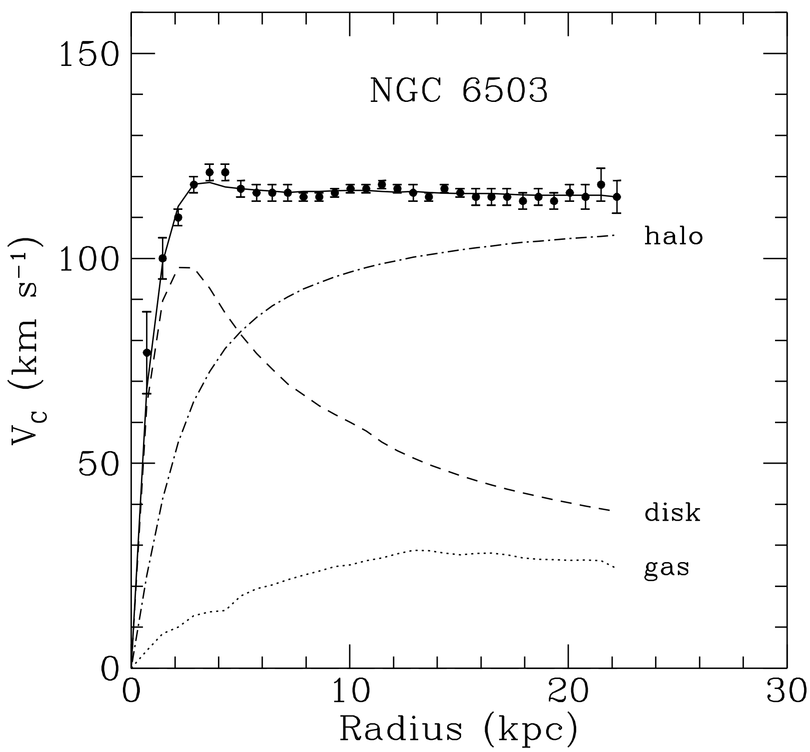

Figure 1.2: Rotation curve for the spiral galaxy NGC6503. The points are the measured circular rotation velocities as a function of distance from the center of the galaxy. Contributions to the rotational velocity due to matter in the observed disk (dashed curve) and gas (dotted curve) are shown. The dot-dash curve is the contribution from the dark matter halo.

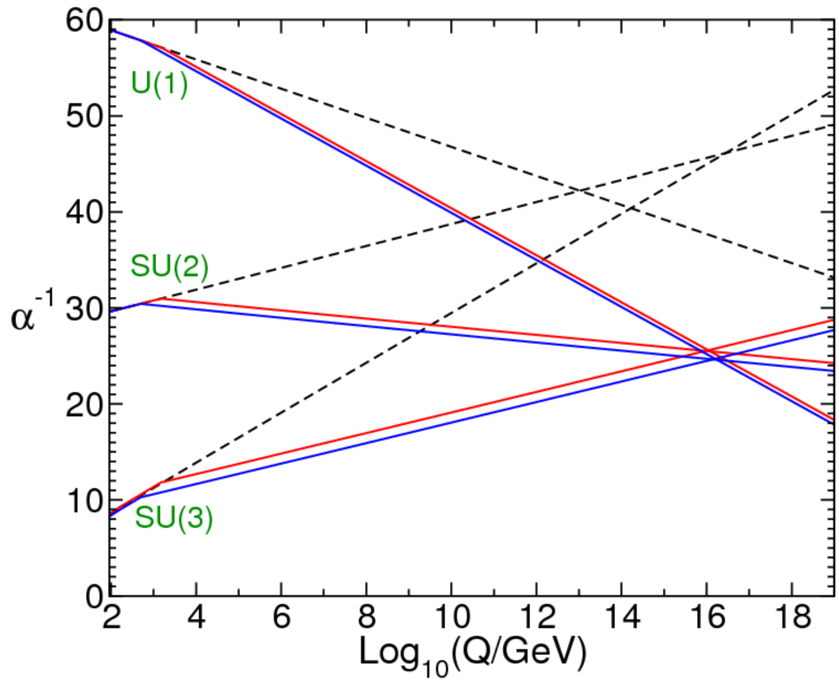

Figure 1.3: Evolution of the inverse gauge couplings $\alpha_a^{-1}(Q)$ in the SM (dashed lines) and the Minimal Supersymmetric Standard Model (MSSM) (solid lines) as a function of energy Q. The bands are found by varying sparticle masses between 500 and 1500 GeV and α_3 between 0.117 and 0.121 for the MSSM case.

Table 1.3: SM particles and their superpartners in the MSSM.

SM particles		Spin	MSSM particles		spin
Lepton	l	1/2	Slepton	$\tilde{l}$	0
Quark	q	1/2	Squark	$\tilde{q}$	0
Gluon	g	1	Gluino	$\tilde{g}$	1/2
B Boson	B	1	Bino	$\tilde{B}$	1/2
W Boson	$W^{\pm}, W^0$	1	Wino	$\tilde{W}^{\pm}, \tilde{W}^0$	1/2
Higgs Boson	H	0	Higgsino	$\tilde{H}$	1/2
Graviton	G	2	Gravitino	$\tilde{G}$	3/2

dom. The minimal supersymmetric standard model (MSSM) is the minimal extension to the SM based on this concept. In the MSSM, each fundamental SM particle is in either a gauge or chiral supermultiplet, and there must be a superpartner with spin differing by 1/2 unit to satisfy the requirement of equal fermionic and bosonic degrees of freedom. Table 1.3 shows the SM particles and their partners in the MSSM. Table 1.4 gives the relations between the gauge and mass eigenstates of sparticles in the MSSM.

The four-momentum operator or the generator of translation $\mathcal{P}$ commutes with the SUSY operators $\mathcal{Q}$, $\mathcal{Q}^{\dagger}$:

$$[\mathcal{Q},\ \mathcal{P}] = [\mathcal{Q}^{\dagger},\ \mathcal{P}] = 0, \tag{1.6}$$

which implies that the particles in the same irreducible supermultiplet must have equal masses. However, no supersymmetric particle with the same mass as its SM partner has been discovered. If SUSY exists, it must be a spontaneously broken symmetry. The MSSM must be extended to include a sepa-

Table 1.4: Relations between the gauge and mass eigenstates of sparticles in the MSSM.

	Gauge Eigenstates	Mass Eigenstates
Sleptons	$\tilde{e}_L\ \tilde{e}_R\ \tilde{\nu}_e$	$\tilde{e}_L\ \tilde{e}_R\ \tilde{\nu}_e$
	$\tilde{\mu}_L\ \tilde{\mu}_R\ \tilde{\nu}_\mu$	$\tilde{\mu}_L\ \tilde{\mu}_R\ \tilde{\nu}_\mu$
	$\tilde{\tau}_L\ \tilde{\tau}_R\ \tilde{\nu}_\tau$	$\tilde{\tau}_1\ \tilde{\tau}_2\ \tilde{\nu}_\tau$
Squarks	$\tilde{u}_L\ \tilde{u}_R\ \tilde{d}_L\ \tilde{d}_R$	$\tilde{u}_L\ \tilde{u}_R\ \tilde{d}_L\ \tilde{d}_R$
	$\tilde{c}_L\ \tilde{c}_R\ \tilde{s}_L\ \tilde{s}_R$	$\tilde{c}_L\ \tilde{c}_R\ \tilde{s}_L\ \tilde{s}_R$
	$\tilde{t}_L\ \tilde{t}_R\ \tilde{b}_L\ \tilde{b}_R$	$\tilde{t}_1\ \tilde{t}_2\ \tilde{b}_1\ \tilde{b}_2$
Gluinos	$\tilde{g}$	$\tilde{g}$
Neutralinos	$\tilde{B}^0\ \tilde{W}^0\ \tilde{H}_u^0\ \tilde{H}_d^0$	$\tilde{\chi}_1^0\ \tilde{\chi}_2^0\ \tilde{\chi}_3^0\ \tilde{\chi}_4^0$
Charginos	$\tilde{W}^\pm\ \tilde{H}_u^+\ \tilde{H}_d^-$	$\tilde{\chi}_1^\pm\ \tilde{\chi}_2^\pm$
Higgs bosons	$H_u^0\ H_d^0\ H_u^+\ H_d^-$	$h^0\ H^0\ A^0\ H^\pm$

rate SUSY-breaking sector, and only "soft" supersymmetry-breaking terms are allowed to avoid re-introducing the hierarchy problem of the Higgs mass.

The general idea of SUSY breaking is that there is a hidden sector in which SUSY is broken at some high-energy scale [14]. The breaking is mediated to a visible sector, which contains the MSSM via "messengers". There are several SUSY-breaking models depending on the type of mediation, the scale of the messenger M and the SUSY breaking scale $\sqrt{F}$. Table 1.5 summarizes the main scenarios of SUSY breaking.

The MSSM introduces a new quantum number known as R-parity that is defined as

$$R = (-1)^{3B+L+2s}, \tag{1.7}$$

Table 1.5: Different types of SUSY breaking models.

Type	$\sqrt{F}$	M	Gravitino $m_{3/2}$
Gauge Mediation	$\ll 10^{10}$ GeV	$\ll M_{pl}$	$\ll 100$ GeV
Gravity Mediation	$\sim 10^{10}$ GeV	$\sim M_{pl}$	~ 100 GeV
Anomaly Mediation	$\sim 10^{12}$ GeV	$\sim M_{pl}$	$\sim 10^{6}$ GeV

where B is the baryon number, L is the lepton number and s is the spin of the particle. All SM particles have R-parity of 1, while supersymmetric particles have R-parity of -1. If R-parity is conserved, SUSY particles must be produced in pairs because the R-parity of the initial state is 1. Conservation of R-parity also implies that the lightest supersymmetric particle (LSP) cannot decay into SM particles and thus is stable. Therefore, the LSP can serve as dark matter candidate.

1.2.3 General Gauge-Mediated Supersymmetry Breaking

In this analysis, we focus on a scenario known as general gauge-mediated (GGM) supersymmetry breaking [23, 24, 25]. GGM communicates SUSY breaking to the MSSM via the SM gauge interactions and decouples into separate visible and hidden sectors when the MSSM gauge couplings approach zero. The SUSY flavor problem of some SUSY-breaking models, for example, in the lepton-number violating decay $\mu \to e\gamma$, is solved in this gauge mediation framework since SUSY-breaking soft terms are generated by flavor-blind SM gauge interactions.

The general phenomenology of GGM with R-parity conservation includes the following features [26, 27, 28]:

- The gravitino $\tilde{G}$ is always the LSP.

- The next-to-lightest-supersymmetric particle (NLSP) could be one of many SUSY particles, for example, the neutralino, chargino, sneutrino, gluino, squark, or the right-handed slepton.

- The neutralinos are mixtures of the bino, the neutral wino and the neutral higgsinos, while charginos are mixtures of the charged winos and higgsinos, as shown in Table 1.4.

- The bino-like NLSP decay is dominated by the $\tilde{\chi}_1^0 \to \gamma + \tilde{G}$ channel with a branching fraction of $\sim 80\%$ for most of the bino-like NLSP masses. The $\tilde{\chi}_1^0 \to Z + \tilde{G}$ channel accounts for the rest of the branching fraction $\sim 20\%$ for most of the bino-like NLSP masses, as plotted in Figure (left) 1.4 [27].

- Wino-like neutralinos and charginos are nearly degenerate in mass. In this case, they are wino co-NLSPs. The wino-like neutralino decays into $Z + \tilde{G}$ or $\gamma + \tilde{G}$. The branching fraction of the $\gamma + \tilde{G}$ channel is high for the low mass ($\sim$ 100 GeV) wino-like neutralinos and descends to $\sim 20\%$, as displayed in Figure 1.4 (right) [27]. The wino-like chargino can also decay to the gravitino via $\tilde{\chi}_1^\pm \to W^\pm + \tilde{G}$.

In this analysis, only bino-like and wino-like NLSPs are considered since they produce photons in the final states. Figure 1.5 illustrates some Feynman diagrams of bino-like neutralino processes that produce two photons in the final state.

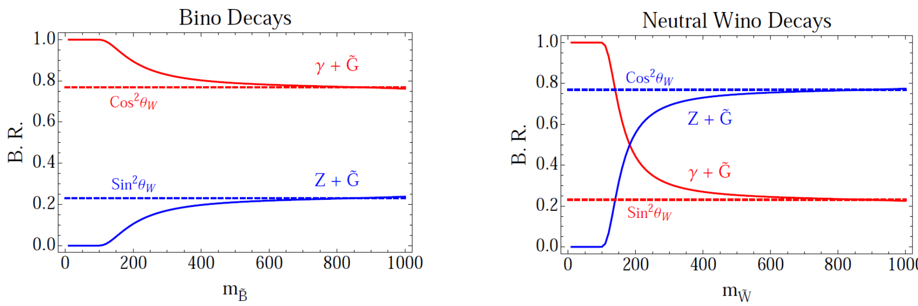

Figure 1.4: Branching fraction of bino-like neutralino decays (left) and wino-like neutralino decays (right), as a function of their masses. Bino-like and wino-like neutralinos decay to a photon and gravitino (red curves) or a Z boson and gravitino (blue curves).

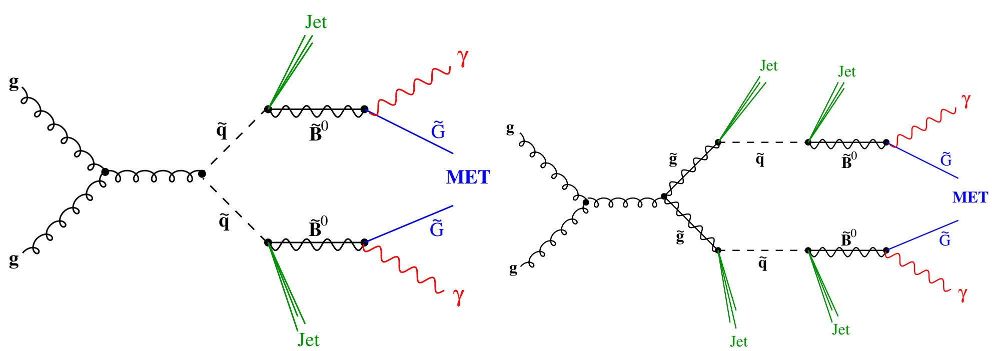

Figure 1.5: Feynman diagrams of GGM SUSY bino-like neutralino processes.

1.2.4 Simplified Supersymmetry Model Spectra

In addition to the GGM scenario, we also consider the simplified supersymmetry model spectra (SMS) [29, 30, 31] in this analysis. The simplified model is defined by an effective Lagrangian describing the interactions using a small number of new-physics particles. The SMS has the simplest particle spectra, characterized only by particle masses, production cross sections, and branching fractions. In order to produce a SUSY-like diphoton signature in this model, pairs of gluinos are initially produced and decay to jets and two neutralinos. Each neutralino then decays with 100% branching fraction into a photon and a gravitino, as shown in Figure 1.6. SMS illustrate clear boundaries of search sensitivity because of the dependence of the reconstruction and selection efficiencies on the mass differences between parent and daughter particles. In addition, SMS provide a natural starting point to quantify the consistency of new-physics signals with different kinds of physics reaction. Finally, limits on simplified models can be used to deduce constraints on a wide variety of models giving rise to the same topologies.

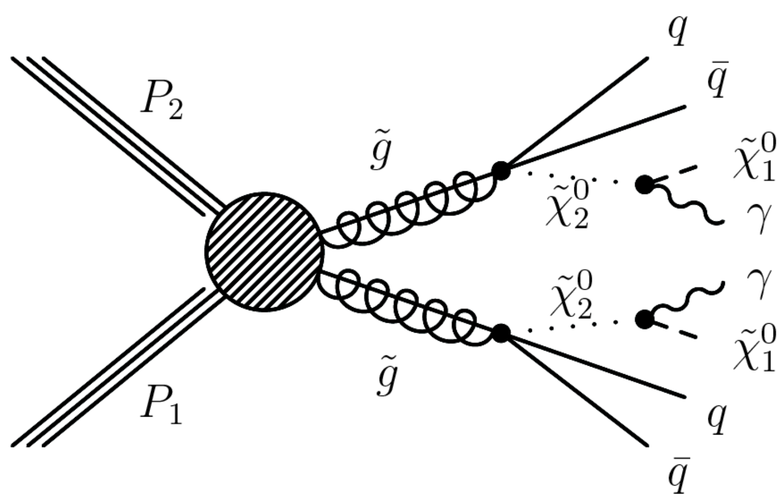

Figure 1.6: Feynman diagram in the SMS model for the production and decay of two gluinos.

Chapter 2

Large Hadron Collider and the Compact Muon Solenoid Detector

2.1 LHC

The Large Hadron Collider (LHC) is a proton-proton particle accelerator at the European Organization for Nuclear Research (CERN) [32]. The goals of the LHC are to understand the nature of particle physics and explore new physics beyond the SM. Several accelerating structures used to boost the proton beams are installed in a tunnel 27 kilometers in circumference, located between 45 and 170 meters below the surface.

Inside the accelerator, two proton beams travel in opposite directions in separate beam pipes. The beam tubes are kept at ultrahigh vacuum to minimize

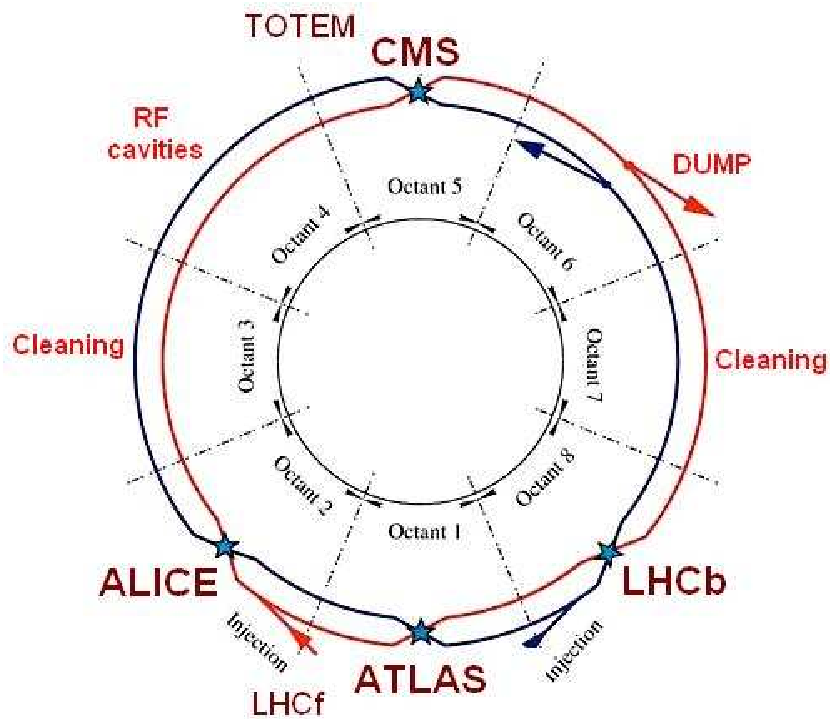

Figure 2.1: Schematic layout of the LHC.

the interactions between protons and gas molecules. The proton beams obtain energy from radio-frequency (RF) cavities located at certain points around the ring. When a proton bunch passes through the electric field in a RF cavity, energy is transfered to the protons. In the end, the proton beams obtain their full energy before colliding with one another. Thousands of superconducting magnets are the main components of the LHC. The refrigeration system cools the magnets to a temperature below 2 K and an electric current over 8000 A then provides a magnetic field above 8 T. Dipole magnets are used to bend the path of the proton beams, while quadrupole magnets focus the particles of beams. Figure 2.1 shows the schematic layout of the LHC.

The design center-of-mass energy of the LHC is 14 TeV. However, the LHC operated at a reduced center-of-mass energy of 7 TeV starting in 2010, and continued 7 TeV running during 2011. The design luminosity of the LHC is $L = 10^{34}\ cm^{-2}s^{-1}$, which corresponds to about 1 billion proton-proton interactions per second. At the end of 2011, the machine reached a peak luminosity around $L = 5 \times 10^{33}\ cm^{-2}s^{-1}$. The luminosity can be described as [32]:

$$L = \frac{f_{rev} N_b^2 n_b \gamma_\gamma}{4\pi\varepsilon_n\beta} F, \tag{2.1}$$

where f_{rev} is the revolution frequency of a signal beam, N_b is the number of particles per bunch, n_b is the number of bunches per beam, γ_γ is the Lorentz factor, ε_n is the normalized transverse beam emittance, β is beta function at the interaction point, and F is the geometric luminosity reduction factor due to the crossing angle of the beams.

2.2 CMS Detector

The Compact Muon Solenoid (CMS) detector [32, 33] is one of two general-purpose experiments at the LHC. The dimensions of the CMS detector are 21.6 meters in length, 14.6 meters in diameter and a total weight of 12500 tons. The detector consists of layers of different subdetectors designed to measure properties of particles emerging from the collisions. The main components are the inner tracking system, the electromagnetic calorimeter (ECAL), the hadron calorimeter (HCAL), the superconducting magnet, the muon system, and the forward detectors. In order to meet the physics requirements and handle the high luminosity delivered by the LHC, the CMS detector has several features. First, a high quality tracking system that is able to

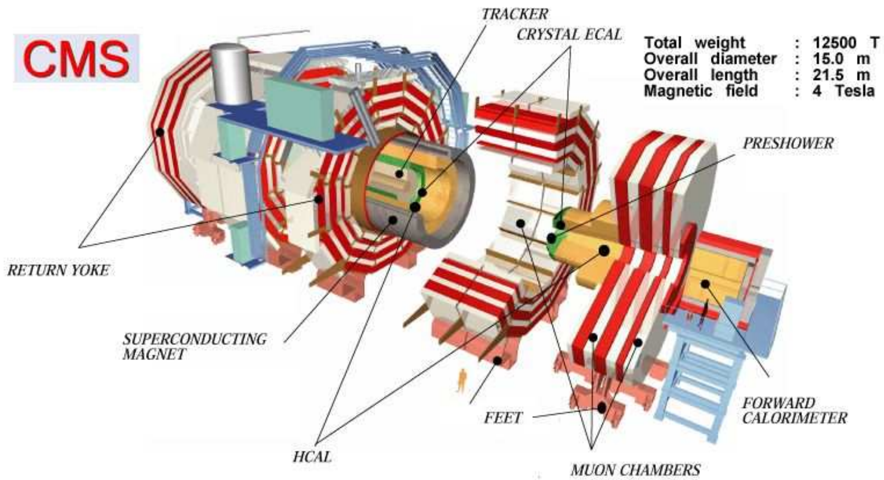

Figure 2.2: A perspective view of the CMS detector.

measure charged-particle momentum with good resolution and reconstruction efficiency. Second, good electromagnetic energy resolution, resulting in a good mass resolution for diphoton states over a wide geometric coverage. Third, hadron calorimeters with a large geometric coverage and fine lateral segmentation providing good missing-transverse-energy and dijet-mass resolution. Fourth, a high performance system to detect and measure muons over a wide range of momenta and solid angle. Figure 2.2 shows a perspective view of the CMS detector.

The origin of the coordinate system used by CMS is the center of the collision point inside the detector. The x axis points radially inward toward the center of the LHC, the y axis points vertically upward, and the direction of the z axis is determined by the right-hand rule. The polar angle θ is measured from the z axis and the azimuthal angle ϕ is measured from the x axis in the x-y plane. The pseudorapidity is defined as $\eta = -\ln\tan(\theta/2)$. Important physical quantities such as the transverse momentum p_T, the transverse energy E_T

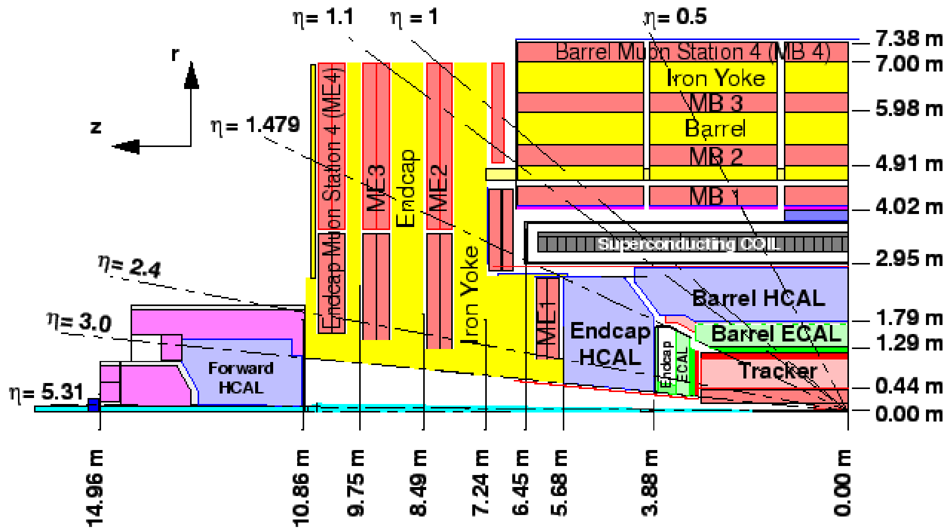

Figure 2.3: A schematic layout showing one segment of the CMS detector.

and the imbalance of transverse energy E_T^{miss} are measured in the x-y plane, which is transverse to the beam direction. Figure 2.3 illustrates a schematic layout of the CMS detector.

2.2.1 Inner Tracking System

The purpose of the inner tracking system is to measure the trajectories of charged particles precisely and efficiently. In order to identify the particle trajectories in situations with a high rate of inelastic collisions superimposed on the pp hard collision of interest, a high granularity detector is required. On the other hand, it is important to use a minimum amount of material in the inner detector to limit nuclear interactions, multiple scattering, bremsstrahlung, and photon conversion. A compromise is achieved in the design of the CMS tracking system.

The CMS tracker is composed of a pixel detector and a silicon strip tracker covering an acceptance range up to $|\eta| < 2.5$. The pixel detector, which is the closest to the interaction region, has three barrel layers at radii of 4.4, 7.3 and 10.2 cm from the beamline, and each layer is 53 cm in length. There are two endcap disks with radius 6 to 15 cm placed at $z = \pm 34.5$ cm and $z = \pm 46.5$ cm. A pixel cell provides similar track resolution in both the r-ϕ and z directions. This results in the pixel detector providing a small impact parameter resolution and good secondary-vertex reconstruction. A charge interpolation technique achieves a spatial-hit resolution in the range of 15 to 20 μm.

The silicon strip tracker consisting of three subsystems occupies the radial region between 20 and 116 cm. The tracker inner barrel and disks (TIB/TID) are made of 4 barrel layers and 3 disks at each end. TIB/TID cover up to 55 cm in radius and provide 4 r-ϕ measurements on a charged-track trajectory. The tracker outer barrel (TOB) surrounds the TIB/TID and extends the tracking radius to 116 cm. TOB has 6 layers of micro-strip sensors and delivers another 6 r-ϕ measurements on a charged-track trajectory. The tracker endcaps (TEC) occupy the region 124 cm $< |z| <$ 282 cm and 22.5 cm $< r <$ 113.5 cm. Each TEC has 9 disks and can provide up to 9 ϕ-measurement per trajectory. Figure 2.4 shows a schematic view of the CMS tracker region.

The radiation lengths of the CMS tracker starts from 0.4 X_0 around $|\eta| \approx 0$, increases to 1.8 X_0 around $|\eta| \approx 1.4$, and then decreases to 1.0 X_0 at $|\eta| \approx 2.5$, as illustrated in Figure 2.5. The expected tracking performance from Monte Carlo simulation of the CMS inner detector is shown in Figure 2.6. The transverse momentum resolution is about 1-2% up to $|\eta| \approx 1.6$ for high-p_T tracks ($\approx$ 100 GeV). For high-momentum tracks, the resolution

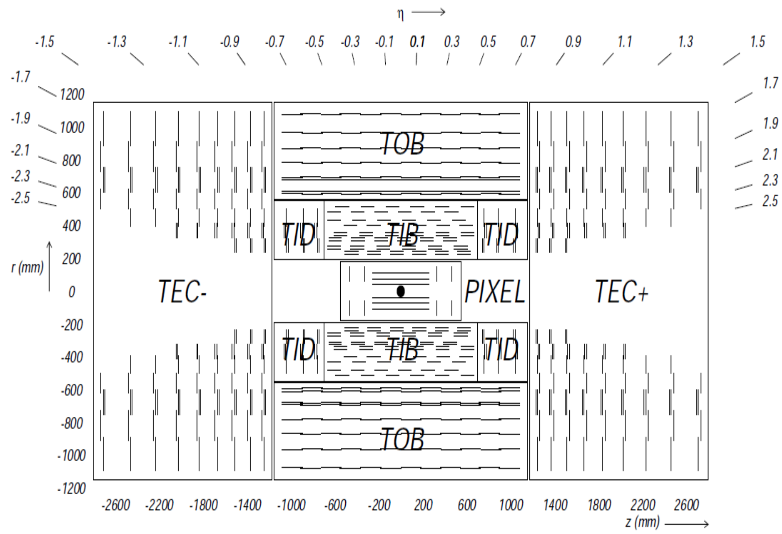

Figure 2.4: A schematic r-z view of the CMS tracker.

of the transverse impact parameter is about 10 μm, and a corresponding longitudinal impact parameter resolution of 20 to 40 μm.

2.2.2 Electromagnetic Calorimeter

The CMS electromagnetic calorimeter (ECAL) is a homogeneous calorimeter made of lead tungstate ($PbWO_4$) crystals and photodetectors as shown, in Figure 2.7. It consists of a barrel and two endcap regions. There is a preshower detector installed in front of each endcap calorimeter. In order to operate in the LHC environment, several requirements needed to be met in the design of the electromagnetic calorimeter.

- Fast response,

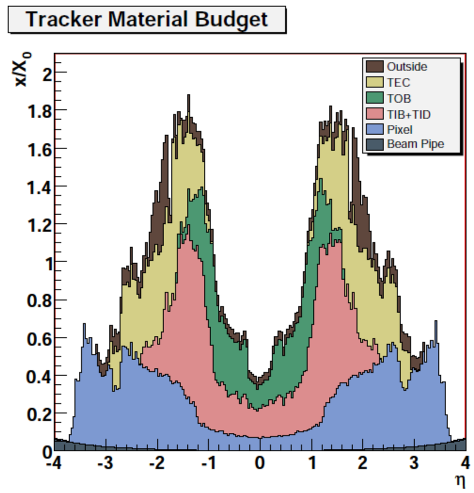

Figure 2.5: Material budget of the CMS tracker in radiation lengths as a function of η.

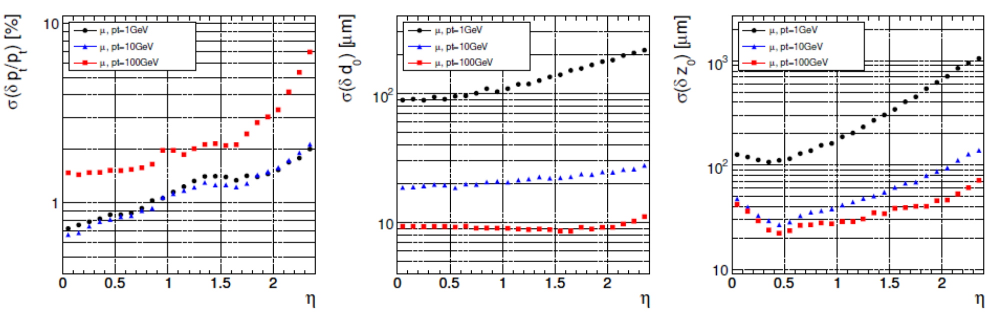

Figure 2.6: The expected CMS tracker transverse momentum (left), transverse impact parameter (middle), and longitudinal impact parameter (right) resolutions versus $|\eta|$ for single muons with transverse momenta of 1, 10 and 100 GeV, as predicted from Monte Carlo simulation.

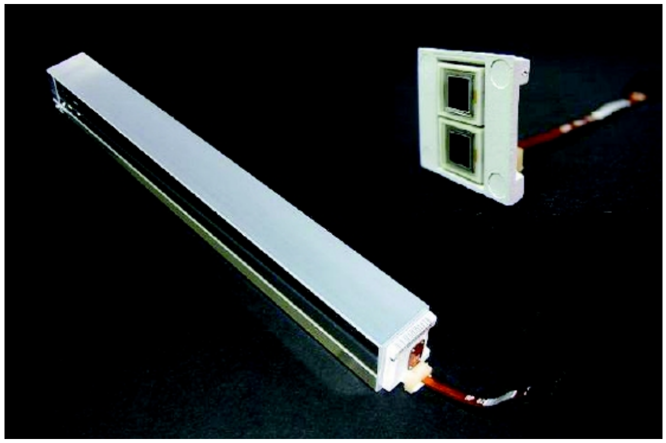

Figure 2.7: A $PbWO_4$ crystal with an avalanche photodiode.

- Fine granularity,
- Ability to operate in high levels of radiation,
- Ability to operate in a high magnetic field.

The characteristics of the $PbWO_4$ crystals such as high density (8.28 g/cm^3), short radiation length X_0 (0.89 cm) and small Moliere radius (2.2 cm) allow the ECAL to be a finely granular and compact calorimeter. When electrons and photons pass through the crystals, blue-green scintillation light is emitted as a result of the electromagnetic shower. About 80% of the light is emitted within 25 ns, which corresponds to the LHC design bunch-crossing time. The scintillation photons are spatially well-defined because of the short radiation length and small Moliere radius of the crystals. The photons are then collected by photodetectors, converted into electrical signals, and recorded by the data acquisition system.

The ECAL barrel (EB) covers the range $|\eta| < 1.479$. The crystal granularity of the barrel is (2×85)-fold in η and 360-fold in ϕ. Each crystal has a cross section of 0.174×0.174 in η-ϕ, corresponding to $22 \times 22\ mm^2$ at the front face of the crystal. The crystal length is 230 mm, corresponding to 25.8 radiation lengths.

The endcaps of the ECAL (EE) cover the pseudorapidity range $1.479 < |\eta| < 3.0$ and begin 315.4 cm away from the interaction point in longitudinal distance. Each endcap has two halves and consists of 5×5 crystals (supercrystals) arranged in the x-y plane. The crystals have a front face cross section of $28.6 \times 28.6\ mm^2$ and a length of 220 mm ($24.7X_0$).

The photodetectors used with the crystals need to have a fast response time, be radiation tolerant and able to operate in a 4 T magnetic field. Hence, photodetectors were specially designed and developed for the CMS ECAL. Avalanche photodiodes (APDs) are used in the barrel region and vacuum phototriodes (VPTs) in the endcaps. Since the number of scintillation photons emitted by the crystals and the amplification of the photodetectors are temperature dependent, the ECAL needs to be kept at a constant working temperature of 18°C.

The preshower detector is located in the endcap region within $1.653 < |\eta| < 2.6$. It is a two-layers sampling calorimeter with a total thickness of 20 cm. It consists of a $2X_0$ lead radiator in front of the first silicon strip sensor plane, and another $1X_0$ lead radiator, followed by the second sensor plane. The strips of the two sensor planes are orthogonal in order to cover all the area of the lead radiators. The purpose of the preshower detector is to distinguish between single high-energy photons and closely spaced pairs of lower-energy photons from a neutral pion decay. The preshower detector also measures the first part of the electromagnetic shower profile and improves the precision of the spatial measurement of electrons and photons.

The energy resolution of the ECAL is measured to be between 1.6% and 2.2% in the barrel and 4.8% in the endcap [34]. The position resolution of the ECAL is measured to be $2.8(5) \times 10^{-3}$ rad in $\Delta\phi$ in EB (EE) and $1(2) \times 10^{-3}$ units in $\Delta\eta$ in EB (EE) [34].

2.2.3 Hadron Calorimeter

The hadron calorimeter (HCAL) is a nearly hermetic subdetector of CMS, designed to measure the signatures of quarks and gluons through the measurement of jets of charged and neutral particles (hadrons). The HCAL also provides an indirect measurement of the missing transverse energy flow that is the signature of neutrinos or other noninteracting new particles escaping the detector. The hadron calorimeter barrel (HB) and endcaps (HE) are sampling calorimeters made of repeated layers of brass absorber and scintillator. The outer barrel (HO) is located outside the magnetic solenoid to measure hadron showers that leak out the back of the HB. To extend the hermeticity of the hadron calorimeter system, the forward hadron calorimeters (HF) are employed at each end of CMS, extending the pseudorapidity coverage to $|\eta| = 5$. Figure 2.8 shows a longitudinal view of the hadron calorimeter.

The HB covers the range $|\eta| < 1.3$ and is divided into two half-barrel sections. Each section has 18 identical azimuthal wedges that are made of flat brass absorber plates. The granularity of the HB is $(\Delta\eta, \Delta\phi) = (0.087, 0.087)$. The HB effective thickness is 5.82 interaction lengths (λ_I) at $\eta = 0$ and increases to 10.6 λ_I at $|\eta| = 1.3$. When hadronic particles hit an absorber plate, in-

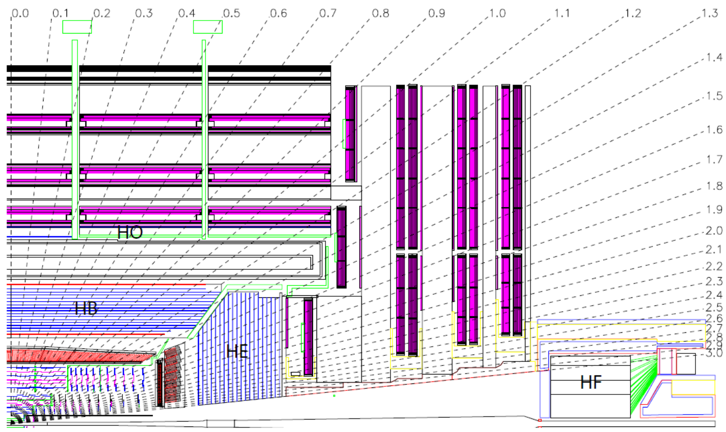

Figure 2.8: Longitudinal view of the CMS detector showing the locations of the HB, HE, HO, and HF calorimeters.

teractions can produce numerous secondary particles. When these secondary particles pass through successive layers of absorber, more interactions happen and result in a cascade or ”shower” of particles. The scintillator tiles inserted between the absorber plates emit blue-violet light when particles pass through them. Wavelength-shifting fibers placed in a machined groove in the scintillator absorb the blue light and shift it into green light. Then, clear optic fibers carry the green light to optical connectors, as shown in Figure 2.9. Signals from successive tiles are added optically to form ”towers”. The summed optical signals are converted into electronic signals by hybrid photodiodes (HPD).

The HE covers the range $1.3 < |\eta| < 3$. The absorbers and scintillators used in the HE are similar to those used in the HB but with a different geometry.

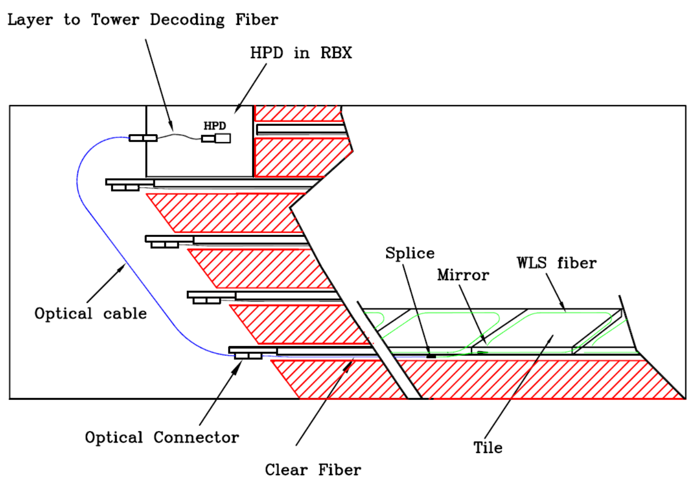

Figure 2.9: Schematic of the HB optics.

The granularity of the HE is $\Delta\eta \times \Delta\phi = 0.087 \times 0.087$ for $|\eta| < 1.6$ and $\Delta\eta \times \Delta\phi = 0.17 \times 0.17$ for $|\eta| \geq 1.6$. Because of the radiation environment and energy resolution concerns, towers 18−26 have two separate longitudinal read-out segments and towers 27−29 have three divisions in depth, as shown in Figure 2.10.

The outer radius of the EB (R = 1.77 m) and the inner radius of the magnet coil (R = 2.95 m) constrain the total amount of material that can be used in the HB to absorb hadronic showers. The total depth of the calorimeter system (EB plus HB) does not provide sufficient containment for hadron showers in the central pseudorapidity region. In order to measure the hadron shower energy deposited after the HB and improve the measurement of missing energy, the HO is placed outside the solenoid. The HO has 5 rings in the region $|\eta| < 1.3$. The central ring has two layers of scintillators, while

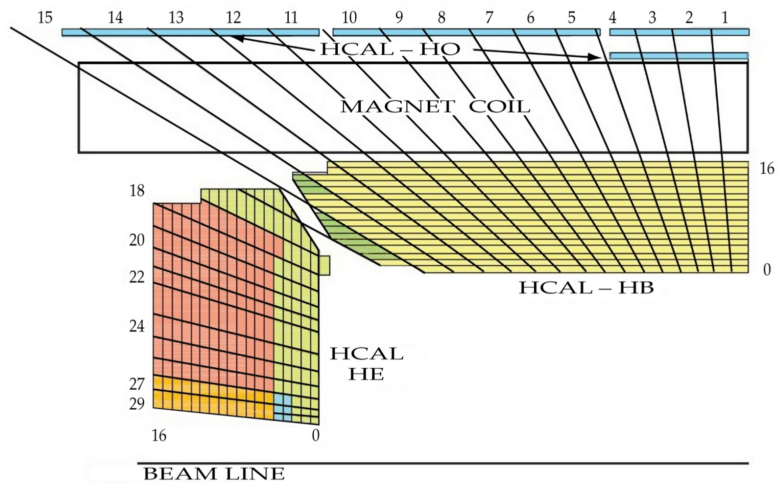

Figure 2.10: The HCAL tower segmentation in the r-z plane.

the other rings have a single layer. Each ring is divided into 12 identical ϕ sectors and each sector has 6 slices in ϕ, resulting in an η-ϕ granularity of 0.087×0.087. The HO increases the total depth of the calorimeter system to a minimum of 11.8 λ_I.

The HF calorimeter covers the range $3 < |\eta| < 5$, with a front face located at $z = \pm 11.2$ m from the pp interaction point. The HF is used to identify very-forward jets and improve the measurement of the missing transverse energy. Steel absorbers and quartz fibres are used in the HF in order to survive and operate in a very high level radiation environment. Charged particles emit photons when they pass through a quartz fibre with a phase velocity greater than the speed of light in the quartz, a phenomenon known as the Cherenkov effect. The fibers are insensitive to neutrons, which are the main products in the high-radiation LHC environment. In addition, there is a threshold velocity value below which there is no Cherenkov light emission that makes quartz fibres insensitive to low-energy particles. There are two functional longitudinal segments of the HF. Half of the quartz fibres run over the full depth of the absorbers, and the other half starts at a depth of 22 cm measured from the front of the HF. Showers from electrons and photons deposit most of their energy in the first 22 cm of absorber, while hadron showers produce approximately equal signals in both segments. The two separate readout segments allow the HF to distinguish the two types of showers.

The energy resolution of the HCAL is parameterized as $\sigma/E = 120\%/\sqrt{E} \oplus 6.9\%$ [33]. The missing transverse energy resolution is measured to be between 13 and 26 GeV by using the $Z \to \mu^+\mu^-$ events in data and Monte Carlo simulation sample [35].

2.2.4 Superconducting Magnet

The CMS superconducting magnet is a solenoid that is designed to provide a 4 T magnetic field in a free bore with a diameter of 6 m and length of 12.5 m. The magnet is made of 4-layer winding made from a stabilized reinforced $NbTi$ conductor. An electric current of 19 kA flows in the coil to produce the magnetic field inside the solenoid. The solenoid must be kept at a operating temperature of 1.8 K to allow the current to flow without resistance (superconductivity). The magnetic flux outside the central solenoid region is returned through a steel yoke composed of 5 barrel wheels and 6 endcap disks. The magnetic field bends the paths of charged particles emerging from the pp collisions. Measuring the curvature using the pixel and silicon tracker provides an accurate measurement of the momentum of the particles.

2.2.5 Muon System

Muon detection is one of the most important tasks of the CMS detector since muons can be final-state products in potential new physics scenarios and can provide good mass resolution because of having less radiative losses in the tracker material than electrons. Muons are identified using their property of being the only charged particles able to pass through the calorimeters and steel flux return with little interaction. The muon system is designed to have a wide angular coverage for muon detection and be able to measure the momentum of muons over the entire kinematic range of the LHC. As shown in Figure 2.11, three types of gaseous detectors are used in the muon system to trigger on, identify, and measure the momentum of muons.

The drift tube (DT) chambers cover the range $|\eta| < 1.2$ because of the low muon background rates and the uniform magnetic field in this region. When a muon passes through a drift cell, it ionizes the atoms of the gas mixture of 85% $Ar + 15\%\ CO_2$. Electrons then drift to the anode wires and the drift time is converted to the hit position of the muon. Figure 2.12 gives a sketch of a DT drift cell. The DT chambers form concentric cylinders and each sector has 4 stations interlaid between the steel yoke layers. A DT chamber consists of 3 (or 2) superlayers made of 4 consecutive layers of drift tubes. The 2 outer superlayers provide muon measurements in the r$-\phi$ plane with a resolution of 100 μm. The anode wires are orthogonal to the beam line in the inner superlayer, which provides a position measurement in the z-direction (an inner superlayer is not available in the fourth station). The superlayers

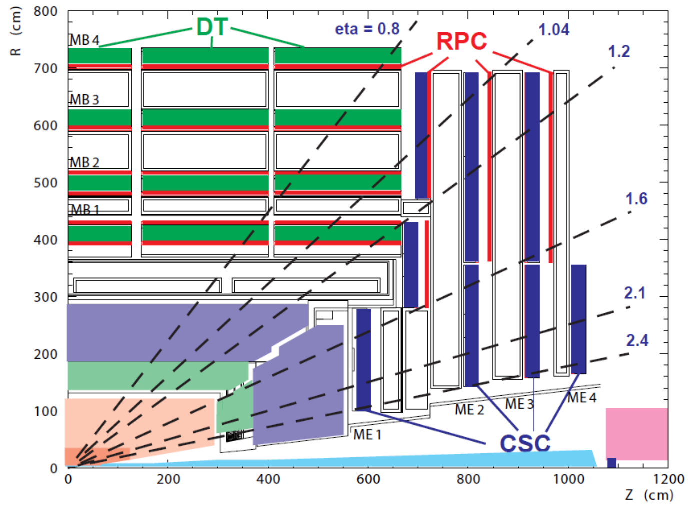

Figure 2.11: Layout of one quarter of the CMS muon system.

also provide excellent timing capability, with a time resolution less than the LHC bunch-crossing time of 25 ns.

In the endcap regions ($0.9 < |\eta| < 2.4$), cathode strip chambers (CSC) are used for the muon system due to higher muon background rates and a nonuniform magnetic field. There are 4 stations of CSCs in each endcap. The CSC are positioned perpendicular to the beam line, as shown in Figure 2.13. Each CSC is trapezoidal in shape and consists of 6 gas gaps. Each gas gap has a plane of cathode strips running radially outward and a plane of anode wires running approximately perpendicular to the strips. When a muon passes through the chamber, it ionizes the gas mixture of $40\%\ Ar + 50\%\ CO_2 + 10\%\ CF_4$. Electrons move to the anode wires, creating an avalanche of electrons and inducing an image charge pulse on the cathode strips. This provides the position and timing measurements of muons passing

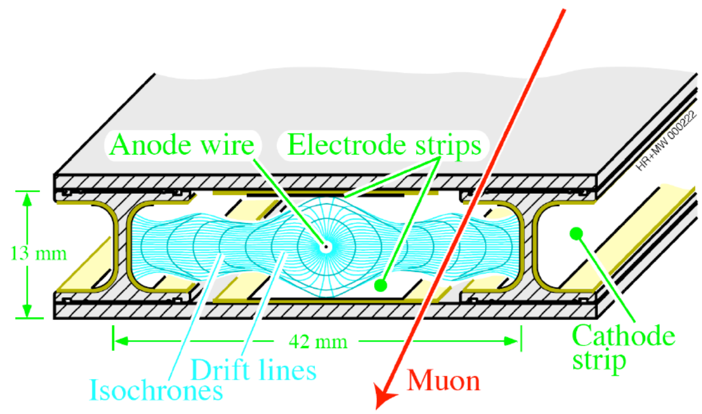

Figure 2.12: Sketch of a DT drift cell.

through the CSC. The spatial and time resolutions of the CSC system are $75 \sim 150$ μm and 5 ns, respectively.

The resistive plate chambers (RPC) are added in both the barrel and endcap ($|\eta| < 1.6$) regions as a complementary trigger system, in addition to those of the DTs and CSCs. There are 6 layers of RPCs embedded in the barrel muon system (two layers in each of the two innermost stations, plus one layer in each of the outermost stations) and 3 planes of RPCs in each endcap (one in each of the first three stations). RPCs are gaseous parallel-plate detectors that use the gas mixture of 96.2% $C_2H_2F_4 + 3.5\%$ $C_4H_{10} + 0.3\%$ SF_6. An electron avalanche is caused by muons passing through and ionizing the gas volume, which the electrons causing an avalanche that produces an image charge on metallic strips. This process delivers precise timing information with a resolution about 2 ns and a quick measurement of the muon momentum,

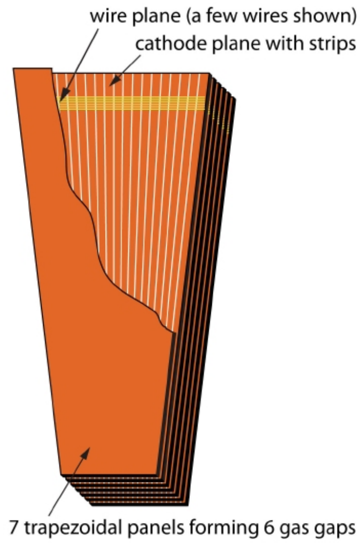

Figure 2.13: Layout of a cathode strip chamber.

which can be used by the trigger described in the next section.

2.2.6 Trigger and Data Acquisition

At the design luminosity of 10^{34} $cm^{-2}s^{-1}$, the LHC will operate at a 40 MHz bunch-crossing frequency, which corresponds to about one billion proton-proton interactions per second. It is impossible to read out and store the information from all the *pp* collisions. A trigger system is required to select the potentially interesting events and reduce the amount of stored data. The level-1 (L1) trigger consists of programmable electronics and is designed to reduce the 40 MHz bunch-crossing rate to an output rate of 100kHz. The next trigger level, the high level trigger (HLT), is a software filter system that reduces the stored data to a rate of $\sim$ 100 Hz.

There are local, regional and global triggers for both calorimeter and muon L1 triggers. The trigger primitive generators (TPG) obtain trigger tower transverse energy information by summing the energy deposited in the ECAL or the HCAL readout towers. The regional calorimeter trigger uses information from the TPGs and pattern logic to identify electron/photon candidates and measure transverse energy sums per calorimeter region which consists of 4×4 trigger towers. The global calorimeter trigger combines all information and determines the highest-rank calorimeter objects. The rank reflects the level of confidence attributed to the L1 parameter measurements.

All muon subsystems are used in the muon trigger. The DT chambers provide local trigger information in the form of track segments and hit patterns, while the CSCs provide track segments and also timing from the anode wires. The regional muon trigger consists of the DT and CSC track finders, which form tracks by joining the segments and assign physical parameters to them, such as the transverse momentum. In addition, the RPC chambers, which have good time resolution, deliver track candidates based on regional hit patterns. The global muon trigger then combines the information from all three muon subdetectors to improve the trigger efficiency, suppress background and reduce trigger rates.

The highest-rank objects determined by the global calorimeter and global muon triggers are transfered to the global trigger. Then the Global Trigger decides whether to keep an event for further evaluation by the HLT or to discard it. Figure 2.14 shows the architecture of the level-1 Trigger.

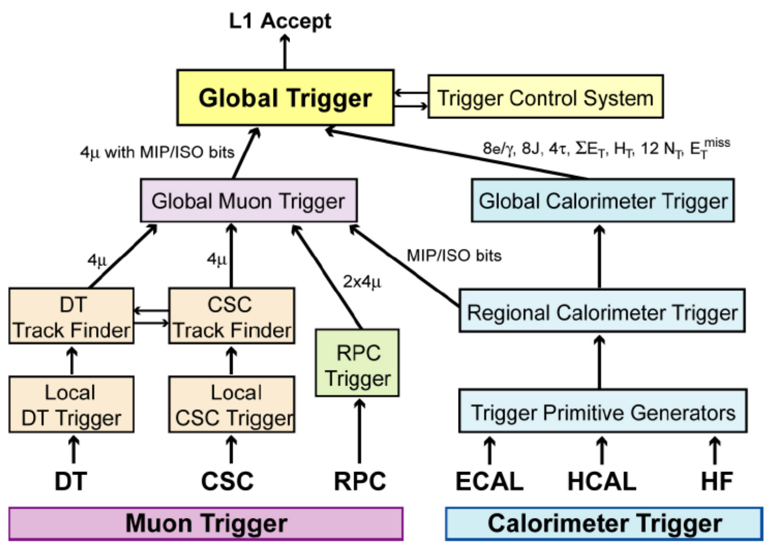

Figure 2.14: Architecture of the level-1 trigger logic.

Chapter 3

Event Reconstruction

The raw data collected by the CMS detector with the level-1 trigger are electronic signals with amplitude, timing, and position information. These raw data must be reconstructed as physics quantities and synthesized into the physical objects that can be used in the analysis. This chapter describes how event objects are reconstructed.

3.1 Track and Vertex Reconstruction

Since the proton bunches have a finite size, the interaction points of the proton-proton collisions are distributed over a region, referred to as the beamspot. After the beamspot is determined, the pixel vertices are determined from an initial round of track and vertex reconstruction using only pixel hits. The standard CMS track reconstruction [36,37,38,39] is performed by a combinatorial track finder (CTF), which proceeds in three stages: (1) seed generation, (2) track finding, and (3) track fitting. Pixel triplets of hits or pairs of hits with an additional constraint from the beamspot or a pixel vertex provides an initial estimate of the particle trajectory (seed). The seed is then propagated outward to search for compatible hits in other layers of the tracker system. When new hits are found, they are added to the trajectory and the track parameters and uncertainties are updated. The collection of compatible hits is fitted to obtain the best estimate of the track parameters in the final stage.

There are six iterations of the CTF. The 0^{th} and 1^{st} iterations use pixel triplets and pixel pairs as seeds to reconstruct the vast majority of high p_T-tracks. The 2^{nd} iteration uses pixel triplet seeds to reconstruct low-momentum tracks, while the 3^{rd} iteration is used to find displaced tracks. The final two iterations use seeds of silicon strip pairs to reconstruct tracks produced outside the volume of the pixel tracker. Between each iteration, hits associated with a track reconstructed in an earlier iteration are removed and only the remaining hits are used for the subsequent iteration. The reconstructed tracks are filtered based on the number of hits, the normalized χ^2 of the track hit, and the compatibility of the track originating from a pixel vertex to remove fake tracks at the end of each iteration.

The primary pp interaction vertices are reconstructed from prompt tracks based on their transverse impact parameter with respect to the beamspot [37, 39, 40]. The selected tracks are then clustered along the z axis by requiring a separation of at least 1 cm to the next cluster. Clusters containing at least two tracks are then fit with an adaptive vertex fit [41] to compute the best estimate of the vertex parameters. Each track associated with a vertex is assigned a track weight between 0 and 1 based on its compatibility with the vertex in the adaptive vertex fit. The number of degrees of freedom of a primary vertex is defined as

$$n_{dof} = 2 \sum_{i}^{n_{tracks}} w_i - 3, \tag{3.1}$$

where w_i is the weight of the i^{th} track. For example, an event with two tracks which are consistent with the common vertex has a primary vertex with number of degrees of freedom of 1.

3.2 Electron Reconstruction

Electrons interact with the materials of the tracking system and also deposit energy in the ECAL crystals. Due to the tracker materials, electrons may undergo bremsstrahlung emission before entering the ECAL, and the bremsstrahlung photons can then convert into an electron-position pair. This results in clusters of energy deposited in the ECAL with a narrow width in the η direction and spreading in the ϕ direction caused by the bending of the pairs in the magnetic field. The collection of associated ECAL clusters form what is called a supercluster.

Two complementary track-seeding algorithms are used for the electron reconstruction [42, 43, 44, 45]. The "ECAL-driven" algorithm is optimized for isolated electrons, while the "track-driven" seeding is suitable for low-p_T electrons and electrons inside jets. The ECAL-driven algorithm starts from superclusters with transverse energy $E_T > 4$ GeV and $H/E < 0.15$, where H is the energy deposited in the HCAL towers and E is the energy of the ECAL supercluster. These superclusters are matched to track seeds to build trajectories. The electron trajectory is determined by using a Gaussian sum filter

(GSF) algorithm in which the energy loss in each track layer is approximated by a weighted sum of Gaussian distributions. Electron candidates also need to pass the requirements $|\Delta\eta| < 0.02$ and $|\Delta\phi| < 0.15$, where $\Delta\eta$ and $\Delta\phi$ are the pseudorapidity and azimuthal angle differences between the position of the supercluster and the extrapolating of the electron track to the ECAL.

The tracker-driven algorithm uses all GSF tracks to produce superclusters by combing particle-flow clusters. Based on the GSF track, a tangent to a track is extrapolated at each tracker measurement layer to the ECAL to look for possible corresponding bremsstrahlung photons. The ECAL cluster matched with the outermost position extrapolated from the GSF track is defined as the electron cluster, which is finally added to the supercluster. Track-cluster matching observables, track p_T and η are combined to obtain a global identification variable using a boosted decision tree (BDT). A global identification variable > -0.4 from BDT is used to select electron candidates with the tracker-driven seeding algorithm.

3.3 Photon Reconstruction

Photons do not leave hits in the tracking system but deposit all their energy in the ECAL. The same clustering algorithms [45] are used to reconstruct the energy of photons and electrons. A hybrid algorithm is performed in the barrel region and a multi-5x5 algorithm is used in the endcaps to cluster the crystal energies. Both algorithms operate on a set of crystals sorted in descending order of E_T.

The hybrid algorithm consists of the following:

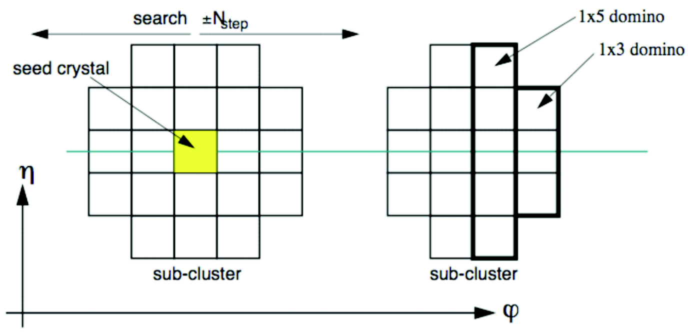

Figure 3.1: An illustration of the hybrid clustering algorithm.

- In the region of interest, the crystal with the largest energy deposit serves as the seed crystal. The E_T of the seed crystal must be greater than a threshold $E_T^{hybseed}$ to avoid low-energy background and noise contamination. In addition, the seed crystal must not belong to another cluster.
- A 5×1 set of crystals called a domino is chosen symmetrically in η-ϕ around the seed crystal.
- The previous step is repeated for all crystals with the same η as the seed crystal and with $\phi < \phi_{road}$ in each ϕ direction. The dominoes must have energy above a threshold E_{thresh} to be included in the cluster.
- Each disconnected subcluster is required to have a seed domino with energy greater than E_{seed}.

The hybrid algorithm is shown pictorially in Figure 3.1.

The multi-5x5 algorithm proceeds as follows:

- A crystal with $E_T > E_T^{seed}$ and that does not already belong to a cluster is chosen as the seed to the clustering process.
- The energy of the seed crystal must be a local maximum compared its energy to its four neighbors in a Swiss Cross pattern.
- A 5×5 matrix of crystals around the seed is built, but using only crystals that are not already assigned to other clusters.
- The outer 16 crystals of the 5×5 matrix can seed a new matrix to cover overlapping showers.

3.4 Muon Reconstruction

Muon reconstruction [46, 47] relies on both the tracker and muon system. Silicon tracks and standalone-muon tracks are independently reconstructed in the tracking and muon systems, respectively. Based on silicon tracks and standalone-muon tracks, there are three different muon reconstruction methods.

- Global muon: A standalone muon in the muon system is extrapolated outside-in to match a silicon track. Then a global muon track is fit by using the hits from the silicon track and the standalone-muon track. This method can improve the momentum resolution for high-transverse-momentum muons ($p_T \gtrsim 200\ GeV$) compared to the tracker-only fit.
- Tracker muon: All silicon tracks with $p_T > 0.5$ GeV and $p > 2.5$ GeV are assumed to be potential muon candidates and are extrapolated

inside-out to the muon system. The expected energy loss and the uncertainty on the muon trajectory due to multiple scattering are considered in this process. The muon is classified as a tracker muon when the extrapolated track matches at least one muon segment. This approach is more efficient for low-momentum muons ($p < 5$ GeV).

- Standalone muon: When the previous two reconstruction methods fail and only a standalone-muon track is found, the muon is classified as a standalone muon. Muons from cosmic rays are the main source of this kind of muons. Only about 1% of the standalone muons come from collisions.

3.5 Jet Reconstruction

Jets are the experimental signature of quarks and gluons. In other word, jets are sprays of hadrons due to the hadronization of quarks or gluons. Different types of jets are reconstructed based on which subdetectors are used and how the measurements of the subdetectors are combined. Calorimeter jets are reconstructed using only ECAL crystals and HCAL towers. The particle-flow (PF) algorithm [48,49] aims to reconstruct, identify and calibrate all particles in the event such as electrons, muons, photons, and charged hadrons, as well as neutral hadrons, by combining information from all subdetectors. PF jets are used in this analysis and more details of the PF jet reconstruction are described below.

A given particle can produce several particle-flow elements in the various subdetectors. These PF elements must be connected to fully reconstruct each single particle. A link algorithm is performed on the PF elements that produces blocks of elements. For each block, if a global muon is linked to a particle-flow muon, the corresponding track is removed from the block. Each track-driven identified electron produces a particle-flow electron. The corresponding track and ECAL clusters are then removed from the block. The remaining tracks in the block are defined as particle-flow charged hadrons. The momentum and energy of the charged hadrons are determined directly from the track momentum by using a charged-pion mass hypothesis. Finally, the remaining ECAL and HCAL clusters which are not linked to any tracks give rise to particle-flow photons and particle-flow neutral hadrons, respectively.

Particles are then clustered into jets via a sequential clustering algorithm [50]. The distance d_{ij} between entities (particles, pseudo-jets) i and j and the distance d_i are defined:

$$d_{ij} = min(k_{ti}^{2p}, k_{tj}^{2p})\frac{\Delta_{ij}^2}{R^2} \tag{3.2}$$

$$d_i = k_{ti}^{2p}, \tag{3.3}$$

where $\Delta_{ij}^2 = (y_i - y_j)^2 + (\phi_i - \phi_j)^2$ and k_{ti}, y_i and ϕ_i are the transverse momentum, rapidity and azimuthal angle of particle i, respectively. R is the jet radius parameter and p is the relative power of the energy-versus-geometrical (Δ_{ij}) scales.

If $d_{ij} < d_i$, entities i and j are recombined into a single pseudo-jet, weighting the position of the jet by the momenta of the entities. If $d_i < d_{ij}$, entity i is called a jet and removed from the list of entries. This procedure is iterated until no entries are left.

The case of $p = 1$ is referred to as the inclusive-k_T algorithm, while $p = 0$ corresponds to the inclusive-Cambridge/Aachen algorithm, and $p = -1$ as the anti-k_t algorithm. The anti-k_t jet-clustering algorithm with $R = 0.5$ is used in this analysis. One feature of the anti-k_t algorithm is that soft particles do not modify the shape of the jet, while hard particles do. The jet boundary of anti-k_t algorithm is resilient with respect to soft radiation but flexible with respect to hard radiation. In addition, the anti-k_t algorithm is infrared and collinear (IRC) safe. This means that the output of the jet reconstruction is robust against the presence of soft gluon emissions and when the energy of a parton is distributed among two collinear particles.

3.5.1 Jet Energy Corrections

Because the energy response of the calorimeters are not perfectly linear or uniform, the measured jet energy needs to be corrected [51]. Additional contributions from noise in the electronics and from multiple interactions occurring in the same bunch-crossing called pileup (PU), also need to be corrected for. The jet energy corrections (JEC) are factorized with three different corrections applied successively to each jet. The level-1 (L1Fast) offset correction subtracts energy originating from noise and PU. The goal of the level-2 (L2) relative correction is to equalize the response of all jets as a function of η, with respect to the average response in the calorimeter barrel region. Finally, the level-3 (L3) absolute correction flattens the absolute jet response of the calorimeter versus the jet p_T. All corrections are derived from data using dijet and γ/Z + jet events.

3.6 Reconstruction of the Missing Transverse Energy

Neutral weakly interacting particles such as neutrinos or some BSM particles that are produced in the pp collisions will not interact inside the detector. The presence of such particles will produce an imbalance in the total reconstructed momentum in an event. The magnitude of the imbalance in the transverse plane is known as the missing transverse energy (MET), denoted by E_T^{miss}. Different types of MET are reconstructed: calorimeter MET (caloMET), track-corrected MET (tcMET) and particle-flow MET (PFMET). Since particle-flow MET is measured using all the particles reconstructed in the detector, PFMET has an overall better resolution and is therefore used in this analysis. The particle-flow MET is defined as the magnitude of the negative vector sum of the transverse momentum of all particle-flow particles:

$$E_T^{miss} = | -\sum_i \vec{P}_T^i | \quad , \tag{3.4}$$

where the sum is over all particle-flow particles in an event.

Chapter 4

Search for New Physics

4.1 Analysis Overview

As mention in Section 1.2.2, the new-physics signal that we are looking for consists of two photons and large missing transverse energy in the final state. For example, an event with two photons and large missing transverse energy in the detector is illustrated in Appendix A. Several SM processes can produce or mimic this final state. We group SM backgrounds into two categories. One type of background does not have intrinsic E_T^{miss}, and the other type does have real E_T^{miss}.

Direct two-photon final states can be produced by quark-antiquark, quark-gluon, antiquark-gluon and gluon-gluon scattering. We refer to this kind of background as quantum chromodynamics (QCD) events. Figure 4.1 shows some examples of Feynman diagrams for diphoton production through QCD processes. In addition to direct diphoton production, QCD events with one

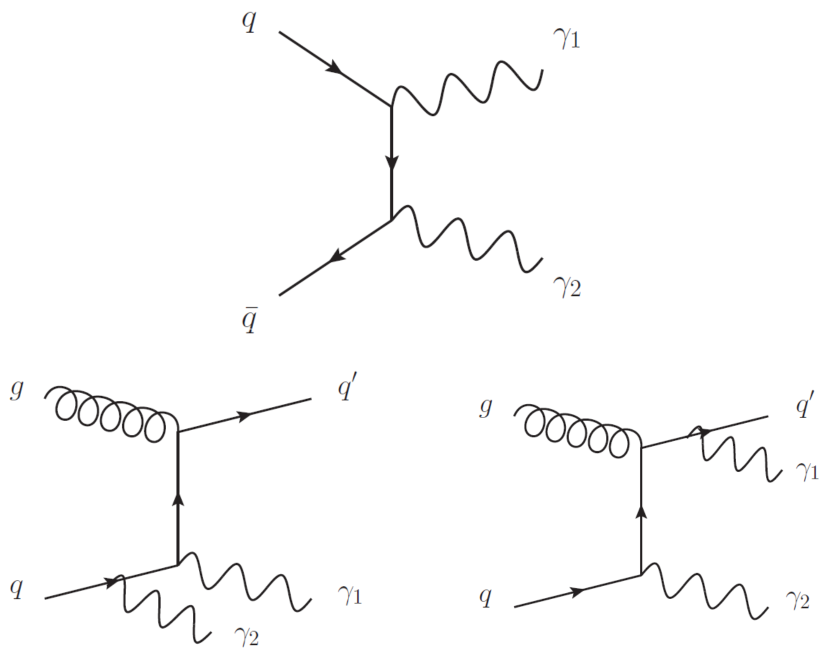

Figure 4.1: Examples of Feynman diagram for QCD diphoton production at leading-order (top) and next-to-leading-order (bottom).

real photon and jets, where a jet is misidentified as a photon, can also result in two reconstructed photons in the final state. It is also possible that two photons in QCD events are both mimicked by jets. Because of the high production rate for QCD events, the dominant background in this analysis is from QCD. Although there is no intrinsic E_T^{miss} in QCD events, the large hadronic activity in QCD events and the finite energy resolution of detector can result in a sizable measured E_T^{miss}. We will use two control samples to model the E_T^{miss} distribution from QCD background events.

The other type of background comes from events with real E_T^{miss} due to the presence of neutrinos. This background is dominated by the $W\gamma$ process, where the photon can be a real photon or a misidentified jet. When the

W boson decays into an electron and a neutrino, the neutrino becomes the source of E_T^{miss}. If the electron is misidentified as a photon, $W\gamma$ events will result in two photons in the final state. This type of background is referred as the electroweak (EWK) background. A straightforward method is used to estimate the EWK background. First, the electron misidentification rate is determined from the data. Then, a sample of events that contain at least one electron and one photon is scaled by the electron misidentification rate to estimate the electroweak contribution.

The $Z\gamma \rightarrow ee\gamma$ process, where one electron is misidentified as a photon, also produces events with two photons. However, there is no true E_T^{miss} for such a process, and the contribution is partially accounted for by the EWK background estimation. Other standard model processes contributing to the diphoton final state with true E_T^{miss} are $Z\gamma\gamma \rightarrow \nu\nu\gamma\gamma$, $W\gamma\gamma \rightarrow l\nu\gamma\gamma$, $t\bar{t}\gamma\gamma$ and $Z\gamma\gamma \rightarrow \tau\tau\gamma\gamma$, where the τ decays to $e(\mu)\nu\nu$ or $\pi\nu$. However, the cross sections for such channels are quite small and the contributions from these processes are negligible.

4.2 Definition of Selection Variables

The selection variables used in this analysis are the following:

- $\Delta R = \sqrt{(\Delta\phi)^2 + (\Delta\eta)^2}$, the cone radius, where $\Delta\phi$ and $\Delta\eta$ are the differences of azimuthal angle and pseudorapidity between two interested objects, respectively.
- ECAL isolation: The E_T of the ECAL crystals in a cone of $\Delta R = 0.3$, centered around the ECAL supercluster position, are summed. The

summation excludes a region consisting of a strip of width 0.087 in the η direction and an inner cone with $\Delta R = 0.06$, as illustrated in Figure 4.2.

- HCAL isolation: The E_T of the HCAL towers in a cone of $\Delta R = 0.3$, centered at the ECAL supercluster position, are summed excluding an inner cone with radius $\Delta R = 0.15$.

- Track isolation: The p_T of tracks in a cone of $\Delta R = 0.3$, centered around the line joining the selected primary vertex to the ECAL supercluster position, are summed. The summation excludes a region consisting of a strip of width 0.03 in the η direction and an inner cone with $\Delta R = 0.04$.

- Combined isolation (I_{comb}) = ECAL isolation + HCAL isolation + Track isolation.

- H/E : Ratio of the energy measured in the HCAL to the ECAL supercluster energy within a cone of $\Delta R = 0.15$.

- $\sigma_{i\eta i\eta}$: Shower shape variable of the electromagnetic cluster computed with logarithmic weights as

$$\sigma^2_{i\eta i\eta} = \frac{\sum_i^{5\times 5} w_i(\eta_i - \bar{\eta}_{5\times 5})^2}{\sum_i^{5\times 5} w_i}, \quad w_i = max(0, 4.7 + ln\frac{E_i}{E_{5\times 5}}),$$

  where E_i and η_i are the energy and pseudorapidity of the ith crystal within the 5×5 electromagnetic cluster and $E_{5\times 5}$, and $\bar{\eta}_{5\times 5}$ are the total energy and average pseudorapidity of the entire 5×5 cluster.

- R9: The ratio of the total energy in a 3×3 crystal cluster around the seed crystal and the total supercluster energy.

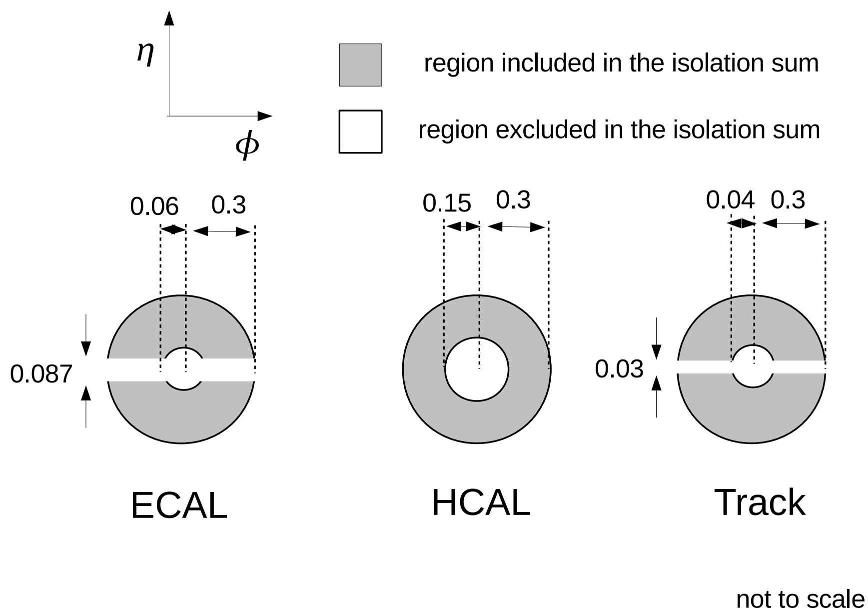

Figure 4.2: Illustration of the isolation sum cones for ECAL, HCAL and track isolation variables.

4.3 Signal Monte Carlo Simulation

GGM signal Monte Carlo simulation samples were generated to study the kinematic distributions and the phenomenological interpretation of the results of this analysis. The parameters considered in the production of the signal samples are chosen to simplify the parameter space. They include: M_1, the mass of the bino-like neutralino, M_2, the mass of the wino-like neutralino, and M_3, the mass of the gluino. The mass spectra are chosen so that the mass of irrelevant particles decoupled from these three, in order to only produce events with photons in the final state.

4.3.1 Signal Monte Carlo Simulation Production

The technical details of the signal production are summarized below:

- Superpartner spectra of the GGM scenarios were generated using SuSpect 2.41 [52] with the decay table from SDECAY [53].
- The decays of NLSPs and co-NLSPs were handled by Pythia [54], where the gravitino was forced to be the LSP.
- Parton distribution functions (PDF) were obtained from CTEQ6L1 [55] via LHAPDF [56].
- Next-to-leading-order (NLO) K-factors, renormalization scale uncertainties, and PDF uncertainties were calculated using PROSPINO [57].

4.3.2 Signal Scans

Five different phase-space scenarios in the form of two-dimensional (2D) GGM signal scans were produced. They include:

Gluino-squark grid for bino-like neutralino: M_1 was set to 375 GeV, and M_2 was decoupled at 2000 GeV. The gluino and light squark masses were varied in a 2D grid.

Gluino-bino grid: M_2 was decoupled at 2000 GeV, and squarks were decoupled at 5000 GeV. The gluino and bino masses were varied in a 2D grid, while the gluino mass was constrained to be larger than M_1 in order to maintain the bino as the NLSP.

Gluino-squark grid for wino-like neutralino: M_1 was decoupled at 5000 GeV, and M_2 was set to 375 GeV. The gluino and light squark masses were varied in a 2D grid.

Gluino-wino grid: M_1 was decoupled at 5000 GeV, and squarks were decoupled at 5000 GeV. The gluino and wino masses were varied in a 2D grid, while the gluino mass was constrained to be larger than M_1 in order to maintain the wino as the NLSP.

Wino-bino grid: Gluino and squark masses both were decoupled at 5000 GeV. Wino and bino masses were varied in a 2D grid, while M_2 was constrained to be larger than M_1 in order to maintain the bino as the NLSP.

The mass parameters for these GGM signal scans are summarized in Table 4.1.

Table 4.1: The range of different mass parameters in GeV for the GGM signal scans.

Scan	Gluino	Squark	Bino	Wino
Gluino-Squark (Bino)	400-2000	400-2000	375	2000
Gluino-Squark (Wino)	400-2000	400-2000	5000	375
Gluino-Bino	300-1500	5000	50-1500	2000
Gluino-Wino	300-1500	5000	5000	100-1000
Wino-Bino	5000	5000	50-1000	115-1000

4.3.3 Properties of Signal Events

To demonstrate the properties of the signal events, we take three signal points of the gluino-squark scans and study the general kinematic distributions of the signal events. For these three signal points, the bino-like neutralino mass is 375 GeV and the gluino mass is selected to be fixed at 1720 Gev while the squark masses are varied from 600, 1100 to 1600 GeV. For kinematic variables associated with an individual object (photon), all photon requirements listed in section 4.6.2 are applied except the variable itself. These N-1 distributions are shown in Figures 4.3 and 4.4. There are not many differences between the N-1 distributions of the different signal points. This is expected since photons originating from the signal should have the same kinematic properties. However, we can expect the differences between the N-1 distributions of the photon p_T and combined isolation for different signal points, as shown in Figure 4.5. In the selected three signal points, the gluino mass is greater than the squark mass. The gluino decays into a squark and a jet, then the squark decays into a bino-like neutralino and another jet and finally, the neutralino decays into a photon and a gravitino. The heavier of a squark is, the more energy photons in the final state can have. Higher photon p_T also implies possible border distribution of the combined isolation. For kinematic variables associated with an event such as E_T^{miss}; Di-EMPt, the magnitude of the vector sum of the p_T of the selected photons; HT, the scalar sum of the p_T of the selected jets; MHT: the vector sum of the p_T of the selected jets; the numbers of jets; and the p_t of the leading jet are shown in Figure 4.6 after the photon selection requirements listed in Section 4.6.2 are applied. As explained above, a squark with heavier mass can result in more energetic photons, gravitions, and jets in the final state. The distributions associated with these variables are expected to be border for signal points with a heavier squark mass.

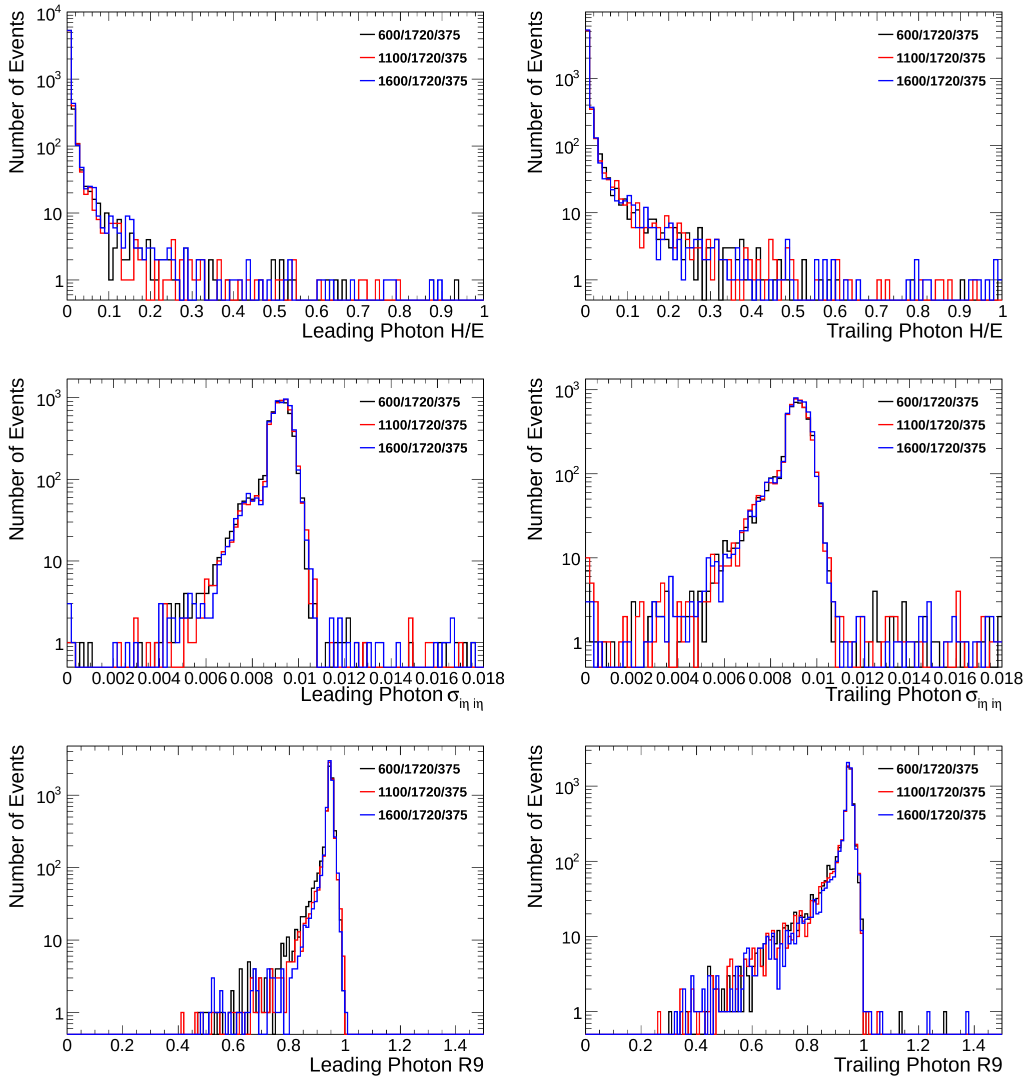

Figure 4.3: The N-1 distributions of the signals with squark/gluino/bino-like neutralino mass in GeV for the leading photon (left) and the trailing photon (right): H/E (top row), $\sigma_{i\eta i\eta}$ (middle row) and $R9$ (bottom row).

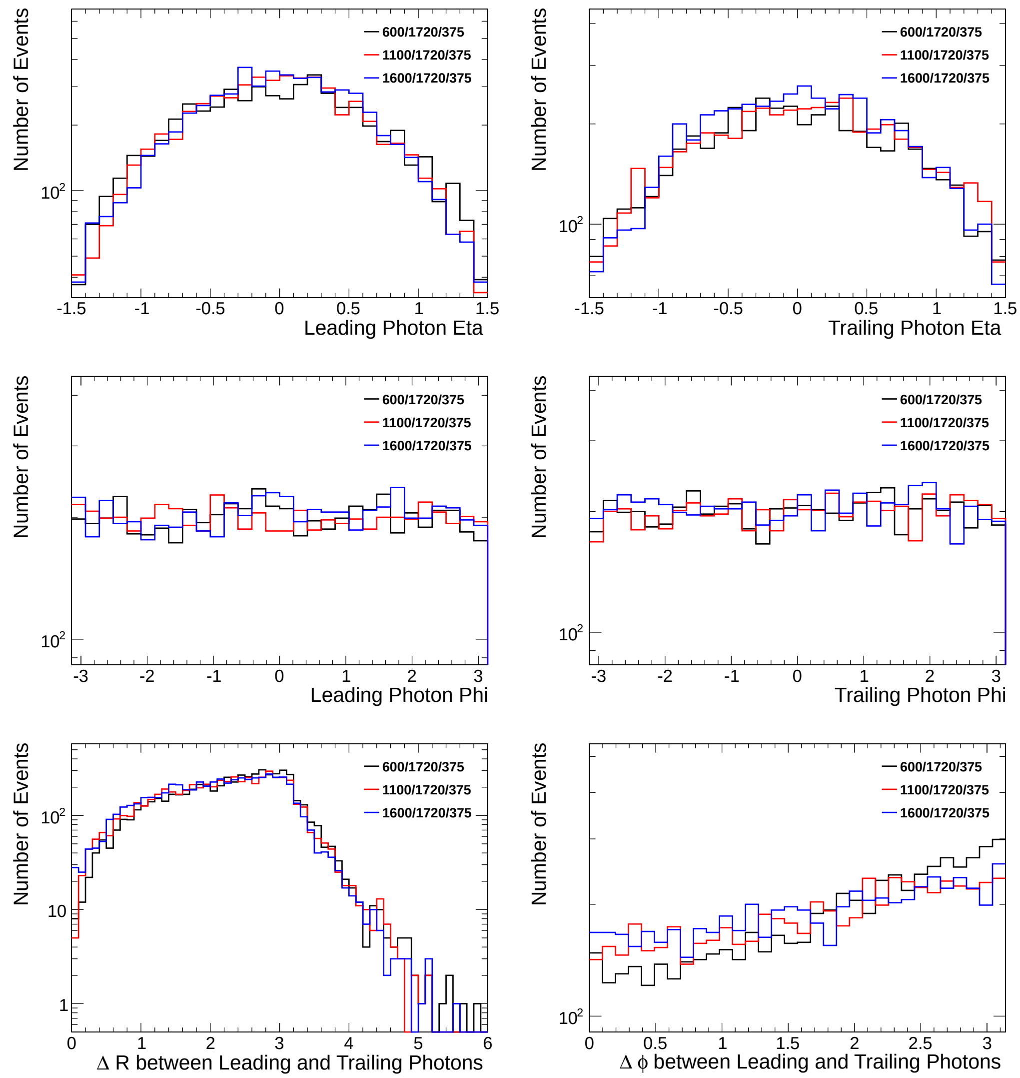

Figure 4.4: The N-1 distributions of the signals with squark/gluino/bino-like neutralino mass in GeV for the leading photon: η (top left) and ϕ (middle left). Trailing photon: η (middle left) and ϕ (middle right). ΔR (bottom left) and $|\Delta\phi|$ (bottom right) between the leading and trailing photons.

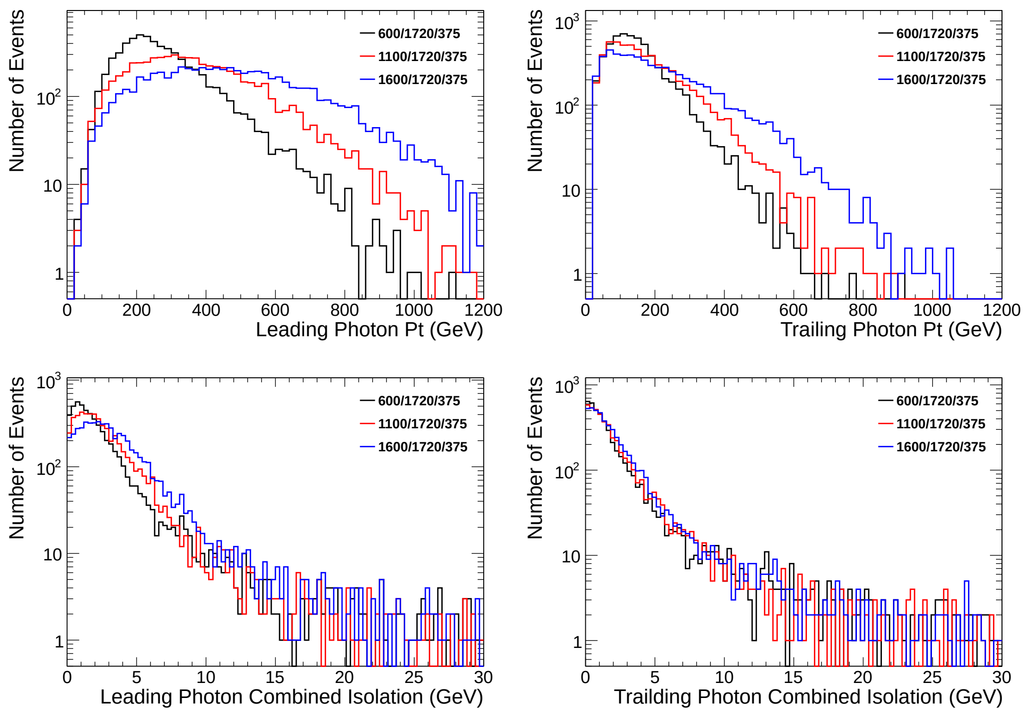

Figure 4.5: The N-1 distributions of the signals with squark/gluino/bino-like neutralino mass in GeV for the leading photon (left) and trailing photon (right): p_T (top row), combined isolation (bottom row).

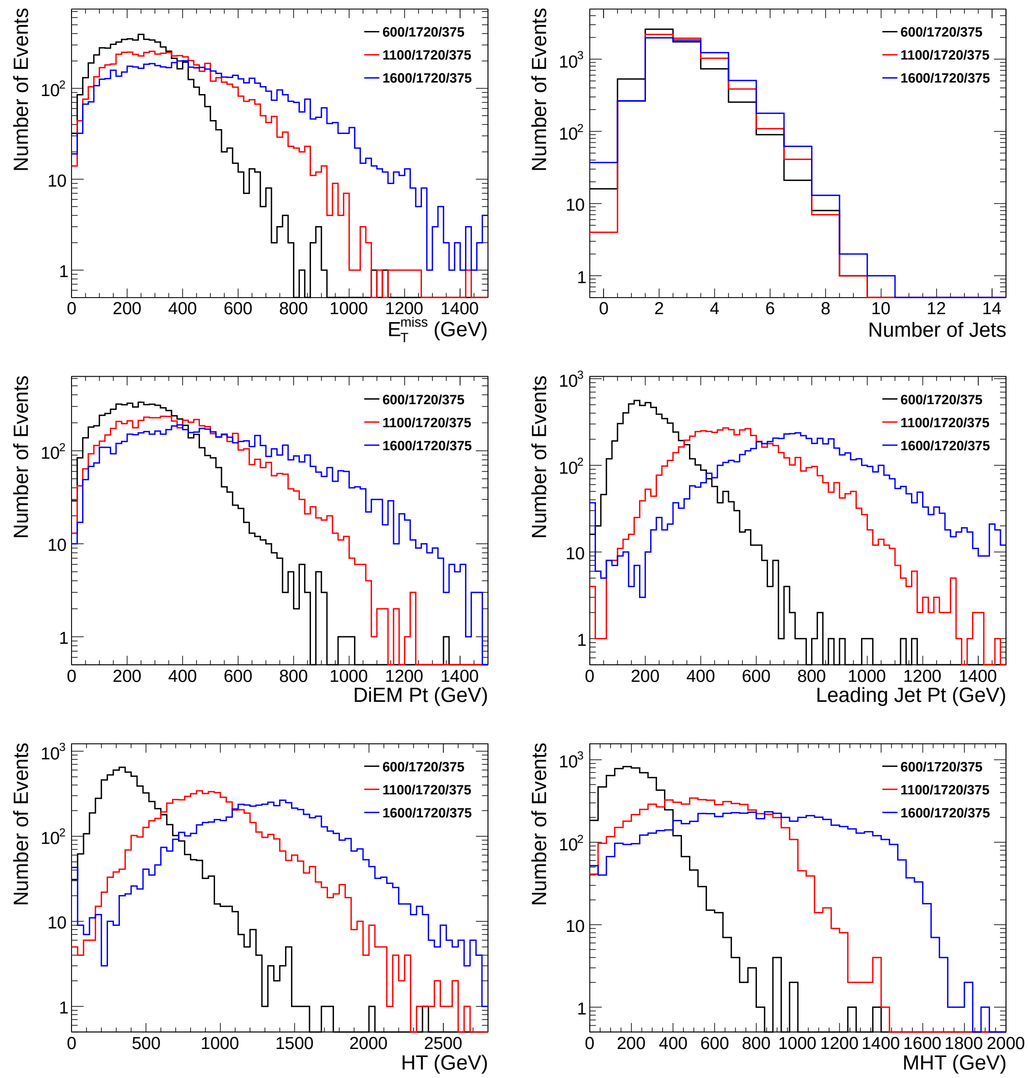

Figure 4.6: Distributions of the signals with squark/gluino/bino-like neutralino mass in GeV: E_T^{miss} (top left), Number of jets (top right), Di-EMPt (middle left), Leading jet p_T (middle right), HT (bottom left), and MHT (bottom right).

4.4 Trigger

Data are accumulated after the selection of the triggers. The design of the triggers is the first task of an analysis. The strategy of the trigger design is to maximize the acceptance of the signals, while keeping the trigger bandwidth within reasonable rates. Diphoton triggers are used in this analysis.

Each diphoton high-level trigger (HLT) must be initiated by at least one level-1 (L1) electron/photon seed. The reason for requiring only one L1 seed instead of two is to reduce the dependency of the trigger efficiency on the inefficiency of the L1. Suppose the L1 seed efficiency is ϵ_{L1}, then the overall L1 trigger efficiency for a diphoton path will be:

$$\epsilon^{L1}_{diphoton} = 1 - (1 - \epsilon_{L1}) \times (1 - \epsilon_{L1}) = \epsilon_{L1}(2 - \epsilon_{L1}). \tag{4.1}$$

If we require two L1 seeds, the overall L1 trigger efficiency for a pair of photon candidates will be:

$$\epsilon^{L1}_{diphoton} = \epsilon_{L1} \times \epsilon_{L1} = \epsilon^2_{L1}. \tag{4.2}$$

The L1 trigger efficiency $\epsilon^{L1}_{diphoton}$ in Eq. (4.1) is always equal to or larger than that in Eq. (4.2).

Table 4.2 shows a list of diphoton triggers used in this analysis, where the numbers following "Photon" are the E_T requirements for the leading and trailing photon, respectively. The calorimeter identification requirements for `CaloIdL`, where "`L`" means "loose", are:

- H/E < 0.15 (EB), H/E < 0.1 (EE)

Table 4.2: List of triggers used in this analysis.

	Triggers
L1 Seed	L1SingleEG20
HLT (A)	HLT_Photon26_IsoVL_Photon18(v1)
	HLT_Photon36_CaloIdL_Photon22_CaloIdL(v1-v4)
	HLT_Photon36_CaloIdL_IsoVL_Photon22_CaloIdL_IsoVL(v1-v7)
HLT (B)	HLT_Photon36_CaloIdL_IsoVL_Photon22_R9Id(v1-v6)
	HLT_Photon36_R9Id_Photon22_CaloIdL_IsoVL(v1-v7)
	HLT_Photon36_R9Id_Photon22_R9Id(v1-v3)

- $\sigma_{i\eta i\eta} < 0.014$ (EB), $\sigma_{i\eta i\eta} < 0.035$ (EE)

The isolation requirements for `IsoVL`, where "`VL`" stands for "very loose", are:

- ECAL isolation $< 0.012 E_T + 6.0$ GeV
- HCAL isolation $< 0.005 E_T + 4.0$ GeV
- Track isolation $< 0.002 p_T + 4.0$ GeV

The `R9Id` requirement is:

- R9 > 0.8

All triggers listed in Table 4.2 are not prescaled, which means that all events passing these triggers were recorded.

4.4.1 Trigger Efficiency

To determine the HLT trigger efficiency, we use a trigger with requirements much looser than the selection criteria (base trigger). We apply the offline cuts to the events passing the base trigger. We then measure the efficiency of the selected events to pass the triggers used in the analysis (target trigger). The trigger efficiency ϵ is defined as:

$$\epsilon = \frac{\text{Number of events passing (base trigger } + \text{offline cuts } + \text{target trigger)}}{\text{Number of events passing (base trigger } + \text{offline cuts)}}, \quad (4.3)$$

where the offline cuts are:

- requirements of base trigger to reconfirm the condition of the base trigger
- H/E < 0.05
- $\sigma_{i\eta i\eta} < 0.011$
- R9 < 1
- Combined isolation < 6 GeV
- E_T threshold of the leading or trailing photon

Figure 4.7 shows the trigger efficiency as a function of the p_T of the leading and trailing photons for the `HLT_Photon36_CaloIdL_Photon22_CaloIdL` (top) and `HLT_Photon36_CaloIdL_IsoVL_Photon22_CaloIdL_IsoVL` (bottom) triggers. The base triggers are `HLT_Photon26_CaloIdL_Photon18_CaloIdL` and `HLT_Photon26_CaloIdL_IsoVL_Photon18_CaloIdL_IsoVL`, respectively. It is evident that the trigger efficiency is on its plateau when applying a selection

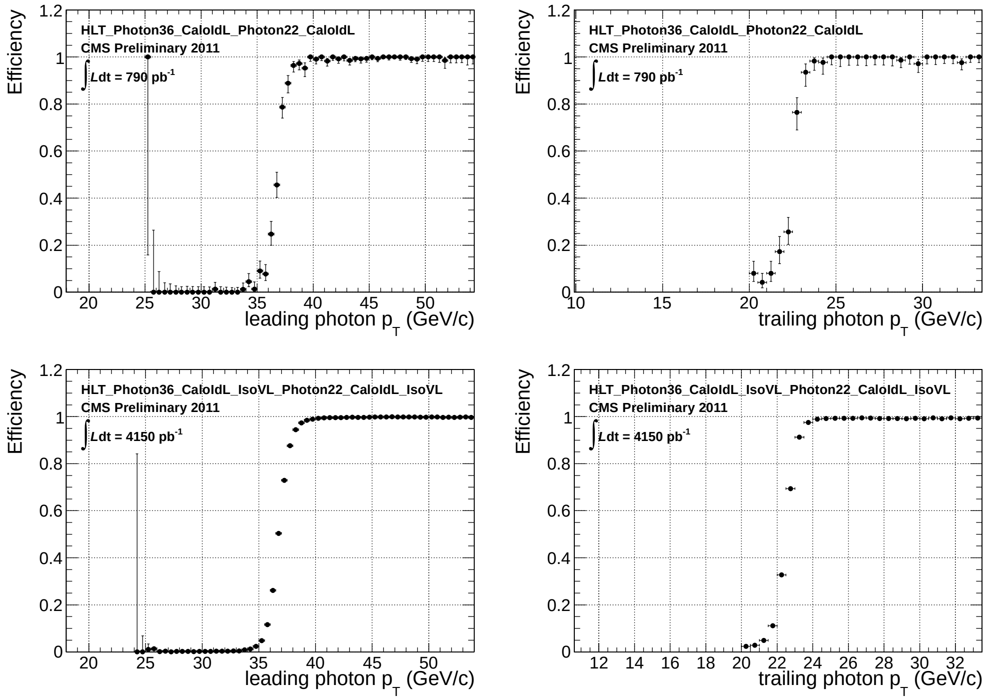

Figure 4.7: Turn-on curves of the trigger efficiency versus the p_T for the `HLT_Photon36_CaloIdL_Photon22_CaloIdL` (top) and `HLT_Photon36_CaloIdL_IsoVL_Photon22_CaloIdL_IsoVL` (bottom) triggers for the leading photon (left) and the trailing photon (right).

requirement of 40 GeV on the leading photon and 25 GeV on the trailing photon.

4.5 Datasets

The LHC delivered *pp* collision data with an integrated luminosity of 6.10 fb^{-1} during 2011. This analysis uses all the data collected by CMS, corresponding to an integrated luminosity of 5.56 fb^{-1}, as shown in Figure 4.8. The data were reconstructed with CMS software versions `CMSSW_4_2_4` and

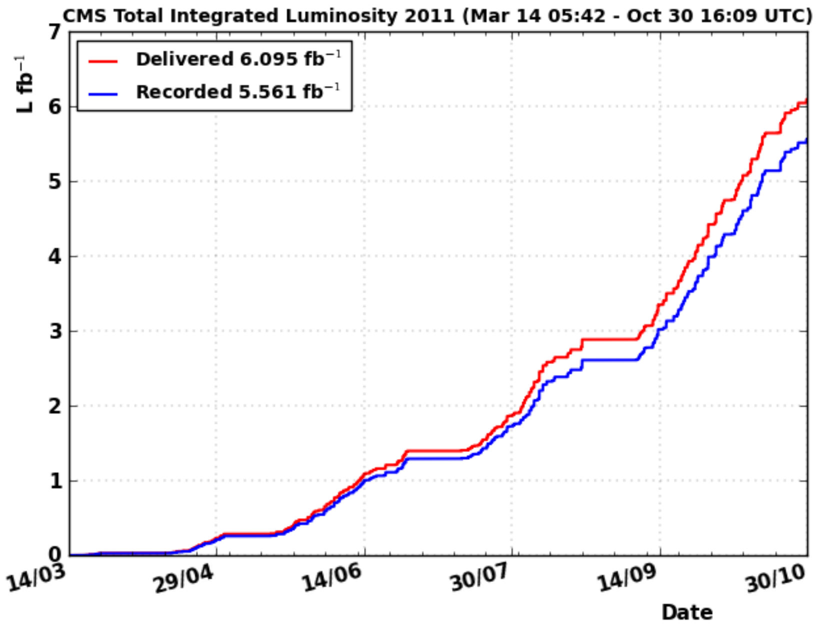

Figure 4.8: CMS delivered and recorded integrated luminosity as a function of time for 2011.

CMSSW_4_2_8 and analyzed with CMSSW_4_2_8. The datasets used in this analysis are listed in Table 4.3.

All data must be certified before they can be used for analysis. This procedure makes sure that all subdetectors performed well for the recorded data and that only good quality data are used. The information about the quality of the events in a given run is provided by so called JSON files. After applying the JSON files to select qualified data, an integrated luminosity of 4.93 fb^{-1} is used for this analysis. The JSON files which cover different run ranges are also shown in Table 4.3.

Table 4.3: List of datasets and JSON files used in this analysis.

Datasets
/Photon/Run2011A-05Jul2011ReReco-ECAL-v1/AOD
/Photon/Run2011A-05Aug2011-v1/AOD
/Photon/Run2011A-03Oct2011-v1/AOD
/Photon/Run2011B-PromptReco-v1/AOD
JSON files
Cert_160404-163869_7TeV_May10ReReco_Collisions11_JSON_v3.txt
Cert_170249-172619_7TeV_ReReco5Aug_Collisions11_JSON_v3.txt
Cert_160404-180252_7TeV_PromptReco_Collisions11_JSON.txt

4.6 Event Selection

4.6.1 Primary Vertex Selection

Events must have at least one primary vertex to pass the candidate event selection. The requirements of a primary vertex are as follows:

- Not be a fake vertex: A fake primary vertex will be found when there are not enough quality tracks available to reconstruct a vertex, or if no sensible vertex is reconstructed.
- The number of degrees of freedom for the vertex fit χ^2 must be greater than 4.
- The z position of the vertex is required to satisfy $|z| < 24$ cm.
- The transverse position (x, y) of the vertex must satisfy $\sqrt{x^2 + y^2} <$ 2 cm.

4.6.2 Photon Selection

The photon candidates are collected using only triggers (A), as shown in Table 4.2, since all the requirements of these triggers satisfy our photon selection criteria. We require $E_T > 40$ GeV for the leading photon and $E_T > 25$ GeV for the trailing photon. Both photons must also satisfy the following requirements:

- passing (`CaloIdL` AND `IsoVL`) to reconfirm the trigger conditions
- supercluster $|\eta| < 1.4442$, which means only photons in the barrel region
- $\sigma_{i\eta i\eta} < 0.011$
- H/E < 0.05
- R9 < 1
- no pixel hit
- $I_{comb} < 6$ GeV, where ECAl and HCAL isolation variables are corrected for pileup. (See Section 4.8)

4.6.3 Optimization of Combined Isolation

In order to improve the sensitivity for a signal, we optimize the combined isolation requirement in the photon selection. The combined isolation < 6 GeV maximizes the signal efficiency over the square root of the background efficiency [58, 59]. The signal and background efficiencies are defined as the number of events passing all photon selection criteria over the number of events passing all photon selection criteria except combined isolation.

Signal events are taken from a general gauge-mediation Monte Carlo simulation sample. Photons in the signal events are required to originate only from neutralino decay. For the background events, two different samples are used. One is QCD Monte Carlo simulation events generated in flat p_T bins from 15 to 3000 GeV. The other background sample is from data using events with two photons and missing transverse energy < 30 GeV, which is expected to be dominated by QCD events. Both background samples yield an optimized value of $I_{comb} < 6$ GeV.

4.6.4 Electron Selection

Since we determine the photon selection efficiency by using a tag-and-probe method based on a $Z \to e^+e^-$ sample, the selection requirements for electrons and photons should be as similar as possible. We define a candidate signal electron with the same selection as for photons, except for requiring at least one pixel hit.

4.6.5 Fake Photon Selection

We also select a sample of photon-like candidates referred to as "fake photons". The purpose of defining fake photons is to estimate the characteristics of background events. This means that the definition of fake photons should not be too different from those of good photons. Fake photons mostly come from real photons close to jets in QCD events or for jets that are misidentified as photons. Thus, larger combined isolation values and a wider shower shape are expected for fake photons. Fake photons are collected by either triggers (A) OR (B) shown in Table 4.2, in order to increase the statistics of fake photon candidates. The requirements for fake photons are identical to those of real photon candidates except:

- passing [`CaloIdL` AND (`IsoVL` OR `R9Id`)] to reconfirm the trigger conditions. The requirement is different compared to good photons because of the triggers used to collect fake photon candidates.
- Combined isolation < 20 GeV.
- $(0.011 < \sigma_{i\eta i\eta} < 0.014)$ OR (6 GeV $<$ Combined isolation < 20 GeV).

Although we expect that there will be more hadronic activity (higher isolation sum) around fake photons, we do not want to select fake photon candidates using a high isolation sum, since that would will worsen the resolution of missing transverse energy. A balance between a reasonable upper isolation requirement and maintaining a reasonable number of fake photons is needed. The requirement $I_{comb} < 20$ GeV is determined from a comparison of the normalized E_T^{miss} distributions from the $\gamma\gamma$ and ff samples defined in Section 4.7 for the low-E_T^{miss} regions. A χ^2 variable is used to evaluate the changes in the E_T^{miss} shape when varying the upper limit of the combined isolation variable. The χ^2 variable is defined as:

$$\chi^2 = \frac{1}{N_{\text{bin}}} \sum_{i=1}^{N_{\text{bin}}} \frac{(ff_i - \gamma\gamma_i)^2}{\sigma_{ff_i}^2 + \sigma_{\gamma\gamma_i}^2}, \tag{4.4}$$

where $\gamma\gamma_i$ and ff_i are the normalized E_T^{miss} bin values, and $\sigma_{\gamma\gamma_i}$ and σ_{ff_i} are the statistical uncertainties in the bin values, for the $\gamma\gamma$ and ff samples, respectively.

Two different low-E_T^{miss} regions ($E_T^{miss} < 25$ GeV and $E_T^{miss} < 50$ GeV) are chosen to test the robustness of this method. It turns out that an upper

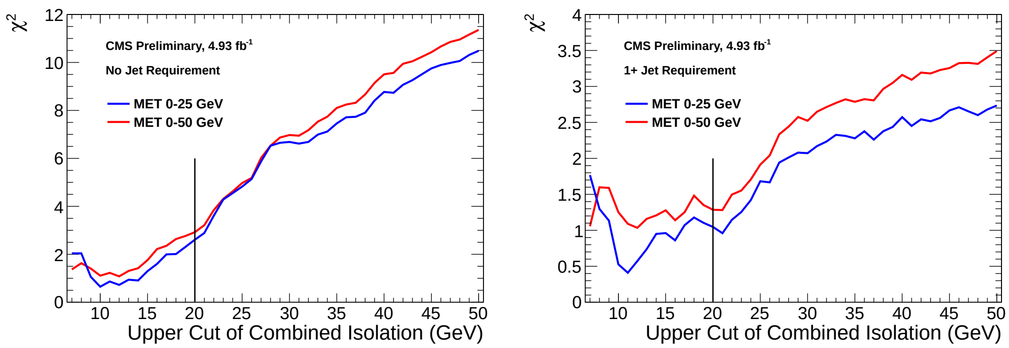

Figure 4.9: Distribution of the χ^2 variable from the E_T^{miss} distribution as a function of the upper limit on the combined isolation variable for the $\gamma\gamma$ and ff samples of events with no jet requirement (left) and for events with one or more jets (right). The 2 curves are for E_T^{miss} less than 25 GeV (blue) and 50 GeV (red).

limit of 20 GeV on the combined isolation variable is a reasonable selection requirement for defining fake photons, as shown in Figure 4.9.

4.6.6 Jet Selection

As described in Section 3.5, particle-flow jets with the anti-k_t clustering algorithm and the L1FastL2L3 jet energy correction are used in this analysis. Requirements to identify a jet are:

- Jet $p_T \geq 30$ GeV
- $|\eta| \leq 2.6$
- Neutral-hadron energy fraction < 0.99
- Neutral electromagnetic energy fraction < 0.99
- Number of the HCAL towers > 1

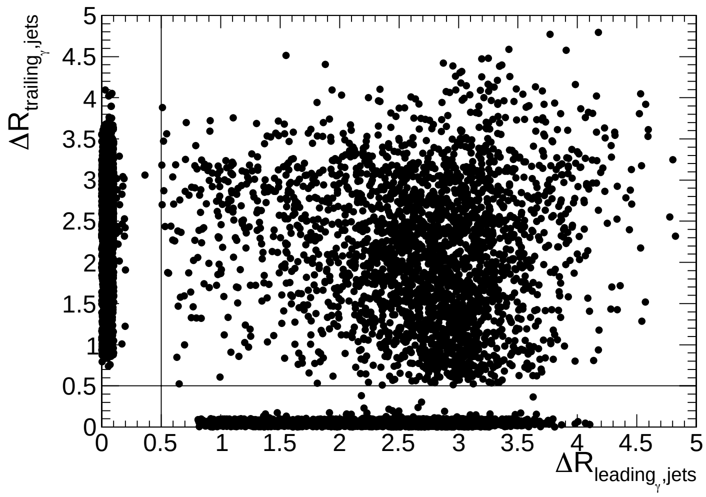

Figure 4.10: ΔR of the leading and trailing photons with respect to jets.

- For $|\eta| \leq 2.4$
  - Charged hadron energy fraction > 0
  - Charged electromagnetic energy fraction < 0.99
  - Charged multiplicity > 0

Jets are required to be separated from photons, electrons, fake photons, and muons in the event by a cone of $\Delta R > 0.5$. The choice of $\Delta R > 0.5$ is because of the anti-k_t clustering algorithm using a cone radius of jet $R = 0.5$, as illustrated in Figure 4.10, which shows the ΔR for the leading and trailing jets to the 2 photons. Points along the x or y axes are from jets candidates that overlap with photon candidates.

4.6.7 Muon Selection

Muons are used only for the jet cleaning, as discussed above. Muon candidates must pass the following identification criteria:

- GlobalMuonPromptTight, in which the track is identified as a global muon and the number of muon-detector hits used in the global fit is > 0
- $p_T \geq 20$ GeV
- $|\eta| \leq 2.1$
- number of valid tracker hits ≥ 11
- global normalized χ^2 fit < 10.0
- impact parameter ($|d_0|$) with respect to the beam spot < 2 mm
- (ECAL isolation + HCAL isolation + Track isolation)$/p_T < 0.1$
- energy of a muon deposited in the HCAL < 6 GeV
- energy of a muon deposited in the ECAL < 4 GeV

4.7 Events Classification

We classify events using the previously defined objects. First, all EM objects (photons, electrons, fake photons) in an event are sorted by p_T. If the leading p_T and the subleading p_T EM objects are separated by $\Delta R > 0.6$ and

- both EM objects are photons, the event is classified as a diphoton ($\gamma\gamma$) event

- both EM objects are fake photons, we classify the event as a fake-fake (ff) event
- both EM objects are electrons, the event is classified as an electron-electron (ee) event
- one EM object is an electron and another EM objects is a photon, the event is classified as an electron-photon ($e\gamma$) event

If the $\Delta R > 0.6$ requirement is not satisfied between the leading and sub-leading p_T EM objects, the event classification procedure will continue to perform the above criteria on the leading and third-leading p_T EM objects, then the leading and fourth-leading p_T EM objects, etc. until no more EM objects are left in the event. The $\Delta R > 0.6$ requirement is chosen because of the isolation sum cone size of $\Delta R = 0.3$ for each EM object. If there is no jet requirement in an event, we demand $\Delta\phi \geq 0.05$ between the two selected EM objects to minimize the contribution from beam-halo background. This requirement is especially relevant for the $\gamma\gamma$ sample. For consistency, the requirement is applied to all samples. A invariant-mass requirement of $81 \leq$ m(ee) ≤ 101 GeV is applied to the ee sample to select $Z \rightarrow e^+e^-$ events. Table 4.4 shows the number of events for each sample after applying the relevant selection criteria.

4.8 Pileup Correction

As the instantaneous luminosity of the LHC increased during 2011, the average number of interactions per bunch-crossing also increased. This effect, called pileup, results from multiple pp interactions per bunch-crossing caus-

Table 4.4: Numbers of selected $\gamma\gamma$, ff, $e\gamma$, and ee events without and with a jet requirement.

Type of event	without jet requirement	with a jet requirement
$\gamma\gamma$	96,717	30,347
ff	57,320	16,879
$e\gamma$	58,344	16,411
ee	599,603	108,080

ing several vertices in one event. Pileup affects our analysis directly by lowering the selection efficiency. When we calculate the isolation sum around an objects originating from the proton-proton hard scattering, the interactions due to soft scattering may also contribute to the same isolation region. These additional contributions need to be subtracted from the objects that we are interested in. In order to avoid a dependence on the pileup, we use a data-driven technique based on jet areas to correct for the pileup effect [60].

A measurement of the average energy per unit area of the jet due to pileup is determined by the "FastJet rho" (ρ_{PU}) variable event by event. An effective area of the jet is multiplied by ρ_{PU} to obtain the energy due to pileup. Since ρ_{PU} is derived using calorimeter information only, we apply the pileup energy correction only to the ECAL and HCAL isolation sums.

A tag-and-probe method with the $Z \to e^+e^-$ sample is used to obtain the effective areas. We use the $Z \to e^+e^-$ events because they are clean and well understood. The procedure for the ρ_{PU} correction is as follows [58]:

- one electron object in e^+e^- events must pass all electron criteria (tag)

- another electron object in e^+e^- events must pass all electron criteria

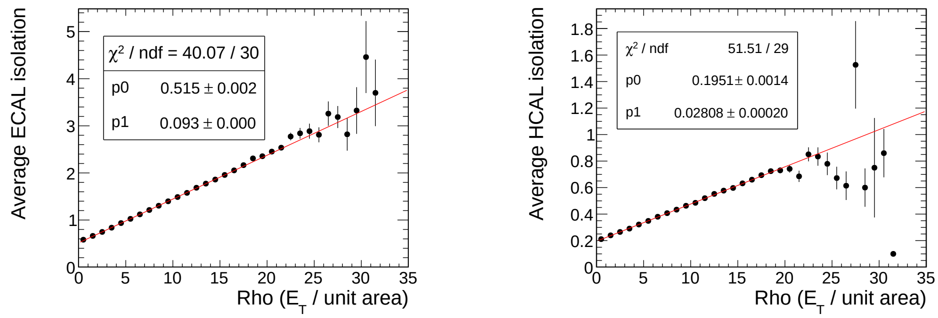

Figure 4.11: Average ECAL (left) and HCAL (right) isolations versus ρ_{PU}, along with the results of the linear fits.

except the combined isolation requirement (probe)

- the average ECAL and HCAL isolations of the probe are calculated for each bin of the corresponding ρ_{PU}
- only probes with < 40 GeV ECAL and HCAL isolation value are used, in order to avoid high isolation sums biasing the average ECAL and HCAL isolations of the probes
- the slope of a linear fit to the average isolation versus ρ_{PU} is defined as the effective area, as shown in Figure 4.11

The resulting fit values for the slopes are 0.093 and 0.028 for the ECAL and HCAL isolations, respectively. Finally, the pileup corrected isolations are given as

$$\text{ECAL Isolation}_{corrected} = \text{ECAL Isolation} - \rho_{PU} \times 0.093. \tag{4.5}$$

$$\text{HCAL Isolation}_{corrected} = \text{HCAL Isolation} - \rho_{PU} \times 0.028. \tag{4.6}$$

4.9 Electron Misidentification Rate

An electron can be misidentified as a photon if it passes through the silicon tracker without leaving enough hits to form a track or a matched pixel hit cannot be found for the corresponding supercluster. We extract the electron misidentification rate directly from the observed ee and $e\gamma$ events.

Define the electron misidentification rate to be $f_{e\to\gamma}$. The number N_{ee} of observed $Z \to e^+e^-$ events in the ee sample can be written as

$$N_{ee} = (1 - f_{e\to\gamma})(1 - f_{e\to\gamma})N_{trueZ} = (1 - f_{e\to\gamma})^2 N_{trueZ}, \tag{4.7}$$

where N_{trueZ} is the true number of $Z \to e^+e^-$ events.

Similarly, the number $N_{e\gamma}$ of observed $e\gamma$ events with one electron misidentified as a photon in the $Z \to e^+e^-$ sample will be

$$N_{e\gamma} = 2f_{e\to\gamma}(1 - f_{e\to\gamma})N_{trueZ}, \tag{4.8}$$

where the factor of 2 is because each electron can be misidentified.

The electron misidentification rate $f_{e\to\gamma}$ can then be obtained from equations (4.7) and (4.8) as

$$f_{e\to\gamma} = \frac{N_{e\gamma}}{2N_{ee} + N_{e\gamma}}. \tag{4.9}$$

N_{ee} and $N_{e\gamma}$ are determined from fits of the ee and $e\gamma$ invariant-mass spectra, respectively. The `RooFit` package [61] is used to perform the fit. The probability density function (PDF) for the signal shape is assumed to be a Crystal Ball function, which consists of a Gaussian function and a power-law low-end tail below a certain threshold. The Crystal Ball function can be written in the form:

$$f(x) = \begin{cases} \exp(-\frac{(x-\mu)^2}{2\sigma^2}) & \text{for } \frac{x-\mu}{\sigma} > -\alpha \\ (\frac{n}{|\alpha|})^n \exp(-\frac{|\alpha|^2}{2})(\frac{n}{|\alpha|} - |\alpha| - \frac{x-\mu}{\sigma})^{-n} & \text{for } \frac{x-\mu}{\sigma} < -\alpha \end{cases} \quad (4.10)$$

where x represents the invariant mass of the interested candidate, μ is the mean value of the gauss function, σ is the standard deviation of the gauss function, α is the threshold of the invariant mass which connects the gauss function and power-low, and n is the parameter controlling the power-low function.

The PDF used to model the background is given by an exponential function convolved with an error function. The exponential models the main background from the Drell-Yan process producing e^+e^- pairs, while the error function is used to handle the threshold effect of E_T requirements. The overall background PDF is given as:

$$g(x) = \exp[\beta(x - \delta)] \times \mathrm{Erf}[(\gamma - x)\kappa + \lambda] \quad (4.11)$$

where x represents the invariant mass of the interested candidate, β decides the slope of the exponential function, δ is the mean value of the exponential function, γ is the mean value of the error function, κ decides how sharp of the error function, and λ control the normalization of the error function.

The fit of the Z peak for the ee sample yields $N_{ee} = 473,154 \pm 2,584$ events, as shown on the left plot of Figure 4.12. Fitting the Z peak in the $e\gamma$ sample yields $N_{e\gamma} = 13,889 \pm 1,584$ events, as shown on the right plot of Figure 4.12.

We also study the electron misidentification rate as the function of the elec-

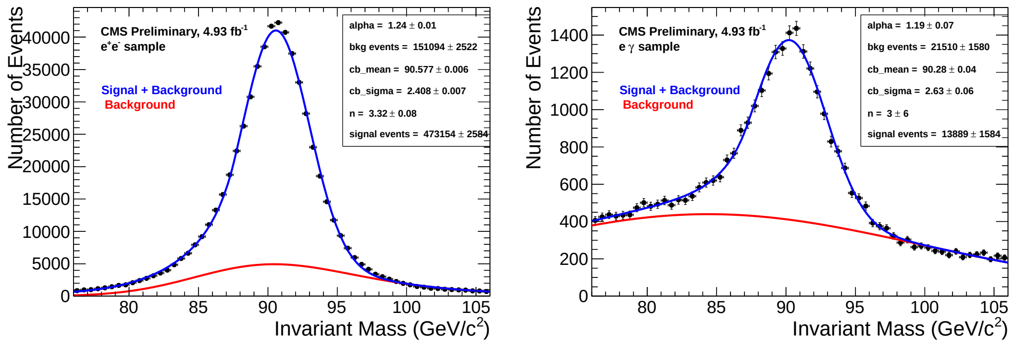

Figure 4.12: The fit of the Z peak in the ee (left) and $e\gamma$ samples (right). The blue curve shows the signal plus background fit and the red curve shows the background fit.

tron p_T using both data and Monte Carlo simulation samples. To obtain the p_T dependence of $f_{e\to\gamma}$ directly from data, we use different methods for the two p_T thresholds (40/25 GeV) in the event selection. For $p_T > 40$ GeV, we restrict the leading electron of the ee sample to different p_T ranges, while we require the photon to be the leading object in the $e\gamma$ sample in the corresponding p_T ranges. For $p_T < 40$ GeV, we apply the p_T requirement to the trailing electron in the ee sample, while requiring the photon to be the trailing object in the $e\gamma$ sample and obeying the corresponding p_T cut.

We then apply the same fit method described above to obtain N_{ee} and $N_{e\gamma}$ for different p_T ranges, as shown in Figures 4.13 and 4.14. Since we assume in the derivation that a specific electron (leading or trailing) is misidentified as the photon, the formula to obtain the electron misidentification rate becomes

$$f_{e\to\gamma} = \frac{N_{e\gamma}}{(N_{ee} + N_{e\gamma})}. \tag{4.12}$$

$Z \to e^+e^-$ Monte Carlo simulation samples are also used to study the electron

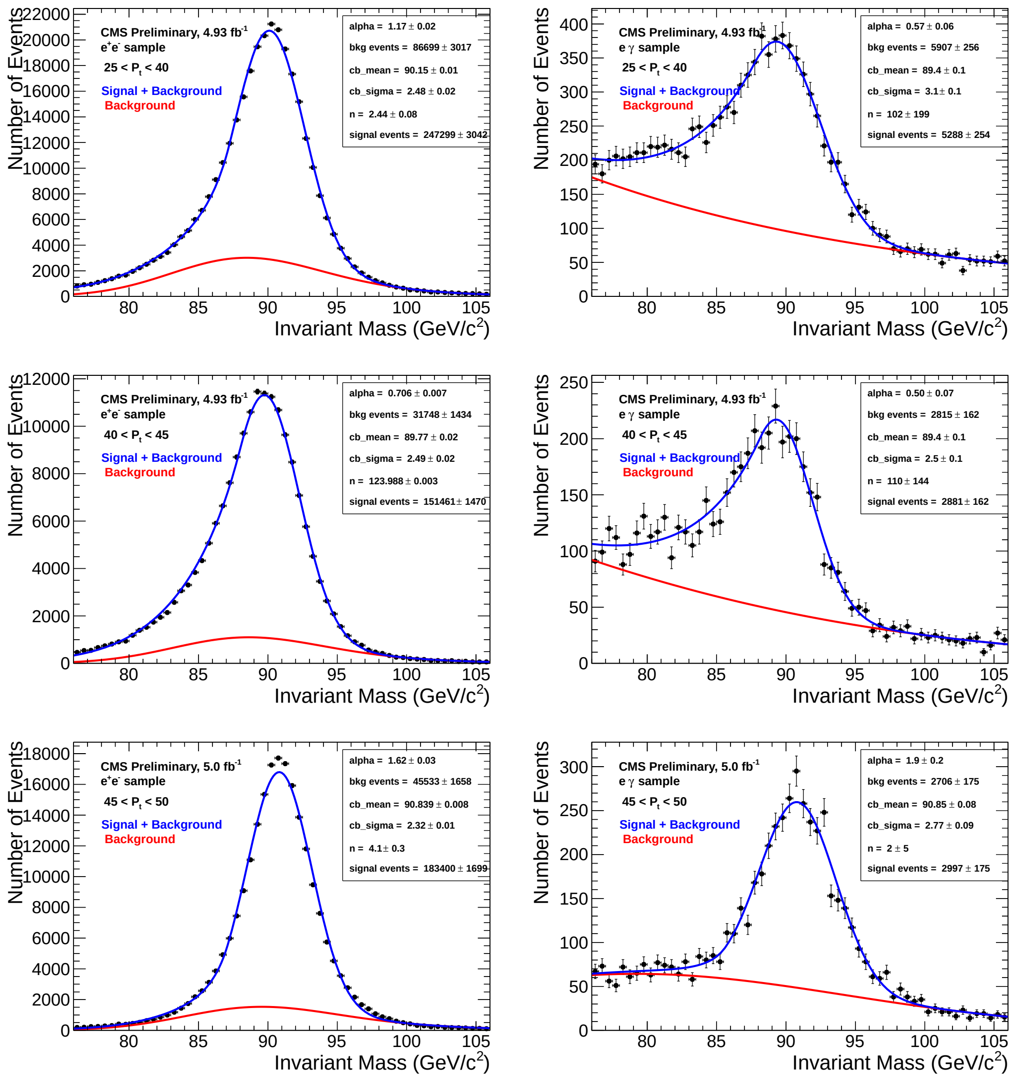

Figure 4.13: The fit of the Z peak in the ee sample (left) and $e\gamma$ sample (right) for the p_T ranges: $25 < p_T < 40$ GeV (top), $40 < p_T < 45$ GeV (middle), and $45 < p_T < 50$ GeV (bottom).

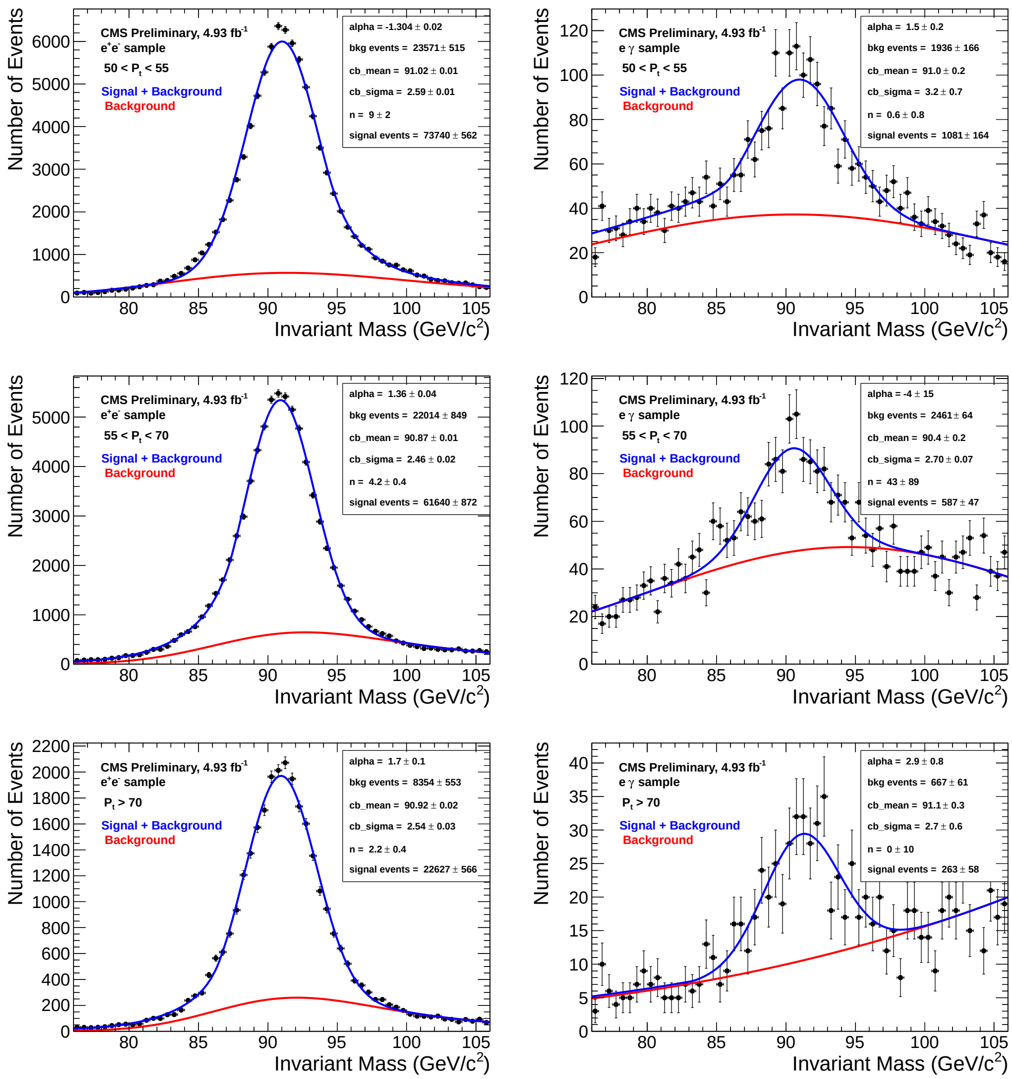

Figure 4.14: The fit of the Z peak in the ee sample (left) and $e\gamma$ sample (right) for the p_T ranges: $50 < p_T < 55$ GeV (top), $55 < p_T < 70$ GeV (middle), and $p_T > 70$ GeV (bottom).

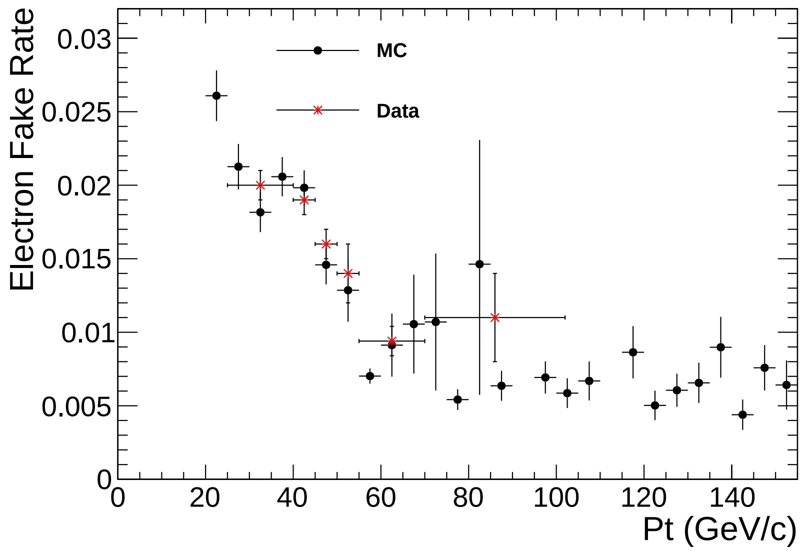

Figure 4.15: Electron misidentification rate as a function of p_T from data (red points) and Monte Carlo simulation (black points).

misidentification rate as a function of p_T. The electron misidentification rate is obtained by measuring how many reconstructed objects match with true electrons at the generation level and are reconstructed as photons. The results for $f_{e\to\gamma}$ from the data and Monte Carlo simulation samples are compared in Figure 4.15.

Finally, we take the maximum deviation of $f_{e\to\gamma}$ obtained from the p_T-dependent cases comparing to the one obtained from the inclusive case in data as the systematic error. We determine the average electron misidentification rate as:

$$f_{e\to\gamma} = 0.014 \pm 0.002\ (stat.) \pm 0.005\ (syst.) \tag{4.13}$$

4.10 Photon Identification Efficiency

In principle, we can obtain the photon selection efficiency from signal Monte Carlo simulation samples by applying the same photon identification requirements used in the data. However, a scale factor is needed to correct for potential differences between the photon identification efficiency in data, ϵ_{γ}^{data}, and the photon identification efficiency in Monte Carlo simulation, ϵ_{γ}^{MC}. It is straightforward to determine ϵ_{γ}^{MC}. However, because the sample of photons in data is not pure, it is difficult to directly measure ϵ_{γ}^{data}. Owing to the similar detector responses for electrons and photons, we use the following relation to obtain the photon efficiency scale factor:

$$\frac{\epsilon_{\gamma}^{data}}{\epsilon_{\gamma}^{MC}} = \frac{\epsilon_{e}^{data}}{\epsilon_{e}^{MC}}, \tag{4.14}$$

where ϵ_{e}^{data} and ϵ_{e}^{MC} are the electron identification efficiencies in data and Monte Carlo simulation, respectively. This is why the photon and electron selection requirements are kept similar in this analysis.

4.10.1 Tag-and-Probe Method

The electron identification efficiency ϵ_{e}^{data} is obtained by the tag-and-probe method, described as follows:

- The tag in an $e^{+}e^{-}$ event must pass all the electron selection criteria and match a silicon track within $\Delta R < 0.04$.
- The probe only needs to pass the p_T and $|\eta|$ cuts and match a silicon track within $\Delta R < 0.1$.

- Two types of tag-probe pairs are fitted on invariant-mass spectra simultaneously
  - all tag-probe pairs
  - pairs in which the probe passes additional photon identification criteria
- The PDF used to describe the signal is a Crystal Ball function, as given in Eq. (4.10).
- The PDF used to describe the background is an exponential function convolved with an error function, as given in Eq. (4.11).

Figure 4.16 shows ϵ_e^{data} for each photon identification selection as a function of the number of primary vertices in the event. The photon identification criteria applied to the probe are cumulative.

The photon efficiency scale factor is then measured to be [58, 59]

$$\frac{\epsilon_\gamma^{data}}{\epsilon_\gamma^{MC}} = \frac{\epsilon_e^{data}}{\epsilon_e^{MC}} = 0.994 \pm 0.002\ (stat.) \pm 0.035\ (syst.), \tag{4.15}$$

where the systematic error is determined by varying the fit parameters and evaluating the difference between ϵ_γ^{MC} and ϵ_e^{MC}.

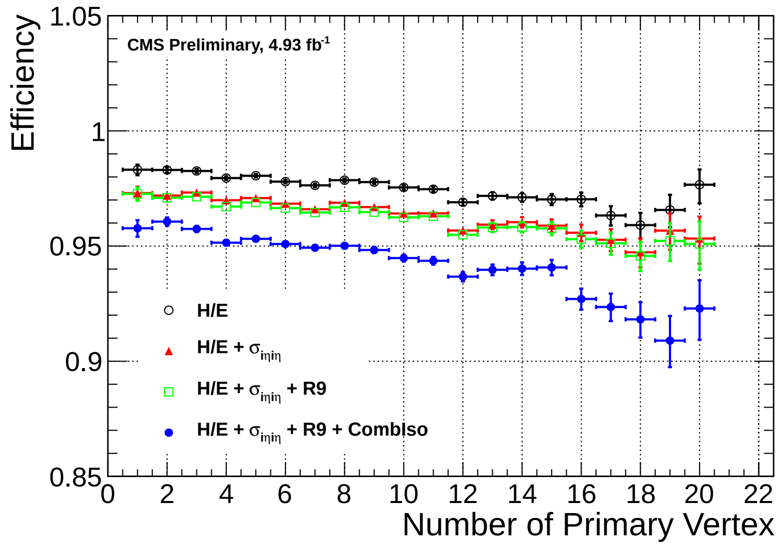

Figure 4.16: Electron identification efficiency versus the number of primary vertices by using a tag-and-probe method.

Chapter 5

Estimation of the Missing Transverse Energy Distributions of the Background and Results of Search for New Physics

Diphoton signal events with large E_T^{miss}, originating from new physics processes, may be contained in the selected $\gamma\gamma$ sample. We first need to estimate the contributions due to standard model physics processes contributing to our $\gamma\gamma$ sample. Then we can compared the predicted E_T^{miss} shape from the known SM physics processes with the E_T^{miss} shape of our observed $\gamma\gamma$ sample. An excess of events at large E_T^{miss} would indicate the existence of new physics. The two main SM backgrounds in the $\gamma\gamma$ sample are the QCD and

EWK backgrounds, as discussed in Section 4.1.

5.1 Electroweak Background Estimation

Events from $W\gamma$ with the W boson decaying into an electron and a neutrino while the electron being misidentified as a photon contribute to the $\gamma\gamma$ events. We can estimate this type of electroweak background by using the $e\gamma$ control sample. Again define the electron misidentification rate to be $f_{e\to\gamma}$. The observed number of $e\gamma$ events $N_{e\gamma}$ is:

$$N_{e\gamma} = (1 - f_{e\to\gamma})N_{trueW\gamma}, \tag{5.1}$$

where $N_{trueW\gamma}$ is the number of true $W\gamma$ events in the sample. The number $N_{\gamma\gamma}$ of $\gamma\gamma$ events due to the electroweak background is then given as:

$$N_{\gamma\gamma} = f_{e\to\gamma}N_{trueW\gamma} = \frac{f_{e\to\gamma}}{1 - f_{e\to\gamma}}N_{e\gamma}. \tag{5.2}$$

We use the measured electron misidentification rate $f_{e\to\gamma}$ given in Eq. (4.13) and multiply the missing transverse energy distribution of the $e\gamma$ sample by the factor $f_{e\to\gamma}/(1 - f_{e\to\gamma})$ to estimate the E_T^{miss} distribution of the electroweak background.

5.2 QCD Background Estimation

Two control samples (ee and ff) are used to estimate the QCD background. Since there is no true E_T^{miss} in QCD events, hadronic (jet) activity dominates the E_T^{miss} distribution of QCD events. Before comparing the E_T^{miss} shapes between our background control and diphoton candidate samples, we need to correct for potential differences between these samples with respect to hadronic activity.

We use the magnitude of the vector sum of the p_T (referred as di-EMPt) of the two jets associated with the selected pair of EM objects in each sample ($\gamma\gamma$, ff , and ee) as a measure of the hadronic activity. The jets are used instead of the EM objects themselves because the jet energy measurement is a better representation of the hadronic activity in an event. However, to better represent the EM objects, the jets definitions need to be modified compared to those in Section 4.6.6. The new requirements on the associated jets are:

- only pileup-corrected L1Fast particle-flow jets are used because the associated jets of interest here are essentially EM objects. The L2 and L3 jet energy corrections that are applied to real jets are not necessary here
- $p_T > 20$ GeV
- $|\eta| < 2.6$
- An EM object must be matched to a jet within $\Delta R < 0.3$
- If either one of the EM pair cannot be associated with a matched jet, the di-EMPt value is calculated using the four-vector of the EM objects.

Figure 5.1 shows a comparison of the normalized di-EMPt spectra from the $\gamma\gamma$, ee and ff samples for events with no jets, exactly 1 jet and at least 2 jets. Note that the spectra are normalized to the total number of events in each sample and not to the unit area in each histogram. The difference in the di-EMPt spectra between the $\gamma\gamma$ and ee samples is assumed to be due to different topologies. The $Z \rightarrow e^{+}e^{-1}$ events are produced via s-channel in pp collisions. However, the QCD diphoton events are produced via t- and u-channels. In addition, the fraction of events with 0, 1, ≥ 2 jets are different for the $\gamma\gamma$ and ee samples. Table 4.4 shows that 31% of the $\gamma\gamma$ events contain at least one jet, while for ee events it is only 18%.

A reweighting procedure is performed to compensate for the differences in the di-EMPt spectra between the candidate and control samples. First, the ratio of the candidate sample to the control samples is obtained from Figure 5.1. Then each event of the control samples is scaled using the di-EMPt ratio of the corresponding di-EMPt bin.

5.2.1 Estimate of the QCD Background Using the ff Sample

Figure 5.2 shows the di-EMPt ratio of the $\gamma\gamma$ sample to the ff sample before reweighting. Figure 5.3 compares the E_T^{miss} distributions of the ff sample before and after the di-EMPt reweighting. The shapes of the E_T^{miss} distributions do not change much after applying the di-EMPt reweighting because of the similar kinematics between the $\gamma\gamma$ and ff samples.

The final step to obtain the QCD background is to determine the proper normalization of the control sample to the diphoton candidate sample in the low-E_T^{miss} region. Events from new physics in our diphoton candidate sample are expected to have large E_T^{miss}. Hence, it is safe to normalize the control sample to a region dominated by background. We normalize the E_T^{miss} spectra

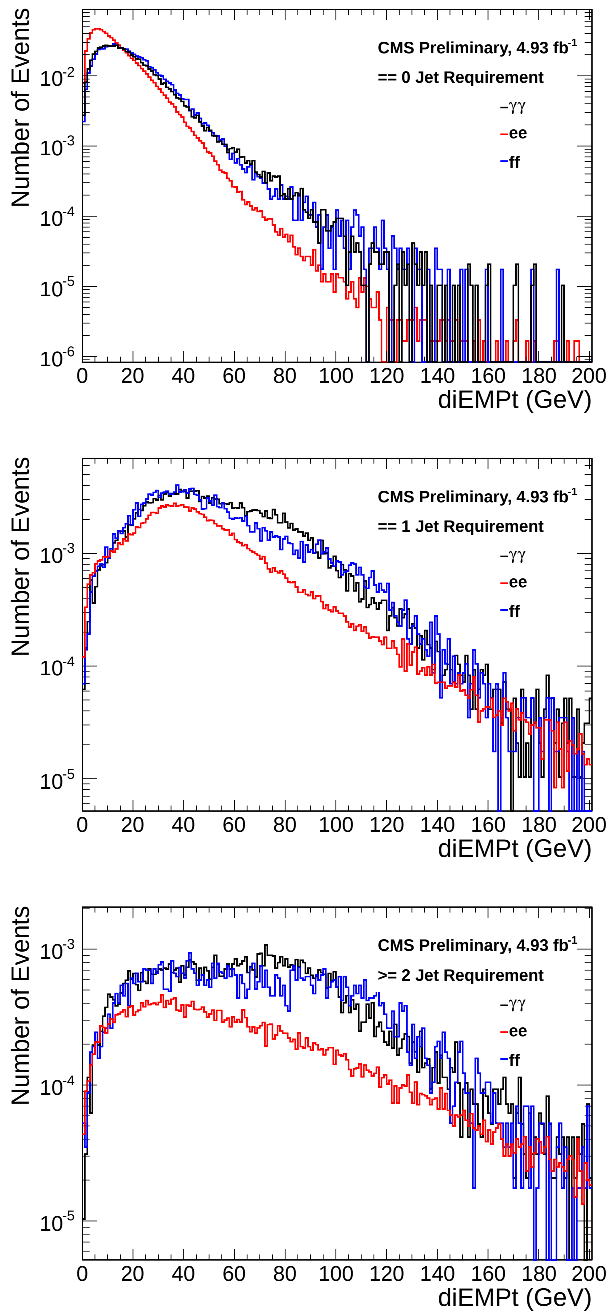

Figure 5.1: Comparison of the normalized di-EMPt distributions between candidate and control samples for events with no jets (top), exactly 1 jet (middle) and at least 2 jets (bottom).

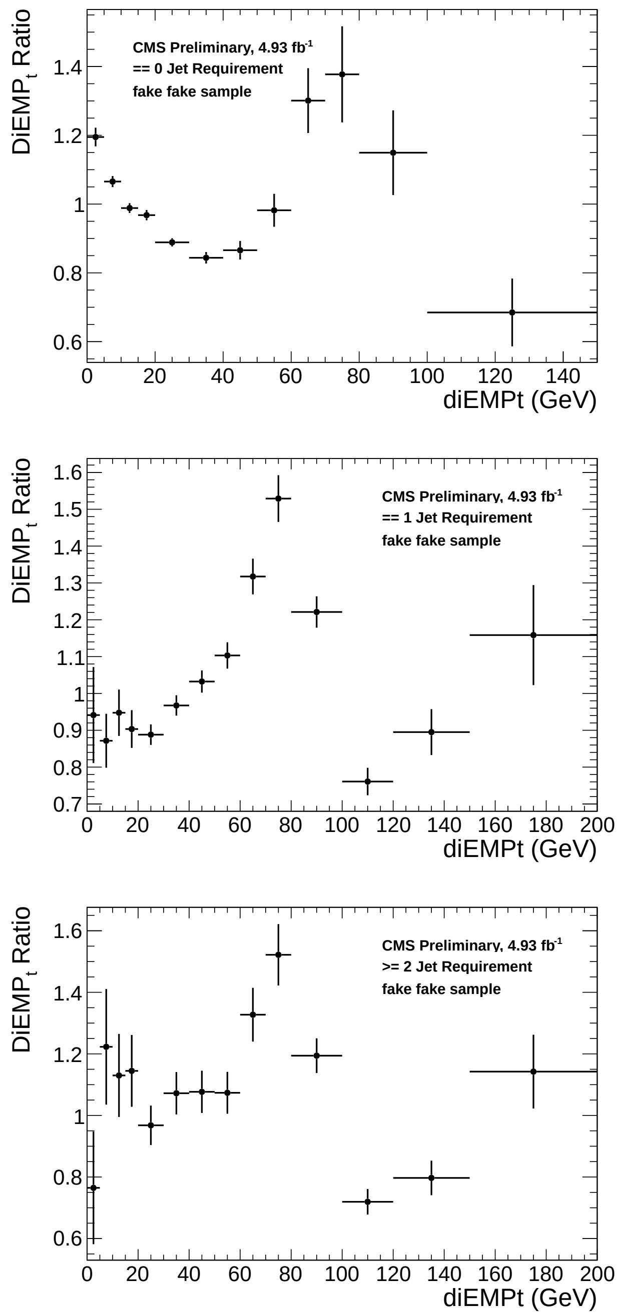

Figure 5.2: Di-EMPt ratio of the $\gamma\gamma$ sample to the ff sample as a function of di-EMPt for events with no jets (top), exactly 1 jet (middle) and at least 2 jets (bottom).

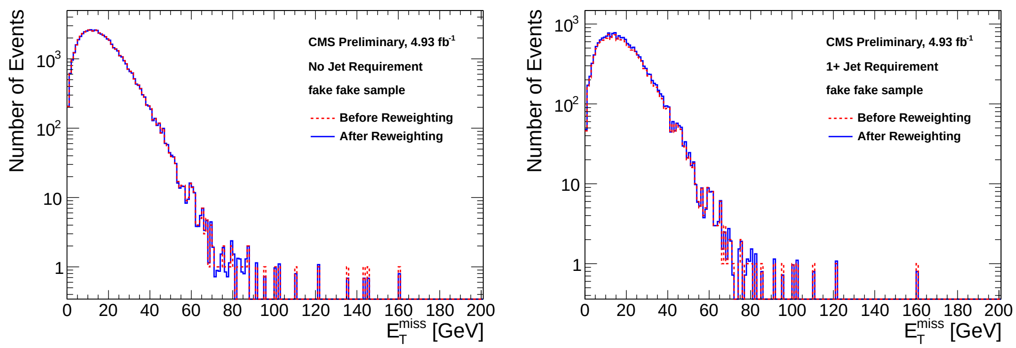

Figure 5.3: Comparison of the di-EMPt reweighting effect on the E_T^{miss} distributions in the ff sample with no jet requirement (left) and at least one jet requirement (right).

of our control sample by requiring:

$$N_{QCD} + N_{EWK} = N_{\gamma\gamma} \text{ for } \mathrm{E}_{\mathrm{T}}^{\mathrm{miss}} \leq 20 \text{ GeV}, \tag{5.3}$$

where N_{QCD} is the number of E_T^{miss} events in the QCD control sample, N_{EWK} is the number of E_T^{miss} events in the electroweak background obtained from the $e\gamma$ sample described in Section 5.1, and $N_{\gamma\gamma}$ is the number of E_T^{miss} events of the diphoton candidate sample. Figure 5.4 shows a 2D plot of the ratios of expected number of signal events to the observed number of $\gamma\gamma$ events in the range $E_T^{miss} \leq 20$ GeV as a function of the gluino and squark masses. The signal events are from a gluino-squark scan with a bino-like neutralino. The ratio is less than 0.0005 for most of the grid points. Hence, the signal contamination is negligible in the normalization region.

The normalization factors for the ff control sample are given in Table 5.1. Since the ff sample can be considered as the sideband of the $\gamma\gamma$ sample, according to its definition, and its kinematics is more similar to that of the

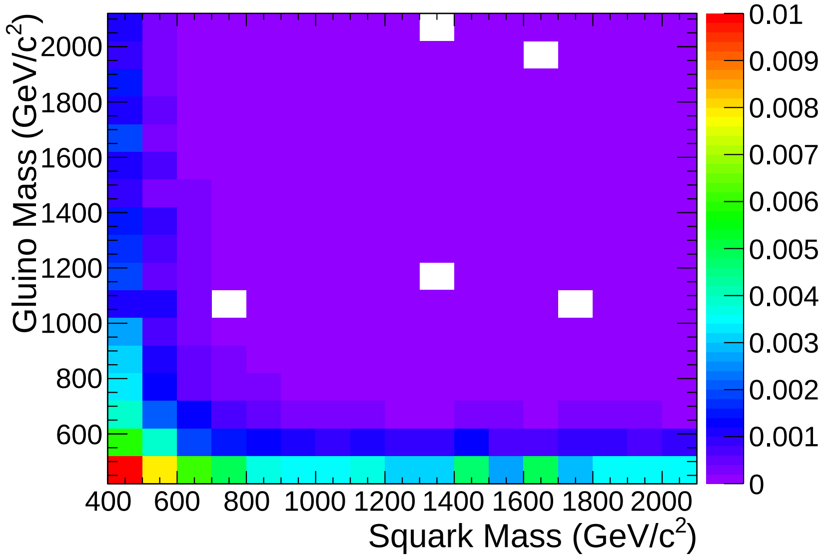

Figure 5.4: Ratios of the expected signal events over the observed $\gamma\gamma$ events in the $E_T^{miss} \leq 20$ GeV range as a function of the gluino and squark masses.

$\gamma\gamma$ sample compared to the ee sample, we take the ff sample as the main QCD background estimation of our analysis.

Table 5.1: Normalization factors of the control samples.

	Normalization factor	
Sample	Events with no jet requirement	Events with at least one jet
ff	1.703 ± 0.005	1.711 ± 0.004
ee	0.1660 ± 0.0005	0.1661 ± 0.0004

5.2.2 Estimate of the QCD Background Using the ee Sample

In a similar way, we can also estimate the QCD background using the ee sample. Figure 5.5 shows the di-EMPt ratio of the $\gamma\gamma$ sample to the ee sample. Figure 5.6 compares the E_T^{miss} distributions of the ee sample before and after applying the di-EMPt reweighting, which corrects the E_T^{miss} shape. The result of the di-EMPt reweighting for the no-jet requirement is shown on the left plot of Figure 5.6. For at least one jet, the di-EMPt reweighting does not modify the shape of the E_T^{miss} distribution much, but shifts the distribution owing to the different ratios (normalizations) of the jet components in the $\gamma\gamma$ and ee samples, as explained in Section 5.2.

Although we apply the requirement $81 \leq \mathrm{m}(ee) \leq 101$ GeV on the ee sample to select $Z \rightarrow e^+e^-$ events, there are contributions from other processes in the ee sample. These contributions from events such as $t\bar{t}$ and diboson production have real E_T^{miss} in the final state, and thus will bias the E_T^{miss} distribution of the ee sample. A sideband-subtraction method is performed to subtract the contributions from $t\bar{t}$ and WW production. Events in the ee sample with an invariant mass $\mathrm{m}(ee)$ between $71-81$ GeV and $101-111$ GeV are defined as sideband events. The same di-EMPt reweighting procedure is applied to sideband events. Then, the E_T^{miss} distributions of the sideband events is subtracted from the E_T^{miss} distributions of the ee sample. Figure 5.7 shows the di-EMPt ratio of the $\gamma\gamma$ sample to the ee sideband sample. Figure 5.8 illustrates the effect of the sideband subtraction.

The sideband-subtraction method is assumed to remove all backgrounds whose $m(ee)$ distribution is flat in both the signal and sideband regions.

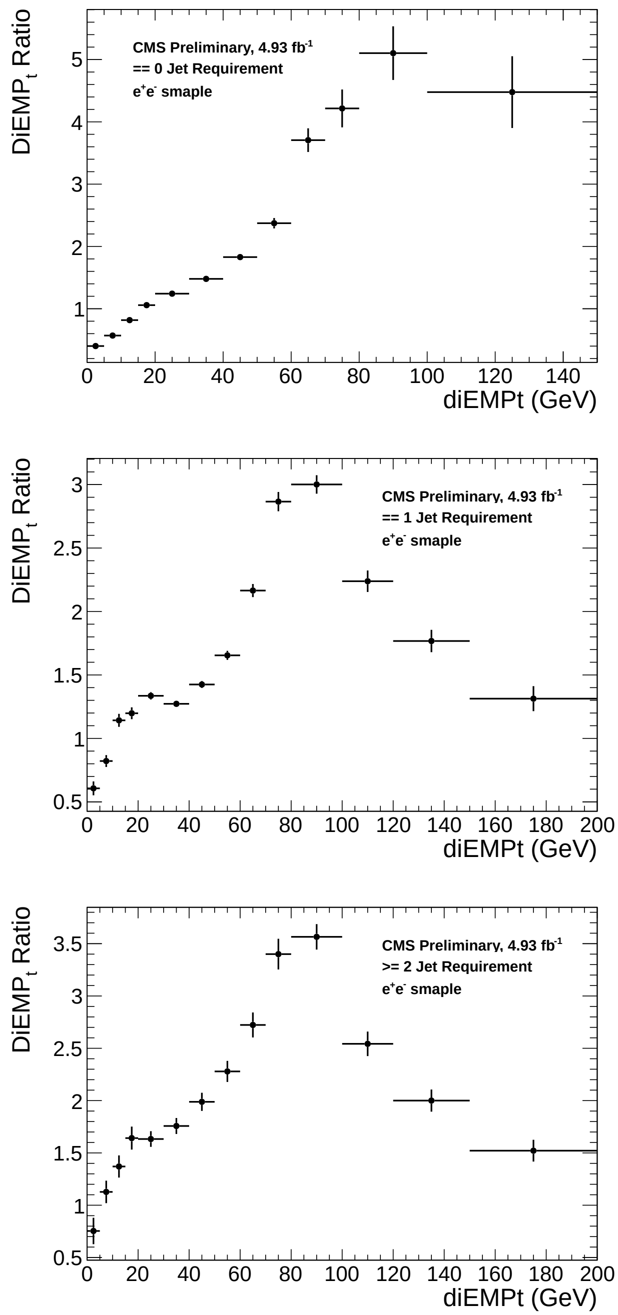

Figure 5.5: Di-EMPt ratio of the $\gamma\gamma$ sample to the ee sample as a function of di-EMPt for events with no jets (top), exactly 1 jet (middle) and at least 2 jets (bottom).

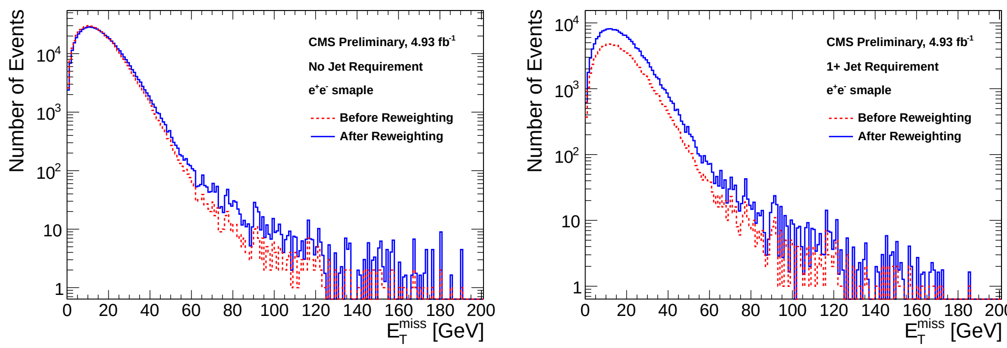

Figure 5.6: Comparison of effect of the di-EMPt reweighting on the E_T^{miss} distributions in the ee sample without jet requirement (left) and at least one jet (right).

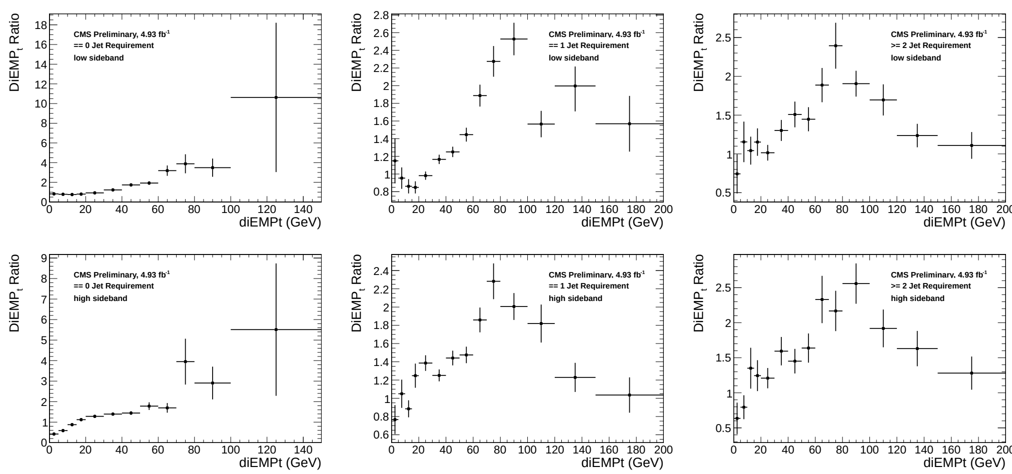

Figure 5.7: Di-EMPt ratio of the $\gamma\gamma$ sample to the ee sideband sample with invariant mass 71-81 GeV (top row) and 101-111 GeV (bottom row) for events with no jets (left), exactly 1 jet (middle) and at least 2 jets (right).

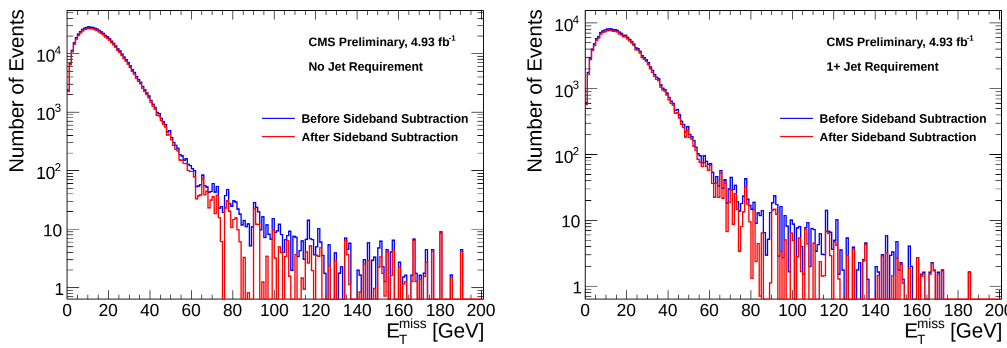

Figure 5.8: Comparison of the sideband subtraction on the E_T^{miss} distributions in the ee sample with the no jet requirement (left) and at least one jet in the event (right).

However, the $ZZ \to e^+e^-\nu\nu$ and $WZ \to l\nu e^+e^-$ backgrounds produce distributions that peak around the Z mass and contribute true E_T^{miss} to the ee sample. Monte Carlo simulation samples shown in Table 5.2 are used to subtract these additional diboson contributions from the ee sample. The diboson Monte Carlo simulation samples are normalized to 4.93 fb^{-1} of total integrated luminosity, based on the next-to-leading-order cross section. The di-EMPt reweighting procedure is also applied to the diboson samples using the $\gamma\gamma$-to-ee di-EMPt ratios obtained directly from data, as shown in Figure 5.5. In order not to double subtract the ZZ and WZ contributions in the signal region, scale factors of 0.95 and 0.9 are applied to the Monte Carlo simulation sample, respectively. The scale factors are determined from the Monte Carlo simulation samples by calculating the fraction of events with 81 $\leq$ m(ee) $\leq$ 101 GeV.

Figure 5.9 shows the E_T^{miss} distributions from the sideband subtraction technique, including the WZ, and ZZ components. The diboson subtraction has little effect on the low E_T^{miss} side, but it can remove up to 40% of the high-

Table 5.2: Monte Carlo simulation samples and NLO cross sections used for the diboson subtraction in the ee sample.

Sample	NLO cross section (pb)
`ZZTo2L2Nu-TuneZ2-7TeV-pythia6-tauola`	0.26
`WZTo3LNu-TuneZ2-7TeV-pythia6-tauola`	0.55

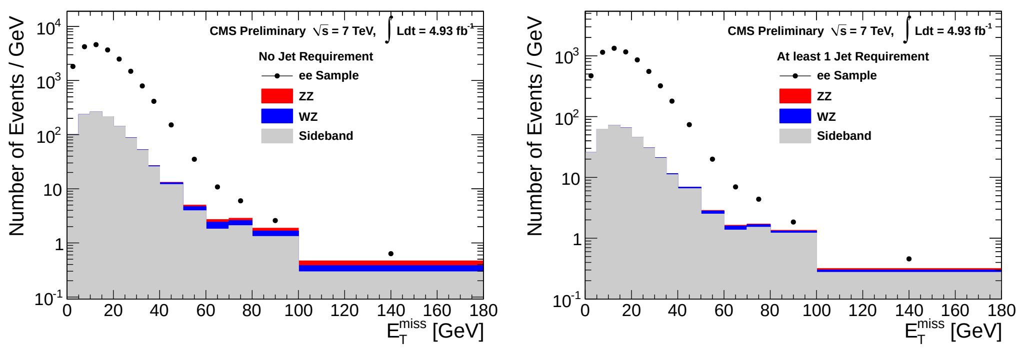

Figure 5.9: Contributions in the ee E_T^{miss} distribution for events with no jets (left) and at least one jet (right). Black points are total ee sample including contributions from diboson ZZ events (red areas), diboson WZ events (blue areas), and sideband-subtraction events (gray areas).

E_T^{miss} events for the case of no-jet requirement and up to 20% for events with at least one jet.

After subtracting all the non-$Z \rightarrow e^+e^-$ events from the ee sample, we normalize the ee sample to the $\gamma\gamma$ sample using Eq. (5.3). The normalization factors for the ee control sample are given in Table 5.1.

Finally, we also use the Monte Carlo simulation samples to validate the QCD background estimation method using the ee sample. Details of the test are shown in Appendix C.

5.3 Systematic Uncertainties in the Background Estimation

To estimate the systematic uncertainty from the di-EMPt reweighting procedure, we generate new di-EMPt ratios using a Gaussian function whose mean value is equal to its original ratio and width is equal to the statistical uncertainty on the ratio. This is done for each bin of di-EMPt ratios. We repeat this procedure one thousand times. Each time, the new di-EMPt ratio is used to perform a di-EMPt reweighting, producing a new E_T^{miss} distribution. The systematic uncertainties are determined from the root mean square of the 1000 E_T^{miss} distributions in each E_T^{miss} bin. The systematic uncertainties of the di-EMPt reweighting procedure are $1 \sim 3\%$ for different E_T^{miss} bins.

Another source of systematic uncertainty is the normalization procedure. The uncertainty in the electron misidentification rate leads to an uncertainty in the electroweak background estimation, which affects the normalization scale factor. The normalization uncertainty is obtained by using error propagation in Eq. (5.3). The normalization uncertainties are $0.2 \sim 0.3\%$ for different E_T^{miss} bins.

5.4 Comparisons of the Diphoton Yields and the Total Background Prediction

After determining the electroweak and QCD background estimations, we combine them to estimate the total background in the $\gamma\gamma$ E_T^{miss} distribution. Tables 5.3 and 5.4 summarize the number of observed $\gamma\gamma$ events and

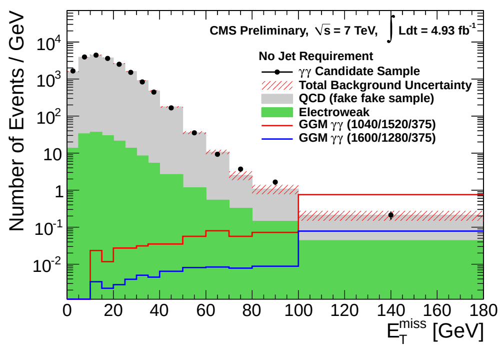

Figure 5.10: E_T^{miss} distribution of diphoton events with the predicted QCD backgrounds using the ff sample for events with no jet requirement (left) and at least one jet (right). Black points are diphoton events. Red hatched areas are the total background uncertainty including systematic and statistical uncertainties. Gray areas are estimation of the QCD background and green areas are estimation of the EWK background. Two GGM points with squark/gluino/neutralino masses in GeV are also shown.

the background predictions, with their statistical and systematic uncertainties. Figure 5.10 shows the E_T^{miss} spectrum of the $\gamma\gamma$ events with the predicted backgrounds using the ff sample for the QCD background estimation. Figure 5.11 gives the corresponding E_T^{miss} spectrum with the predicted backgrounds using the ee sample for the QCD background estimation. Two signal points with squark/gluino/neutralino masses given in GeV are also included in Figures 5.10 and 5.11.

Since the kinematics of the ff sample is more similar to the $\gamma\gamma$ sample than the ee sample, we take the ff sample as the default QCD background estimate, and use the difference between the ff and ee estimates as the systematic uncertainty. We add the systematic uncertainty in electroweak and QCD backgrounds in quadrature to obtain the systematic uncertainty in the total background. The statistical uncertainty in the total background

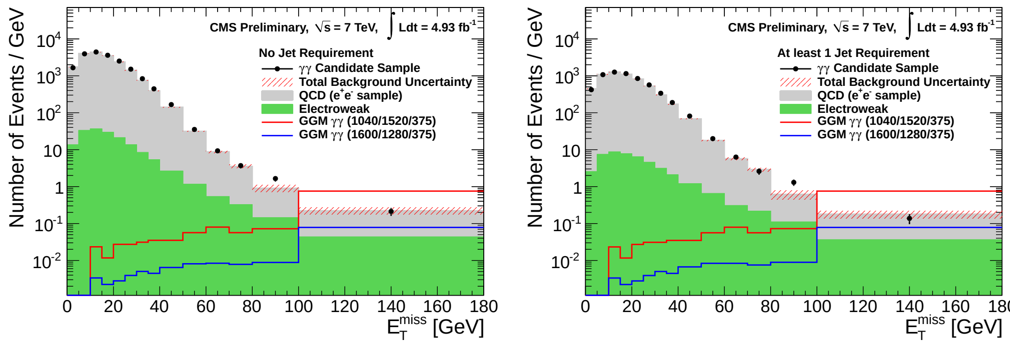

Figure 5.11: E_T^{miss} distribution of diphoton events with the predicted QCD backgrounds using the ee sample for events with no jet requirement (left) and at least one jet (right). Black points are diphoton events. Red hatched areas are the total background uncertainty including systematic and statistical uncertainties. Gray areas are estimation of the QCD background and green areas are estimation of the EWK background. Two GGM points with squark/gluino/neutralino masses in GeV are also shown.

is determined by adding the statistical uncertainty in electroweak and QCD backgrounds in quadrature. The final E_T^{miss} distributions are shown in Figure 5.12.

Table 5.3: Numbers of observed events and the estimated backgrounds for events with no jets requirement for different region of E_T^{miss}. The uncertainties are statistical and systematic, respectively.

E_T^{miss} bins (GeV)	0-20	20-50	50-60	60-70	70-80	80-100	>100
Observed Events	68033	28151	353	93	37	33	17
EW Background	$562.7 \pm 2.9 \pm 191.3$	$269.2 \pm 2.0 \pm 91.5$	$11.6 \pm 0.4 \pm 3.9$	$5.4 \pm 0.3 \pm 1.8$	$3.3 \pm 0.2 \pm 1.1$	$2.9 \pm 0.2 \pm 1.0$	$3.5 \pm 0.2 \pm 1.2$
QCD Background (ee)	$67470.3 \pm 112.0 \pm 109.1$	$25738.7 \pm 69.5 \pm 44.5$	$302.0 \pm 8.1 \pm 1.1$	$81.9 \pm 4.6 \pm 0.5$	$32.0 \pm 3.7 \pm 0.3$	$15.2 \pm 3.6 \pm 0.3$	$14.3 \pm 3.5 \pm 0.5$
QCD Background (ff)	$67470.3 \pm 339.0 \pm 110.3$	$29509.6 \pm 224.2 \pm 50.5$	$345.5 \pm 24.3 \pm 1.4$	$101.8 \pm 13.2 \pm 1.0$	$22.0 \pm 6.1 \pm 0.4$	$18.6 \pm 5.6 \pm 0.5$	$13.5 \pm 4.8 \pm 0.4$
Total Background (ff)	$68033 \pm 339.0 \pm 191.3$	$29778.8 \pm 224.2 \pm 3772.0$	$357.1 \pm 24.3 \pm 43.7$	$107.2 \pm 13.2 \pm 20.0$	$25.2 \pm 6.1 \pm 10.1$	$21.5 \pm 5.6 \pm 3.5$	$17.0 \pm 4.8 \pm 1.4$

Table 5.4: Number of observed events and the estimated backgrounds for events with at least one jet for different region of E_T^{miss}. The uncertainties are statistical and systematic, respectively.

E_T^{miss} bins (GeV)	0-20	20-50	50-60	60-70	70-80	80-100	>100
Observed Events	19515	10507	199	63	26	26	11
EW Background	$132.1 \pm 1.4 \pm 44.9$	$92.5 \pm 1.2 \pm 31.5$	$6.5 \pm 0.3 \pm 2.2$	$3.1 \pm 0.2 \pm 1.0$	$2.2 \pm 0.2 \pm 0.7$	$2.2 \pm 0.2 \pm 0.8$	$2.9 \pm 0.2 \pm 1.0$
QCD Background (ee)	$19382.9 \pm 59.9 \pm 25.9$	$9677.5 \pm 42.5 \pm 13.2$	$171.3 \pm 6.1 \pm 0.6$	$53.7 \pm 3.7 \pm 0.3$	$26.9 \pm 3.1 \pm 0.2$	$10.2 \pm 3.2 \pm 0.2$	$11.5 \pm 3.1 \pm 0.1$
QCD Background (ff)	$19382.9 \pm 182.1 \pm 27.5$	$10957.9 \pm 136.9 \pm 16.8$	$183.8 \pm 17.7 \pm 1.2$	$67.3 \pm 10.7 \pm 1.1$	$15.4 \pm 5.1 \pm 0.5$	$9.4 \pm 4.0 \pm 0.3$	$10.1 \pm 4.2 \pm 0.3$
Total Background (ff)	$19515 \pm 182.1 \pm 44.9$	$11050.5 \pm 136.9 \pm 1280.4$	$190.3 \pm 17.7 \pm 12.7$	$70.4 \pm 10.7 \pm 13.6$	$17.6 \pm 5.1 \pm 11.5$	$11.6 \pm 4.0 \pm 1.0$	$13.0 \pm 4.2 \pm 1.7$

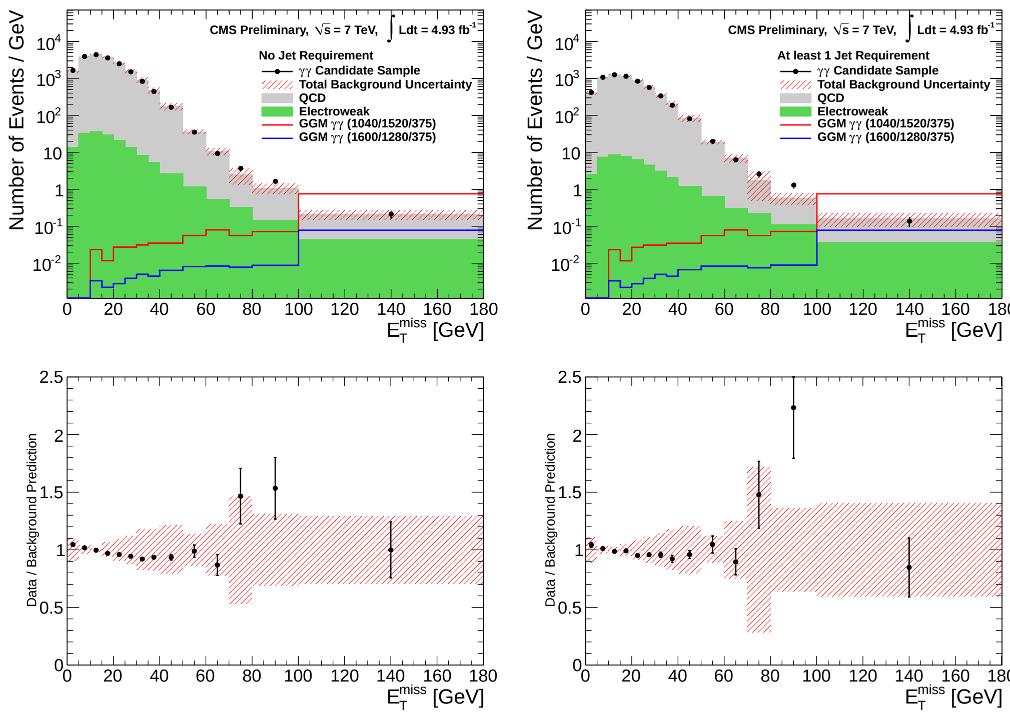

Figure 5.12: E_T^{miss} distribution of diphoton events with predicted backgrounds for the no jet requirement (left) and events with at least one jet (right). Black points are diphoton events. Red hatched areas are the total background uncertainty including systematic and statistical uncertainties. Gray areas are estimation of the QCD background and green areas are estimation of the EWK background. Two GGM points with squark/gluino/neutralino masses in GeV are also shown. Bottom plots show the ratios of the data to the background prediction (points), while the hatched area represents the ratios of the total background uncertainty to the total background prediction for each E_T^{miss} bin.

5.5 Cross-Check of the Background Estimate

As a cross-check of our method to estimate the background, we compare the distributions of other variables in our diphoton events to the background estimates. The di-EMPt reweighting procedure is performed on these distributions and the normalization factors shown in Table 5.1 are used. We study several kinematic variables, including:

- the number of jets in the event,
- HT: the scalar sum of the p_T of the selected jets in an events,
- MHT: the magnitude of the vector sum of the p_T of selected jets in an event,
- the p_T of the leading jet,
- the number of primary vertices in the event.

Figures 5.13 through 5.17 show the various distributions of our $\gamma\gamma$ data sample, compared to the total background estimates. Again, the ff sample is used for the QCD background estimate, and the difference between the ff and ee estimates is taken as the systematic uncertainty.

The results of the cross-check show that the kinematic distributions of diphoton events agree with the background estimate within the ranges of the uncertainties. Therefore, we are confident with the method of the background estimate.

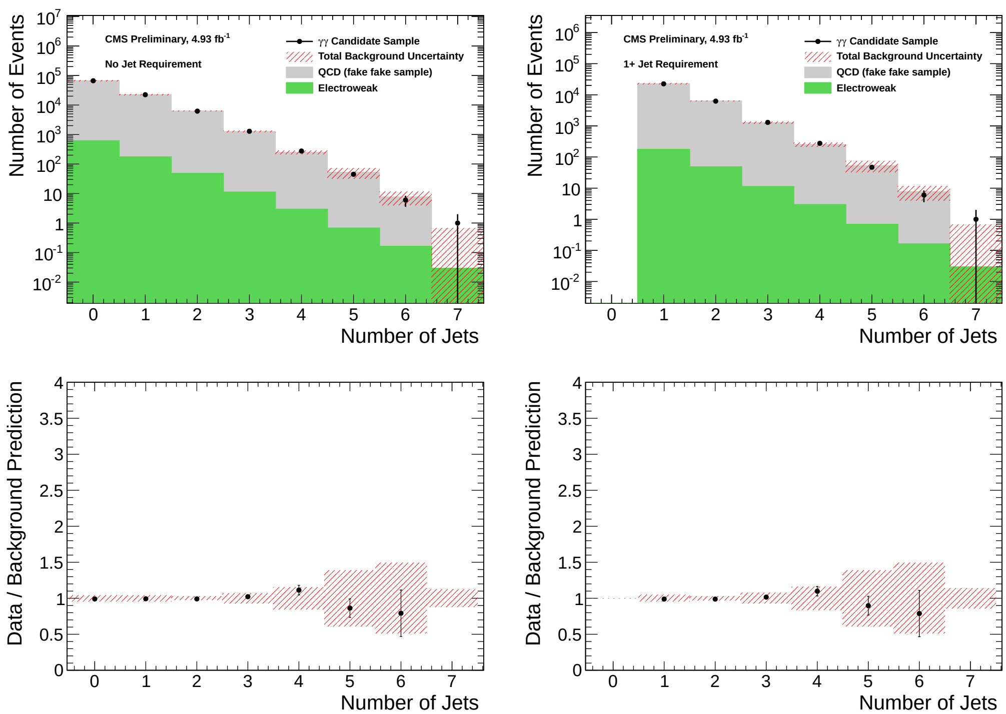

Figure 5.13: Comparisons of the $\gamma\gamma$ data to total background predictions for the number of jets with the no jet requirement (left) and for events with at least one jet (right).

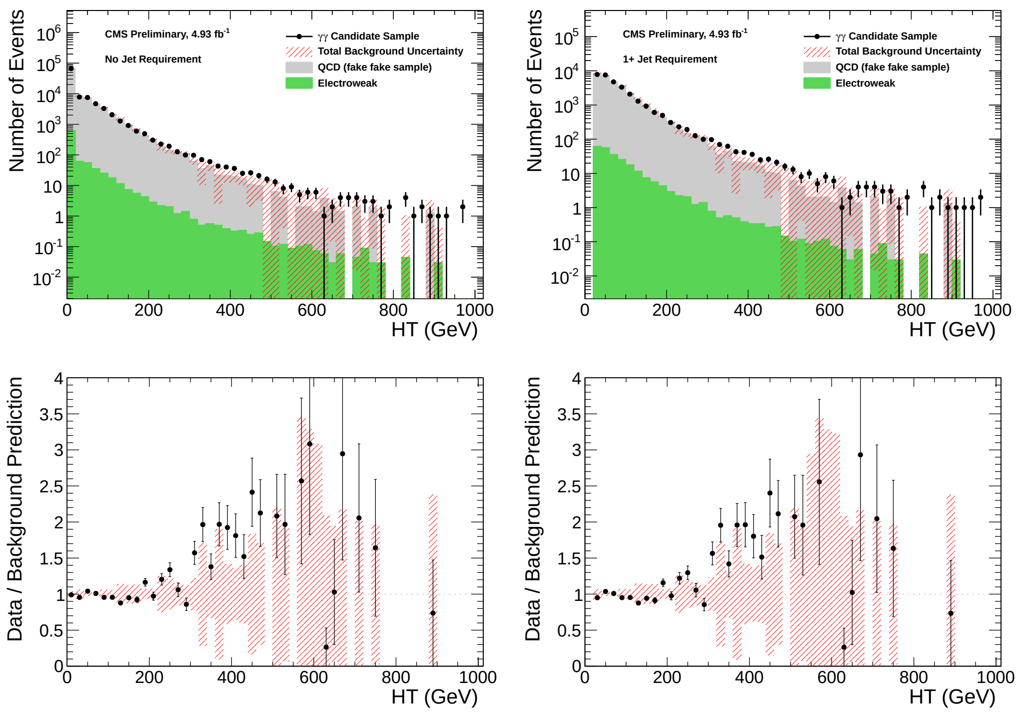

Figure 5.14: Comparisons of the $\gamma\gamma$ data to total background predictions versus HT with the no jet requirement (left) and for events with at least one jet (right).

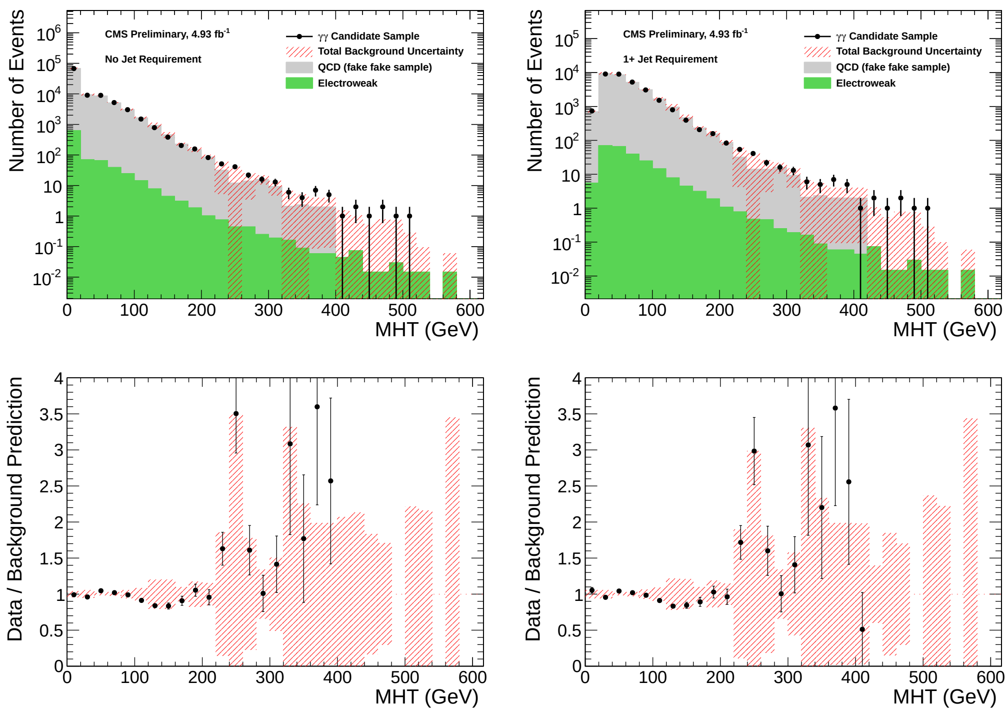

Figure 5.15: Comparisons of the $\gamma\gamma$ data to total background predictions versus MHT with the no jet requirement (left) and for events with at least one jet (right).

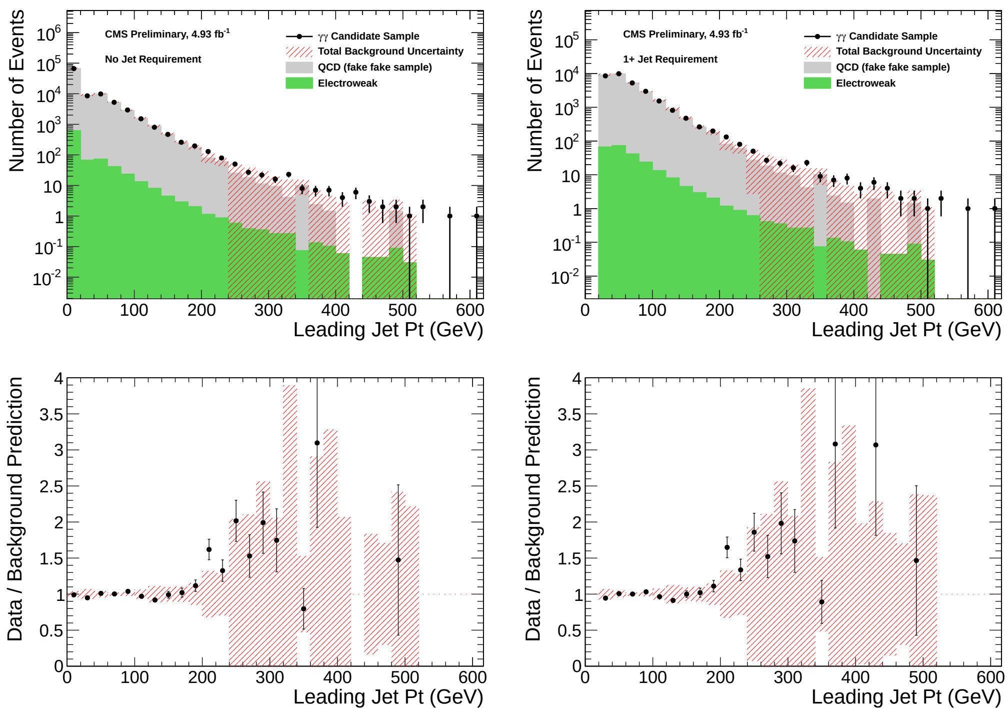

Figure 5.16: Comparisons of the $\gamma\gamma$ data to total background predictions for the leading jet p_T with the no jet requirement (left) and for events with at least one jet (right).

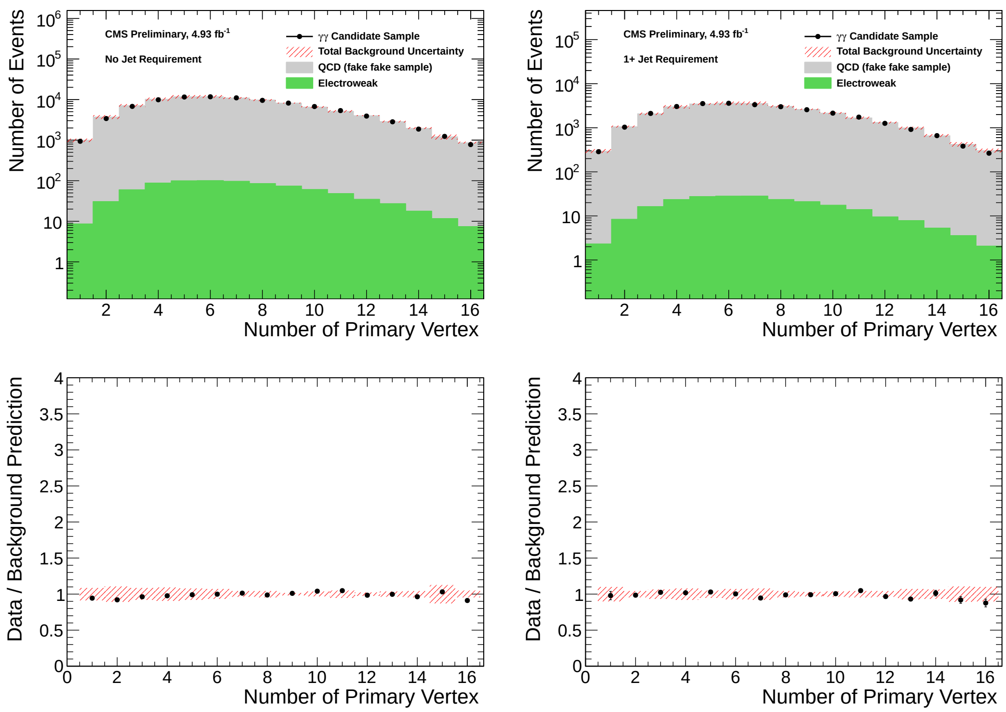

Figure 5.17: Comparisons of the $\gamma\gamma$ data to total background predictions for number of primary vertices with the no jet requirement (left) and for events with at least one jet (right).

Chapter 6

Interpretation of Results

Since we observe no excess when comparing the observed number of $\gamma\gamma$ events to the SM background predictions, we proceed to set upper limits on the signal production cross section of new physics processes. We interpret our results based on the GGM signal scans described in Section 4.3, as well as the SMS model. A modified frequentist method (CL_s method) [62] is used as the statistical tool.

6.1 Statistical Method

In order to compare the compatibility of the observed data with a potential new physics signal, we use a profile likelihood method [63] with the following procedure:

- Construct the likelihood function

$$\mathcal{L}(data|\mu,\theta) = Poisson(data|\mu \cdot s(\theta) + b(\theta)) \cdot p(\tilde{\theta}|\theta), \tag{6.1}$$

where "data" is either the observed data or simulated pseudo-data; μ is the signal-strength modifier; θ represents a set of nuisance parameters; $s(\theta)$ is the signal expectation; $b(\theta)$ is the background expectation; $p(\tilde{\theta}|\theta)$ is the PDF of the systematic uncertainty, where $\tilde{\theta}$ is the default value of the nuisance parameter; $Poisson(data|\mu \cdot s(\theta) + b(\theta))$ is the product of the Poisson PDF to observe n_i events in bin i:

$$\prod_i \frac{(\mu s_i + b_i)^{n_i}}{n_i!} e^{-\mu s_i - b_i}. \tag{6.2}$$

- Define a test statistic $\tilde{q}_\mu$ based on the profile likelihood ratio for the compatibility of the data with the background-only and signal+background hypotheses. In the latter case, the signal is allowed to be scaled by μ.

$$\tilde{q}_\mu = -2ln\frac{\mathcal{L}(data|\mu,\hat{\theta}_\mu)}{\mathcal{L}(data|\hat{\mu},\hat{\theta})}, \text{ with constraint } 0 \leq \hat{\mu} \leq \mu, \tag{6.3}$$

where $\hat{\theta}_\mu$ is the value of θ that maximizes $\mathcal{L}$ for a specified μ. The estimators $\hat{\mu}$ and $\hat{\theta}$ correspond to the values of μ and θ at the global maximum of the likelihood. Demanding a nonnegative signal puts a constraint of $\hat{\mu} \geq 0$. The upper constraint $\hat{\mu} \leq \mu$ is imposed by hand to ensure that any upward fluctuations of the data giving $\hat{\mu} > \mu$ are not considered as evidence against the signal hypothesis.

- Determine the observed value of the test statistic $\tilde{q}_\mu^{obs}$ for a given μ. We also find the nuisance parameters $\tilde{\theta}_0^{obs}$ and $\tilde{\theta}_\mu^{obs}$ that maximize the likelihood $\mathcal{L}$, given the observed data, for the background-only and signal+background hypotheses, respectively.
- Construct the PDFs for $f(\tilde{q}_\mu|\mu, \tilde{\theta}_\mu^{obs})$ and $f(\tilde{q}_\mu|0, \tilde{\theta}_0^{obs})$ by generating toy Monte Carlo pseudo-data.
- Calculate CL_{sb}, CL_b and CL_s:

$$CL_{sb} \equiv P(\tilde{q}_\mu \geq \tilde{q}_\mu^{obs}|signal + background) = \int_{\tilde{q}_\mu^{obs}}^{\infty} f(\tilde{q}_\mu|\mu, \tilde{\theta}_\mu^{obs}) d\tilde{q}_\mu, \quad (6.4)$$

$$CL_b \equiv P(\tilde{q}_\mu \geq \tilde{q}_\mu^{obs}|background\ only) = \int_{\tilde{q}_0^{obs}}^{\infty} f(\tilde{q}_\mu|0, \tilde{\theta}_0^{obs}) d\tilde{q}_\mu, \quad (6.5)$$

$$CL_s \equiv \frac{CL_{sb}}{CL_b}. \quad (6.6)$$

The signal hypothesis is considered excluded at the 95% confidence level when CL_s is $\leq 5\%$.

6.2 Determination of the Upper Limits and Exclusion Regions

The diphoton data sample and the corresponding background predictions are divided into five bins in E_T^{miss}: 50-60, 60-70, 70-80, 80-100, and above 100 GeV. Each bin is treated as its own channel, and the five channels are combined into one test statistic. The sensitivity is dominated by the highest-E_T^{miss} bin.

Sources of systematic uncertainties (nuisance parameters) that affect the expected signal yield are shown in Table 6.1. The uncertainty of the measured integrated luminosity is 4.5%. The uncertainty of the scale factor of the photon identification efficiency between data and Monte Carlo simulation is 4%, as given in Eq. (4.15). The difference between jet energy corrections applied to data and Monte Carlo simulation has 2% uncertainty. The uncertainty in determining the renormalization scale of the running coupling constant, the parton distribution functions uncertainties on the cross section and acceptance from theoretical calculations are also shown. In Appendix B, PDF uncertainties on cross section and acceptance for different signal scans are given. In addition to the systematic uncertainties listed in Table 6.1, the systematic uncertainties of the QCD and EWK background estimations, as described in Eq. (4.13) and Section 5.4, are considered. The nuisance parameters are assumed to be log-normal distributed.

The CL_s method is applied to obtain the 95% upper limit on the cross section for each point of our signal scans. The 95% upper limit on the cross section is then compared to the expected signal cross section. If the observed cross section upper limit is smaller than the expected signal cross section,

Table 6.1: Summary of systematic uncertainties.

Systematics	Uncertainty [%]
Integrated luminosity	4.5
Photon Data/MC scale factor	4
Jet energy scale	2
Renormalization scale	4 - 28
PDF uncertainty on cross section	4 - 66
PDF uncertainty on acceptance	0.1 - 9

the corresponding point of the signal scan is excluded. Table 6.2 shows an example of one signal point that is excluded, and Table 6.3 shows another example of one signal point that is not excluded. In each Table, the numbers of the observed events, total background estimate, and expected signal yield, together with the 95% confidence level expected and observed limits on the cross section for each E_T^{miss} bin are given. The 95% confidence level combined expected and observed limits on the cross section using five E_T^{miss} bins are shown in the bottom of the tables. The signal cross section corresponds to the given signal point.

6.3 Results

The acceptance times efficiency, next-to-leading-order (NLO) cross section, 95% confidence level (CL) observed upper limit on the cross section, and the 95% CL exclusion contours are shown in Figures 6.1 through 6.6 for different signal scans. Since the GGM signal typically has several jets in the event, there is not much difference between the no-jet requirement and the

Table 6.2: An example of a signal point excluded by this analysis (m_{squark} = 880 GeV, m_{gluino} = 880 GeV, m_{bino} = 375 GeV).

E_T^{miss} bins (GeV)	50-60	60-70	70-80	80-100	>100
Observed Events	199	63	26	26	11
Total Background	$190.3 \pm 17.7 \pm 12.7$	$70.4 \pm 10.7 \pm 13.6$	$17.6 \pm 5.1 \pm 11.5$	$11.6 \pm 4.0 \pm 1.0$	$13.0 \pm 4.2 \pm 1.7$
Signal Yield	3.15 ± 0.48	3.15 ± 0.48	2.20 ± 0.40	7.62 ± 0.75	217.2 ± 4.0
95% CL Expected Limit	14.5 pb	8.90 pb	10.6 pb	2.18 pb	0.053 pb
95% CL Observed Limit	17.2 pb	7.47 pb	12.7 pb	3.62 pb	0.047 pb
95% CL Combined Expected Limit on Cross Section			0.046 pb		
95% CL Combined Observed Limit on Cross Section			0.034 pb		
Signal Cross Section			0.160 pb		

Table 6.3: An example of a signal point that is not excluded by this analysis (m_{squark} = 1440 GeV, m_{gluino} = 1520 GeV, m_{bino} = 375 GeV).

E_T^{miss} bins (GeV)	50-60	60-70	70-80	80-100	>100
Observed Events	199	63	26	26	11
Total Background	$190.3 \pm 17.7 \pm 12.7$	$70.4 \pm 10.7 \pm 13.6$	$17.6 \pm 5.1 \pm 11.5$	$11.6 \pm 4.0 \pm 1.0$	$13.0 \pm 4.2 \pm 1.7$
Signal Yield	0.008 ± 0.002	0.012 ± 0.002	0.012 ± 0.002	0.02 ± 0.003	1.51 ± 0.03
95% CL Expected Limit	36.1 pb	36.4 pb	36.1 pb	36.6 pb	6.99 pb
95% CL Observed Limit	36.6 pb	36.4 pb	36.1 pb	36.6 pb	6.47 pb
95% CL Combined Expected Limit on Cross Section			6.89 pb		
95% CL Combined Observed Limit on Cross Section			5.20 pb		
Signal Cross Section			0.001 pb		

requirement of at least one jet in terms of observed and expected upper limits. The exclusion limits are shown only for the case of events with at least one jet. Table 6.4 summarizes the exclusion regions in different planes of the signal phase space.

The results of this analysis are comparable to or better than other SUSY searches. The ATLAS experiment has performed a similar search based on an integrated luminosity of 4.8 fb^{-1} in pp collisions at $\sqrt{s} = 7$ TeV [64]. They exclude the gluinos (squarks) masses below 1.07 TeV (0.87 TeV) in the GGM model. Several other SUSY searches in different final state modes are also performed by the CMS experiment [65]. The results are interpreted in the context of the simplified model spectra, which are summarized in Figure 6.7.

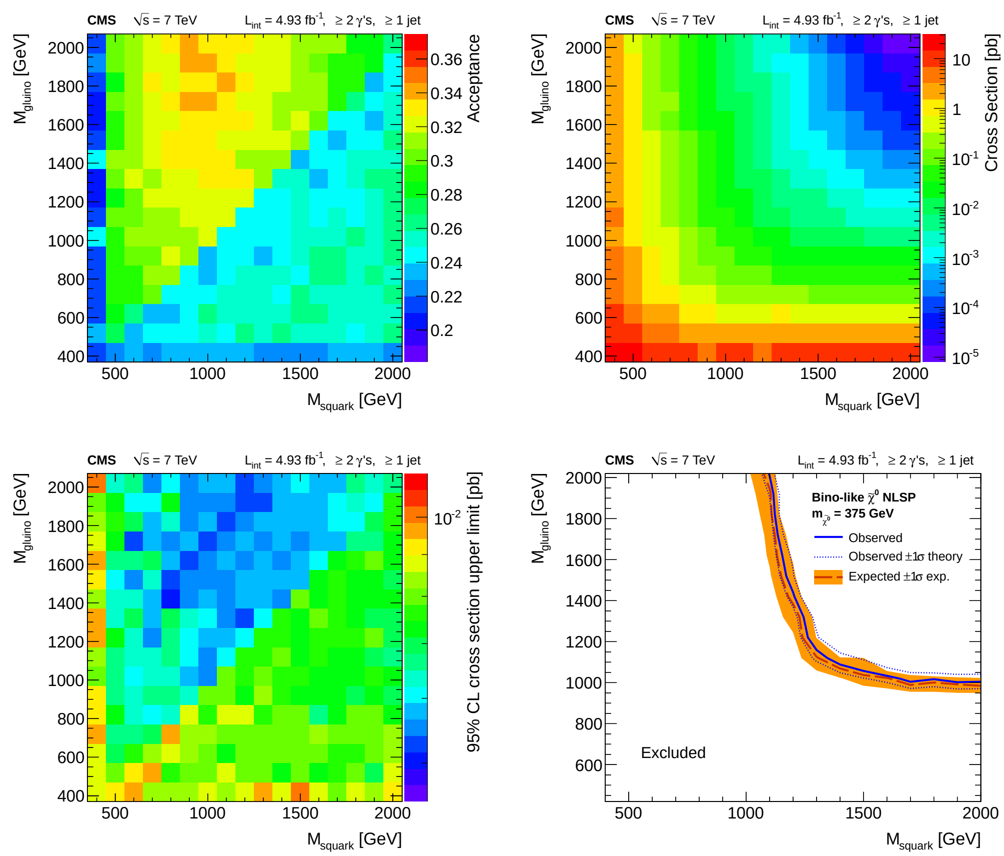

Figure 6.1: Acceptance (top left), theoretical production cross section (top right), observed 95% CL cross section upper limit (bottom left), and exclusion contours including the observed and expected 95% CL limits on the gluino and squark masses (bottom right) as a function of the gluino and squark masses in the GGM model with a bino-like neutralino.

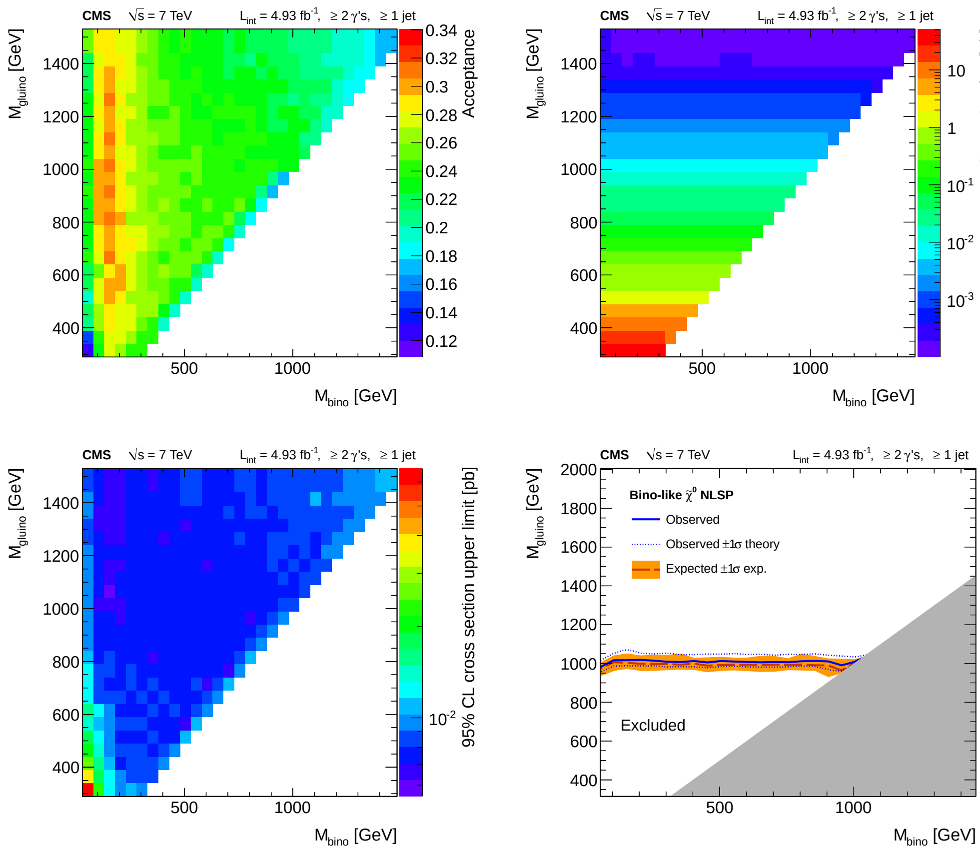

Figure 6.2: Acceptance (top left), theoretical production cross section (top right), observed 95% CL cross section upper limit (bottom left), and exclusion contours including the observed and expected 95% CL limits on the gluino mass (bottom right) as a function of the bino-like neutralino mass in the GGM model (the gray area indicates the region for which the gluino mass is less than the bino mass, which is not considered here).

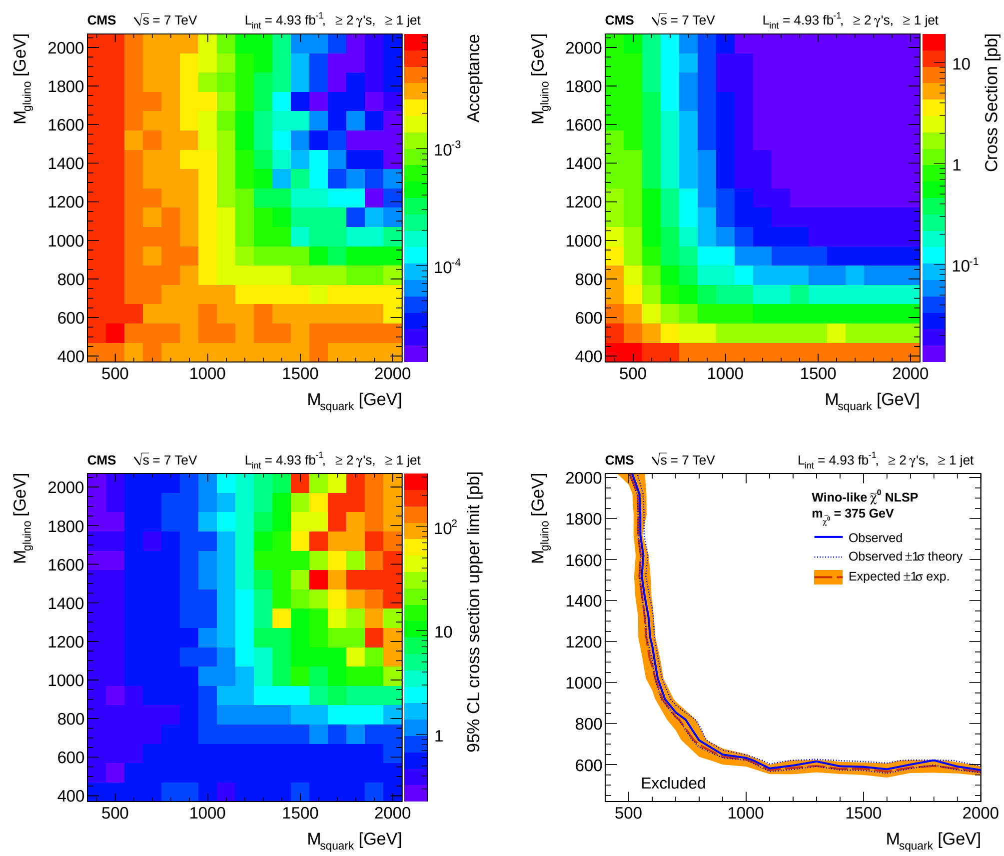

Figure 6.3: Acceptance (top left), theoretical production cross section (top right), observed 95% CL cross section upper limit (bottom left), and exclusion contours including the observed and expected 95% CL limits on the gluino and squark masses (bottom right) as a function of the gluino and squark masses in the GGM model with a wino-like neutralino.

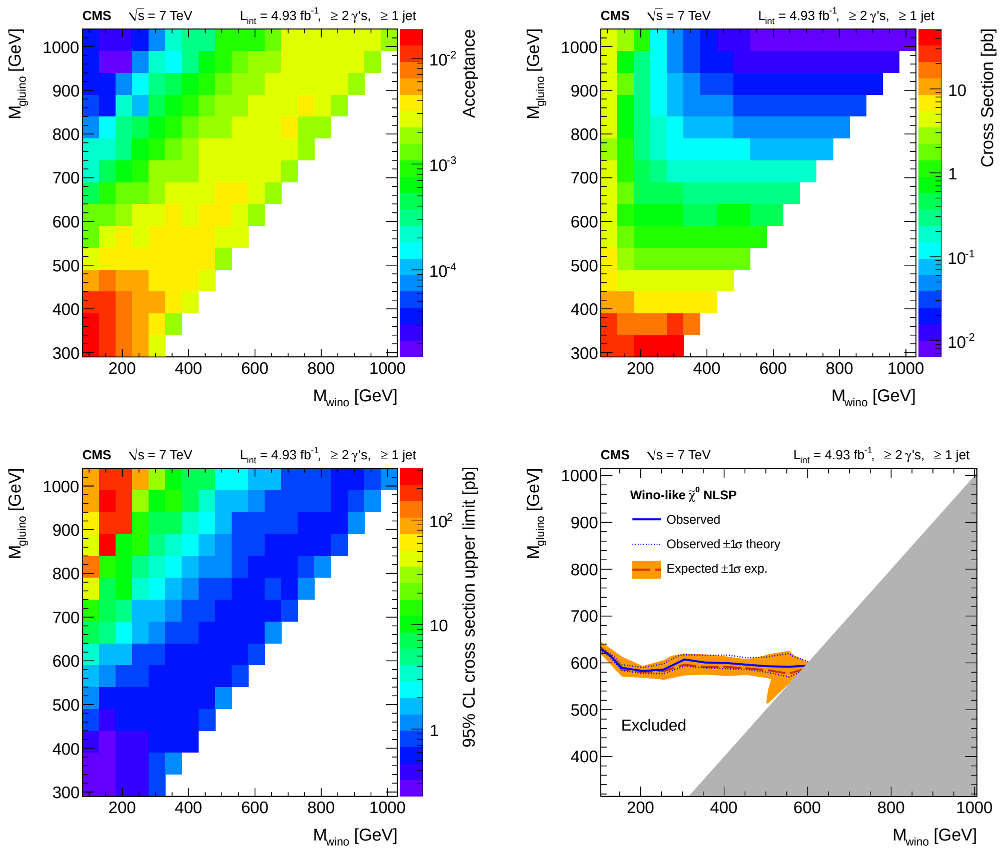

Figure 6.4: Acceptance (top left), theoretical production cross section (top right), observed 95% CL cross section upper limit (bottom left), and exclusion contours including the observed and expected 95% CL limits on the gluino mass (bottom right) as a function of the wino-like neutralino mass in the GGM model (the gray area indicates the region for which the gluino mass is less than the wino mass, which is not considered here).

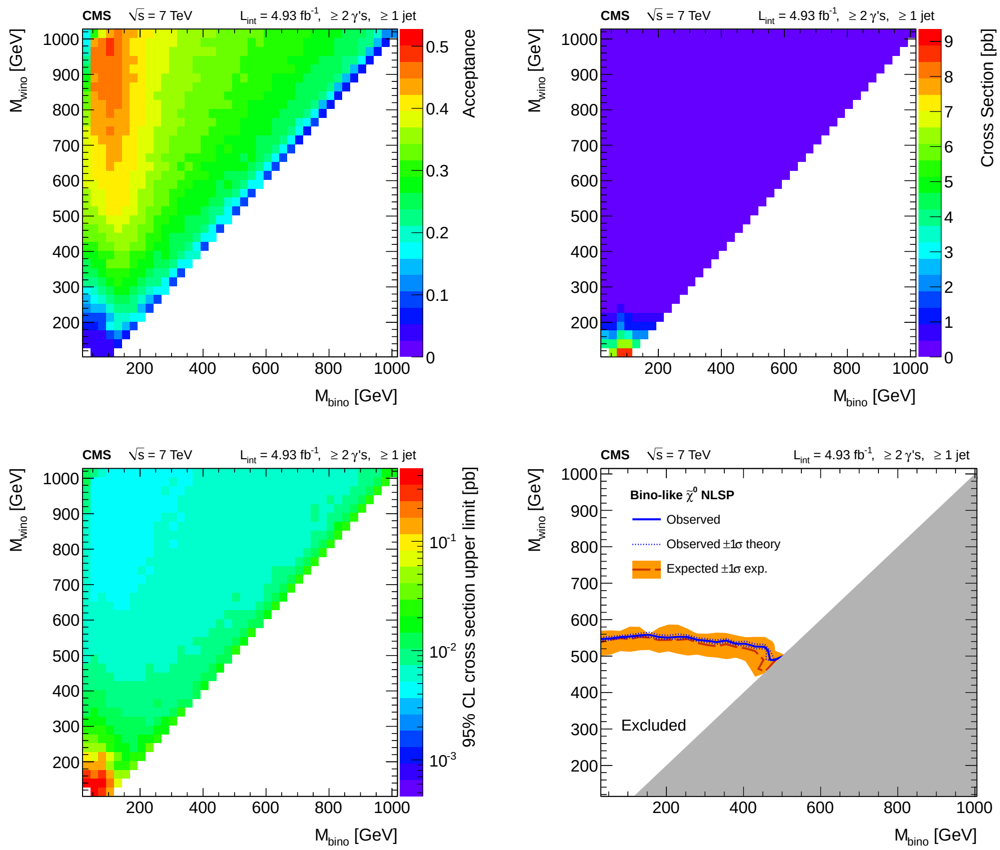

Figure 6.5: Acceptance (top left), theoretical production cross section (top right), observed 95% CL cross section upper limit (bottom left), and exclusion contours including the observed and expected 95% CL limits on the wino-like neutralino mass (bottom right) as a function of the bino-like neutralino mass in the GGM model (the gray area indicates the region for which the wino-like neutralino mass is less than the bino mass, which is not considered here).

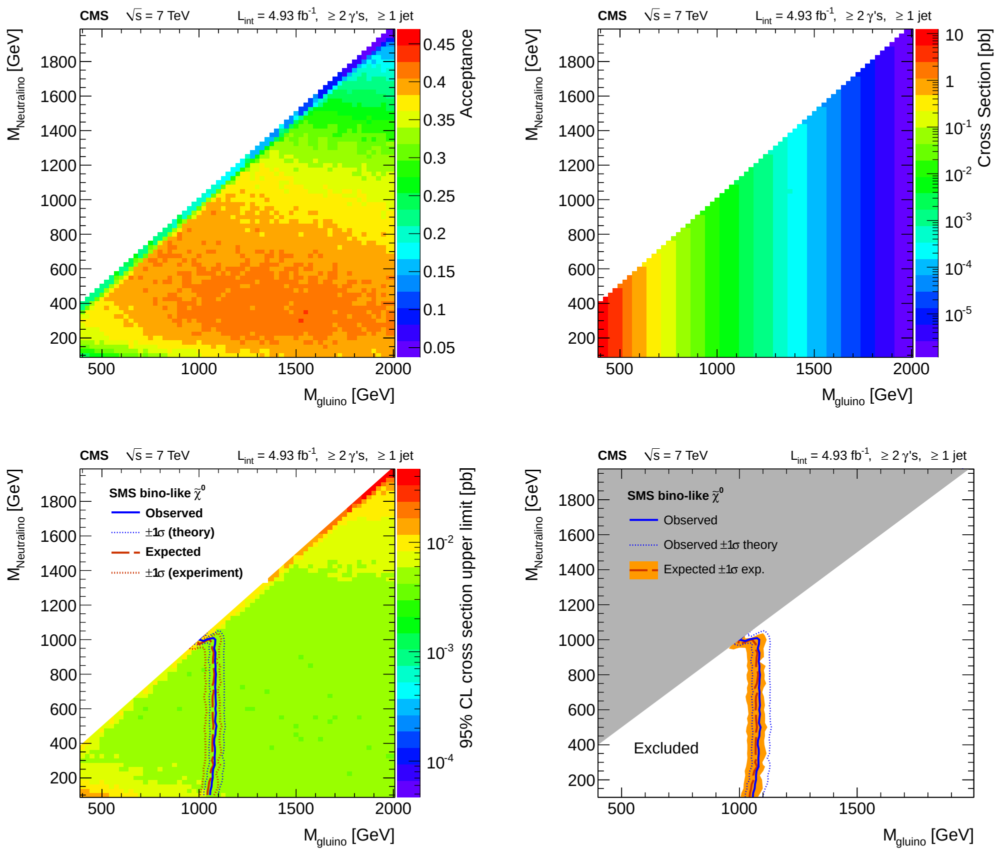

Figure 6.6: Acceptance (top left), theoretical production cross section (top right), observed 95% CL cross section upper limit (bottom left), and exclusion contours including the observed and expected 95% CL limits on the gluino mass (bottom right) as a function of the bino-like neutralino mass in the SMS (the gray area indicates the region for which the gluino mass is less than the bino mass, which is not considered here).

Table 6.4: Summary of the approximate exclusion regions.

Scan	Exclusion
gluino-squark, bino-like neutralino	gluino, squark $\lesssim$ 1 TeV
gluino-bino	gluino $\lesssim$ 1 TeV
gluino-squark, wino-like neutralino	gluino, squark $\lesssim$ 600 GeV
gluino-wino	gluino $\lesssim$ 600 GeV
wino-bino	wino $\lesssim$ 550 GeV
lesssimplified model	gluino $\lesssim$ 1 TeV

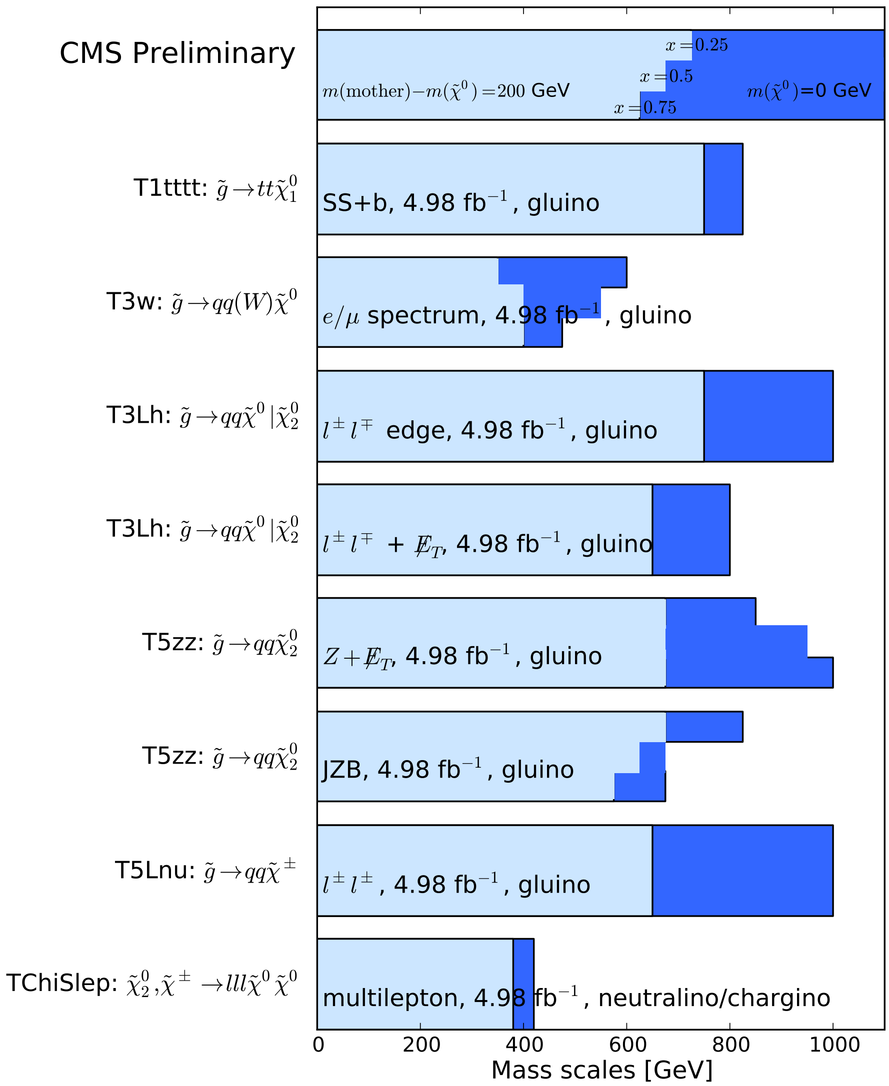

Figure 6.7: Exclusion limits from different analyses interpreted in SMS for LSP $m_{\tilde{\chi}^0}$ = 0 GeV (dark blue) and gluino (squark) mass $m_{\tilde{g}}$ ($m_{\tilde{q}}$) - $m_{\tilde{\chi}^0}$ = 200 GeV (light blue). The mass of the intermediate particle for cascade decays is specified by $x \cdot m_{\tilde{g}} + (1-x) \cdot m_{\tilde{\chi}^0}$. If it is not specified, $x = 0.5$ is chosen.

Chapter 7

Conclusion

We have performed a search for new physics based on a gauge-mediated supersymmetry breaking model using events with two photons and missing transverse energy in the final state. Data corresponding to an integrated luminosity of 4.93 fb^{-1} from pp collisions at $\sqrt{s} = 7$ TeV, collected by the CMS detector at the LHC in 2011, were analyzed. A data-driven method was used to estimate the standard model backgrounds from QCD and electroweak processes. The observed data agree with the standard model background predictions, and no excess of events at high missing transverse energy is observed. We set upper limits on the observed signal cross section for GGM models ranging from 0.001 to 0.01 pb at the 95% confidence level. We exclude both gluino and squark masses below $\sim$ 1 TeV for a bino-like neutralino and up to $\sim$ 600 GeV for a wino-like neutralino. The results of this analysis were also interpreted in the context of the simplified model, and gluino masses below $\sim$ 1 TeV were excluded.

This analysis pushes the limits on the masses of possible SUSY particles higher than ~ 1 TeV. The existence of SUSY particles with masses too far above the weak scale cause a naturalness problem that is also the concern of other current SUSY searches. However, there is still plenty of parameter space in which to search for SUSY, since there are many free parameters in the general theory of SUSY. Even if, in the end, experimental searches rule out SUSY as the theory beyond the SM, this would still constitute an important milestone in particle physics.

However, we are still optimistic about the possibility of discovering SUSY at the LHC. The LHC will run at a higher center-of-mass energy of $13-14$ TeV starting in 2015, and deliver much larger integrated luminosities in the coming years. In addition, upgrades of the CMS detector will provide better measurements of the collision events. Therefore, we are looking forward to the upcoming LHC run and the physics results that will emerge from it.

Bibliography

[1] ATLAS Collaboration, "Search for Diphoton Events with Large Missing Transverse Momentum in 1 fb^{-1} of 7 TeV Proton-Proton Collision Data with the ATLAS Detector", *Phys. Lett.* **B710** (2012) 519–537, `arXiv:1111.4116`. `doi:10.1016/j.physletb.2012.02.054`.

[2] CMS Collaboration, "Search for Supersymmetry in pp Collisions at $\sqrt{s} = 7$ TeV in Events with Two Photons and Missing Transverse Energy", *Phys. Rev. Lett.* **106** (2011) 211802, `arXiv:1103.0953`. `doi:10.1103/PhysRevLett.106.211802`.

[3] CDF Collaboration, "Search for Supersymmetry with Gauge-Mediated Breaking in Diphoton Events with Missing Transverse Energy at CDF II", *Phys. Rev. Lett.* **104** (2010) 011801, `arXiv:0910.3606`. `doi:10.1103/PhysRevLett.104.011801`.

[4] D0 Collaboration, "Search for diphoton events with large missing transverse energy in 6.3 fb^{-1} of $\mathbf{p\bar{p}}$ collisions at $\sqrt{\mathbf{s}} = \mathbf{1.96}$ TeV", *Phys. Rev. Lett.* **105** (2010) 221802, `arXiv:1008.2133`. `doi:10.1103/PhysRevLett.105.221802`.

[5] D. Griffiths, "Introduction to Elementary Particles". John Wiley & Sons, 1987.

[6] M. E. Peskin and D. V. Schroeder, "An Introduction to Quantum Field Theory". Westview Press, 1995.

[7] D. Gross and F. Wilczek, "Asymptotically Free Gauge Theories. I", *Phys. Rev.* **D8** (1973) 3633–3652. `doi:10.1103/PhysRevD.8.3633`.

[8] S. Glashow, "Partial Symmetries of Weak Interactions", *Nucl. Phys.* **22** (1961) 579–588. `doi:10.1016/0029-5582(61)90469-2`.

[9] S. Weinberg, "A Model of Leptons", *Phys. Rev. Lett.* **19** (1967) 1264–1266. `doi:10.1103/PhysRevLett.19.1264`.

[10] A. Salam, "Weak and Electromagnetic Interactions", *Conf. Proc.* **C680519** (1968) 367–377.

[11] P. W. Higgs, "Broken Symmetries and the Masses of Gauge Bosons", *Phys. Rev. Lett.* **13** (1964) 508–509. `doi:10.1103/PhysRevLett.13.508`.

[12] ATLAS Collaboration, "Observation of a new particle in the search for the Standard Model Higgs boson with the ATLAS detector at the LHC", *Phys. Lett.* **B716** (2012) 1–29, `arXiv:1207.7214`. `doi:10.1016/j.physletb.2012.08.020`.

[13] CMS Collaboration, "Observation of a new boson at a mass of 125 GeV with the CMS experiment at the LHC", *Phys. Lett.* **B716** (2012) 30–61, `arXiv:1207.7235`. `doi:10.1016/j.physletb.2012.08.021`.

[14] S. P. Martin, K. R. Dienes, C. Kolda et al., "Perspectives on Supersymmetry II". World Scientific Publishing Company, 2010.

[15] D. Clowe, M. Bradac, A. H. Gonzalez et al., “A direct empirical proof of the existence of dark matter”, *Astrophys. J.* **648** (2006) L109–L113, `arXiv:astro-ph/0608407`. `doi:10.1086/508162`.

[16] K. G. Begeman, A. H. Broeils, and R. H. Sanders, “Extended rotation curves of spiral galaxies - Dark haloes and modified dynamics”, *Monthly Notices of the Royal Astronomical Society* **249** (1991) 523–537.

[17] V. C. Rubin, W. K. J. Ford, and N. Thonnard, “Rotational properties of 21 SC galaxies with a large range of luminosities and radii, from NGC 4605 /R = 4kpc/ to UGC 2885 /R = 122 kpc”, *Astrophysical Journal, Part 1* **238** (1980) 471–487. `doi:10.1086/158003`.

[18] WMAP Collaboration Collaboration, “Five-Year Wilkinson Microwave Anisotropy Probe (WMAP) Observations: Data Processing, Sky Maps, and Basic Results”, *Astrophys. J. Suppl.* **180** (2009) 225–245, `arXiv:0803.0732`. `doi:10.1088/0067-0049/180/2/225`.

[19] H. Georgi and S. L. Glashow, “Unity of All Elementary-Particle Forces”, *Phys. Rev. Lett.* **32** (1974) 438–441. `doi:10.1103/PhysRevLett.32.438`.

[20] A. Buras, J. Ellis, M. Gaillard et al., “Aspects of the grand unification of strong, weak and electromagnetic interactions”, *Nuclear Physics B* **135** (1978), no. 1, 66–92. `doi:10.1016/0550-3213(78)90214-6`.

[21] P. C. West, “Introduction to Supersymmetry and Supergravity”. World Scientific, 1990.

[22] I. Aitchison, "Supersymmetry in Particle Physics: An Elementary Introduction". Cambridge Univ. Press, Cambridge, 2007.

[23] P. Fayet, "Mixing Between Gravitational and Weak Interactions Through the Massive Gravitino", *Phys. Lett.* **B70** (1977) 461. `doi:10.1016/0370-2693(77)90414-2`.

[24] P. Meade, N. Seiberg, and D. Shih, "General Gauge Mediation", *Prog. Theor. Phys. Suppl.* **177** (2009) 143–158, `arXiv:0801.3278`. `doi:10.1143/PTPS.177.143`.

[25] M. Buican, P. Meade, N. Seiberg et al., "Exploring General Gauge Mediation", *JHEP* **03** (2009) 016, `arXiv:0812.3668`. `doi:10.1088/1126-6708/2009/03/016`.

[26] S. Abel, M. J. Dolan, J. Jaeckel et al., "Phenomenology of Pure General Gauge Mediation", *JHEP* **12** (2009) 001, `arXiv:0910.2674`. `doi:10.1088/1126-6708/2009/12/001`.

[27] Y. Kats, P. Meade, M. Reece et al., "The Status of GMSB After 1/fb at the LHC", *JHEP* **1202** (2012) 115, `arXiv:1110.6444`. `doi:10.1007/JHEP02(2012)115`.

[28] J. T. Ruderman and D. Shih, "General Neutralino NLSPs at the Early LHC", *JHEP* **1208** (2012) 159, `arXiv:1103.6083`. `doi:10.1007/JHEP08(2012)159`.

[29] J. Alwall, P. Schuster, and N. Toro, "Simplified Models for a First Characterization of New Physics at the LHC", *Phys. Rev.* **D79** (2009) 075020, `arXiv:0810.3921`. `doi:10.1103/PhysRevD.79.075020`.

[30] D. S. Alves, E. Izaguirre, and J. G. Wacker, "Where the Sidewalk Ends: Jets and Missing Energy Search Strategies for the 7 TeV LHC", *JHEP* **1110** (2011) 012, arXiv:1102.5338. doi:10.1007/JHEP10(2011)012.

[31] LHC New Physics Working Group Collaboration, "Simplified Models for LHC New Physics Searches", arXiv:1105.2838.

[32] A. Breskin and R. Voss, "The CERN Large Hadron Collider: Accelerator and Experiments". CERN, Geneva, 2009.

[33] CMS Collaboration, "CMS Physics Technical Design Report Volume I: Detector Performance and Software". Technical Design Report CMS. CERN, Geneva, 2006.

[34] CMS Collaboration, "ECAL Detector Performance, 2011 Data", CMS Performance Note CMS DP-12-007, CERN, (2012).

[35] CMS Collaboration, "MET Performance in 2011 CMS Data", CMS Performance Note CMS DP-12-003, CERN, (2012).

[36] W. Adam, B. Mangano, T. Speer et al., "Track Reconstruction in the CMS tracker", CMS Note CMS-NOTE-2006-041, CERN, Geneva, (Dec, 2006).

[37] CMS Collaboration, "Tracking and Vertexing Results from First Collisions", CMS Physics Analysis Summary CMS-PAS-TRK-10-001, CERN, (2010).

[38] CMS Collaboration, "CMS Tracking Performance Results from early LHC Operation", *Eur. Phys. J.* **C70** (2010) 1165–1192, arXiv:1007.1988.

[39] CMS Collaboration, "Tracking and Primary Vertex Results in First 7 TeV Collisions", CMS Physics Analysis Summary CMS-PAS-TRK-10-005, CERN, (2010).

[40] T. Speer, K. Prokofiev, R. Frühwirth et al., "Vertex Fitting in the CMS Tracker", CMS Note CMS-NOTE-2006-032, CERN, Geneva, (Feb, 2006).

[41] R. Frühwirth, W. Waltenberger, and P. Vanlaer, "Adaptive Vertex Fitting", CMS Note CMS-NOTE-2007-008, CERN, Geneva, (Mar, 2007).

[42] S. Baffioni, C. Charlot, F. Ferri et al., "Electron reconstruction in CMS", *Eur. Phys. J.* **C49** (2007) 1099–1116. `doi:10.1140/epjc/s10052-006-0175-5`.

[43] W. Adam, R. Frühwirth, A. Strandlie et al., "Reconstruction of electrons with the Gaussian-sum filter in the CMS tracker at the LHC", *Journal of Physics G: Nuclear and Particle Physics* **31** (2005), no. 9, N9.

[44] W. Adam, S. Baffioni, F. Beaudette et al., "Electron Reconstruction in CMS", CMS Analysis Note CMS AN -2009/164, CERN, Geneva, (2009).

[45] M. Anderson, A. Askew, A. Barfuss et al., "Review of clustering algorithms and energy corrections in ECAL", CMS Internal Note CMS IN -2010/008, CERN, (2010).

[46] G. Abbiendi, N. Adam, J. Alcaraz et al., "Muon Reconstruction in the CMS Detector", CMS Analysis Note CMS-AN-2008/097, CERN,

Geneva, (2009).

[47] CMS Collaboration, "Performance of muon identification in pp collisions at $\sqrt{s} = 7$ TeV", CMS Physics Analysis Summary CMS-PAS-MUO-10-002, CERN, (2010).

[48] CMS Collaboration, "Particle-Flow Event Reconstruction in CMS and Performance for Jets, Taus, and MET", CMS Physics Analysis Summary CMS-PAS-PFT-09-001, CERN, (2009).

[49] CMS Collaboration, "Commissioning of the Particle-flow Event Reconstruction with the first LHC collisions recorded in the CMS detector", CMS Physics Analysis Summary CMS-PAS-PFT-10-001, CERN, (2010).

[50] M. Cacciari, G. P. Salam, and G. Soyez, "The Anti-k(t) jet clustering algorithm", *JHEP* **0804** (2008) 063, arXiv:0802.1189. doi:10.1088/1126-6708/2008/04/063.

[51] CMS Collaboration, "Jet Energy Corrections determination at 7 TeV", CMS Physics Analysis Summary CMS-PAS-JME-10-010, CERN, (2010).

[52] A. Djouadi, J.-L. Kneur, and G. Moultaka, "SuSpect: A Fortran code for the supersymmetric and Higgs particle spectrum in the MSSM", *Comput. Phys. Commun.* **176** (2007) 426–455, arXiv:hep-ph/0211331. doi:10.1016/j.cpc.2006.11.009.

[53] M. Muhlleitner, A. Djouadi, and Y. Mambrini, "SDECAY: A Fortran code for the decays of the supersymmetric particles in the MSSM",

Comput. Phys. Commun. **168** (2005) 46–70, arXiv:hep-ph/0311167. doi:10.1016/j.cpc.2005.01.012.

[54] T. Sjostrand, S. Mrenna, and P. Z. Skands, "PYTHIA 6.4 Physics and Manual", *JHEP* **0605** (2006) 026, arXiv:hep-ph/0603175. doi:10.1088/1126-6708/2006/05/026.

[55] J. Pumplin, D. Stump, J. Huston et al., "New generation of parton distributions with uncertainties from global QCD analysis", *JHEP* **0207** (2002) 012, arXiv:hep-ph/0201195.

[56] M. Whalley, D. Bourilkov, and R. Group, "The Les Houches accord PDFs (LHAPDF) and LHAGLUE", arXiv:hep-ph/0508110.

[57] W. Beenakker, R. Hopker, and M. Spira, "PROSPINO: A Program for the production of supersymmetric particles in next-to-leading-order QCD", arXiv:hep-ph/9611232.

[58] CMS Collaboration, "Search for Gauge Mediated Supersymmetry Breaking Using Two Photons and Missing Transverse Energy", CMS Analysis Note CMS AN -2012/515, CERN, Geneva, (2012).

[59] CMS Collaboration, "Search for Supersymmetry in Events with Photons and Missing Transverse Energy", CMS Physics Analysis Summary CMS-PAS-SUS-12-001, CERN, (2012).

[60] M. Cacciari and G. P. Salam, "Pileup subtraction using jet areas", *Phys. Lett.* **B659** (2008) 119–126, arXiv:0707.1378. doi:10.1016/j.physletb.2007.09.077.

[61] http://root.cern.ch/drupal/content/roofit.

[62] A. L. Read, "Presentation of search results: the CL_s technique", *J. Phys.* **G28** (2002) 2693. doi:10.1088/0954-3899/28/10/313.

[63] ATLAS and CMS Collaboration, "Procedure for the LHC Higgs boson search combination in Summer 2011", CMS Note CMS-NOTE-2011-005, CERN, Geneva, (Aug, 2011).

[64] ATLAS Collaboration, "Search for diphoton events with large missing transverse momentum in 7 TeV proton-proton collision data with the ATLAS detector", *Phys. Lett.* **B718** (2012) 411–430, arXiv:1209.0753. doi:10.1016/j.physletb.2012.10.069.

[65] CMS Collaboration, "Interpretation of Searches for Supersymmetry", CMS Physics Analysis Summary CMS-PAS-SUS-11-016, CERN, (2012).

Appendix A

Event Display

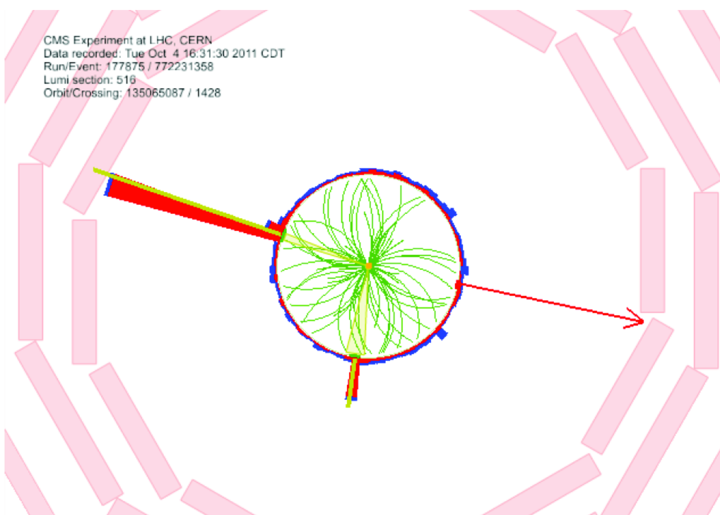

Figure A.1: Event display of one event with two photons (long red strip: 156 GeV photon; short red strip: 33 GeV photon) and high missing transverse energy (red arrow: 164 GeV E_T^{miss}) in the final state.

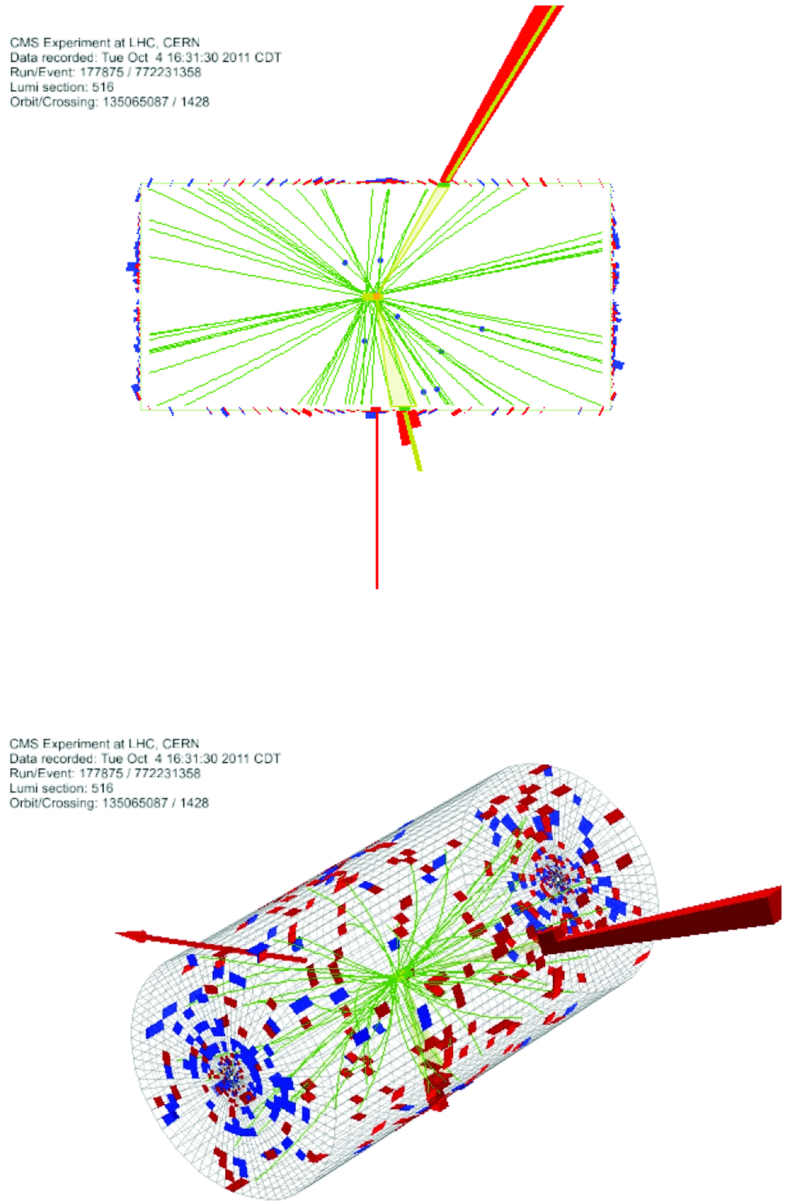

Figure A.2: Event display in ρ-z coordinate (top) and 3D view (bottom).

Appendix B

Systematic Uncertainties of Signal Scans

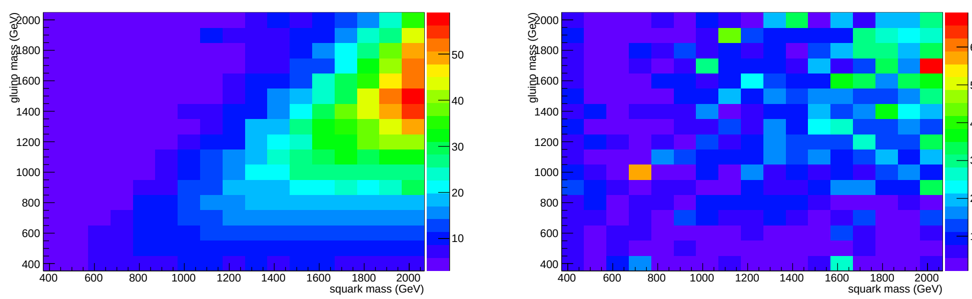

Figure B.1: PDF uncertainties of cross section (left) and acceptance (right) in percent for gluino-squark bino-like neutralino scans.

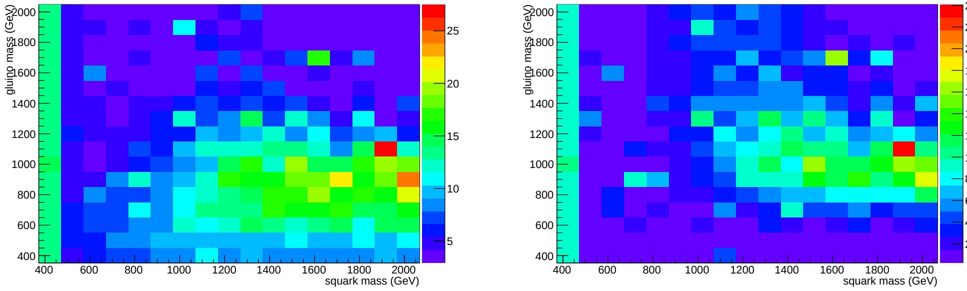

Figure B.2: PDF uncertainties of cross section (left) and acceptance (right) in percent for gluino-squark wino-like neutralino scans.

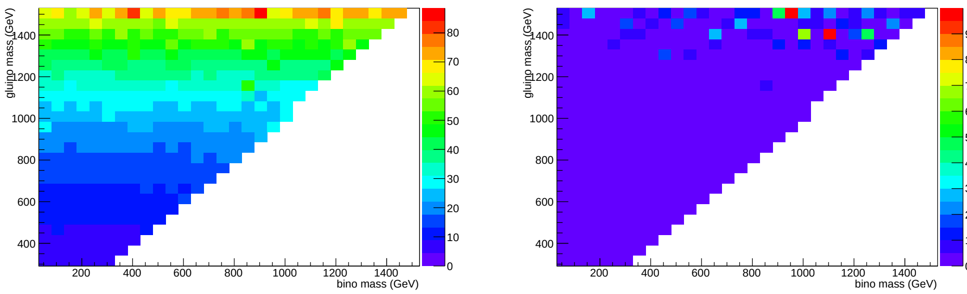

Figure B.3: PDF uncertainties of cross section (left) and acceptance (right) in percent for gluino-bino scans.

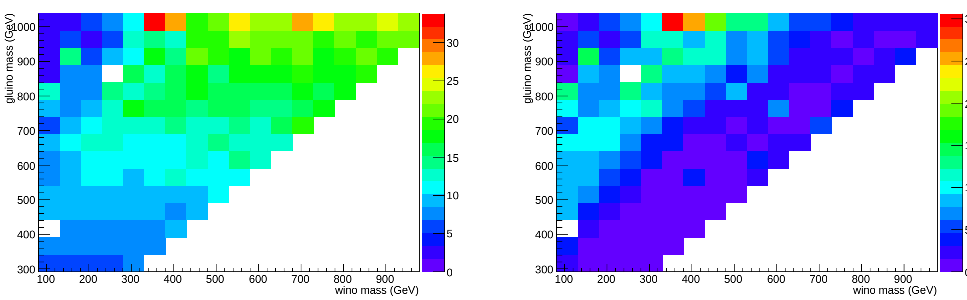

Figure B.4: PDF uncertainties of cross section (left) and acceptance (right) in percent for gluino-wino scans.

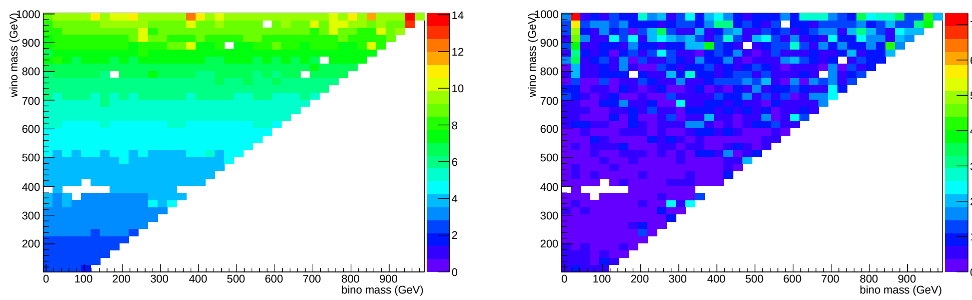

Figure B.5: PDF uncertainties of cross section (left) and acceptance (right) in percent for wino-bino scans.

Appendix C

Test for the QCD Background Estimation

In order to validate the QCD background estimation method, especially for the ee sample, we perform a test using Monte Carlo simulation. The same procedures used in data are applied to the Monte Carlo simulation samples. Since there is no other contributions contained in the Monte Carlo simulation ee sample, sideband and diboson subtractions are not needed. Table C.1 shows the Monte Carlo simulation samples used to obtain $\gamma\gamma$ and ee events. Figure C.1 shows the test for the E_T^{miss} distributions. The test demonstrates that we can use the E_T^{miss} distribution of the ee sample to estimate the E_T^{miss} distribution of the QCD diphoton events by applying di-EMPt reweighting procedure.

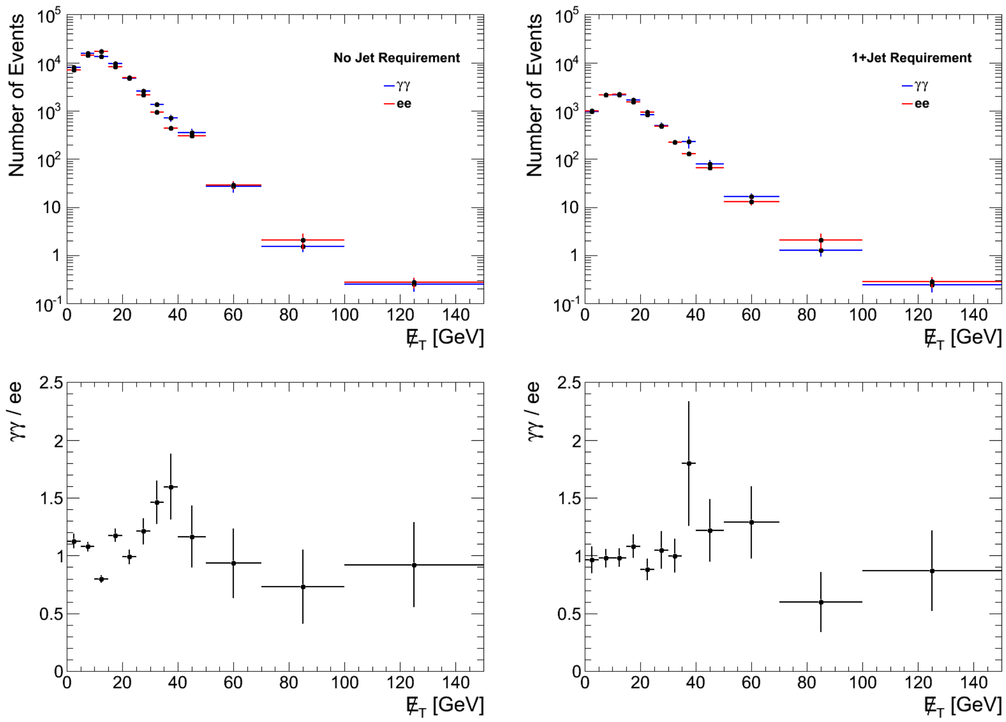

Figure C.1: The E_T^{miss} distributions of the $\gamma\gamma$ and ee Monte Carlo simulation samples for the events with no jets (left) and with at least one jet (right). The bottom plots show the ratio of the $\gamma\gamma$ to ee sample as a function of the E_T^{miss}.

Table C.1: Monte Carlo simulation samples used for the QCD background test.

$\gamma\gamma$ sample	DiPhotonBox-Pt-25To250-7TeV-pythia6
	G-Pt-30to50-TuneZ2-7TeV-pythia6
	G-Pt-50to80-TuneZ2-7TeV-pythia6
	G-Pt-80to120-TuneZ2-7TeV-pythia6
	G-Pt-120to170-TuneZ2-7TeV-pythia6
	G-Pt-170to300-TuneZ2-7TeV-pythia6
	G-Pt-300to470-TuneZ2-7TeV-pythia6
	G-Pt-470to800-TuneZ2-7TeV-pythia6
ee sample	ZjetToEE-Pt-30to50-TuneZ2-7TeV-pythia6
	ZjetToEE-Pt-50to80-TuneZ2-7TeV-pythia6
	ZjetToEE-Pt-80to120-TuneZ2-7TeV-pythia6
	ZjetToEE-Pt-120to170-TuneZ2-7TeV-pythia6
	ZjetToEE-Pt-170to230-TuneZ2-7TeV-pythia6
	ZjetToEE-Pt-230to300-TuneZ2-7TeV-pythia6
	ZjetToEE-Pt-300-TuneZ2-7TeV-pythia6